Intracranial MR Angiography using Pseudo Continuous ASL (PCASL) and Accelerated 3D Radial Acquisition

by

Huimin Wu

A dissertation submitted in partial fulfillment of
the requirements for the degree of

Doctor of Philosophy

(Medical Physics)

at the

UNIVERSITY OF WISCONSIN–MADISON

2012

Date of final oral examination: 11/21/12

The dissertation is approved by the following members of the Final Oral Committee:
Walter F. Block, Professor, Biomedical Engineering, Medical Physics, and Electrical and Computer Engineering
Charles A. Mistretta, Professor, Medical Physics and Radiology
Patrick A. Turski, Professor, Radiology
Oliver Wieben, Assistant Professor, Medical Physics and Radiology
Andrew L. Alexander, Professor, Medical Physics and Psychiatry
Kevin M. Johnson, Assistant Scientist, Medical Physics

To my mother Junhua Zhang, my father Liping Wu, my husband Zhihua Qi, and my dear daughter Blair Qi

Acknowledgments

I would like to express my deepest appreciation to my advisor, Prof. Walter F. Block. Ever since my first day of being a badger, he has been teaching me by example how to burrow through the ground of practical challenges in order to unveil the hidden scientific beauty. His infectious passion and consistent encouragement has also provided much needed guidance through my graduate study. When I re-enrolled the program after a dropout, he graciously offered to be my advisor again and matched me up with Chuck and Pat on another exciting project. His advice, support and friendship have been invaluable on both an academic and a personal level, for which I am extremely grateful.

I am greatly indebted to both Prof. Charles A. Mistretta and Prof. Patrick A. Turski. for their financial support and scientific guidance of my dissertation work. I have been fortunate to work with them, who always encourge new ideas and love to invest time and energy in training younger generations.

I also would like to thank Prof. Oliver Wieben and Prof. Andy Alexander for serving on my committee and offering insights on my work.

I cannot say enough thanks to Dr. Kevin Johnson for his tremendous help and valualbe suggsetions. His uncanny ability to find ways to generate nice-looking MR images, whether by coding, pulse sequence development, or experimental design, has made the clear difference for the projects we have worked on.

I want to thank all the other faculty, staff and students in the MR group who have

given me a lot of help over the years. Special thanks go to Dr. Alexey Samsonov for his instrumental help in my early days of MR research.

Thanks to my husband, Zhihua Qi, who has always been my biggest cheerleader and never complained about being my guinea pig for as many times as needed in testing my MR pulse sequence, and my daughter, Blair, who gives me just enough breaks to complete my dissertation work in time.

Contents

Tables

Figures

Abstract

Intracranial angiography is important for both diagnosis and treatment planning of cerebral vasculature system. Non-contrast-enhanced Magnetic Resonance Angiography (MRA) technique is of great interest due to the non-invasive and non-contrast nature. The aims of this work are using novel imaging techniques to implement high quality arterial spin labeling (ASL) angiography and validating this technique in cerebral vascular diseases.

3-dimensional (3D) ASL angiography was implemented by combining pseudo continuous ASL (PCASL) and accelerated 3D radial acquisition (PCASL-VIPR). Static PCASL-VIPR was validated with healthy and diseased subjects and compared to 3D time-of-flight (TOF) on image quality and pathology visualization.

Dynamic 3D ASL angiography was implemented on the basis of static PCASL-VIPR and optimized in PCASL pulse train modulation for scan time efficiency. Quantitative evaluation is available through time-of-arrival mapping method. Dynamic PCASL-VIPR was validated with arteriovenous malformation (AVM) patients and compared with 3D TOF for image quality and Digital Subtractive Angiography (X-ray DSA) for temporal fidelity.

High resolution 3D angiography was realized by using compressed sensing (CS) for acceleration. CS was implemented using iterative Soft thresholding (IST) framework with data-driven threshold tuning methods. Other potentials of PCASL including vessel selective imaging and hadamard encoding were also explored and validated with in-vivo study.

1 Introduction

1.1 Clinical motivation

Imaging of the cerebral vasculature is important in the diagnosis of many cerebrovascular diseases, including carotid artery stenosis, intracranial aneurysms, and arteriovenous malformations (AVM), as well as in the assessment of patients.

Within the group of cranial vascular lesions, brain arteriovenous malformations (bAVMs) represent an abnormal communication between pial arteries supplying brain tissue and pial veins draining brain tissue. The risk of intracerebral hemorrhage is approximately 4% per year, resulting in a yearly major morbidity and mortality rate of 2.7% [1]. The size, geometry, location, and flow features of AVMs affect their treatment and outcome. A pre-surgical or pre-radiotherapeutic neuroradiological evaluation consequently requires a diversity of anatomical and hemodynamic information.

A cerebral or brain aneurysm is a cerebrovascular disorder in which weakness in the wall of a cerebral artery or vein causes a localized dilation or ballooning of the blood vessel. In the United States approximately 12,000 to 28000 subarachnoid hemorrhages from ruptured intracranial aneurysms are recorded annually, and only one third of these patient survive without significant disability. These data indicate that cerebral aneurysms and subarachnoid bleeding, as their most common complication, represent an important public health care issue.

Intracranial stenosis is a narrowing of an artery inside the brain that can lead to stroke. Stenosis is caused by a buildup of plaque inside the artery wall that reduces blood flow to the brain. The process of plaque buildup is called atherosclerosis. Atherosclerosis that is severe enough to cause symptoms carries a high risk of stroke and can lead to brain damage and death. Evaluation of hemodynamic function and identification of collateral circulation are important in assessment of the risk of recurrent stroke or ischemia from occluded carotid arteries and in presurgical planning.

1.2 An Overview of major angiographic techniques

1.2.1 Digital Subtractive Angiography (DSA)

Traditionally, intracranial angiograms have been acquired by inserting a catheter into the larger downsteam vessel, injecting a contrast medium, and then observing the passage of contrast bolus using x-ray DSA. X-ray DSA provides excellent visualization of the intracranial vasculature with high spatial resolution. It also provides high temporal resolution of inflow dynamics and has the ability to selectively interrogate specific feeding vessels. However, it has a number of drawbacks: it involves intraarterial catheterization, which is not only labor intensive but also results in increased morbidity and mortality for the patient, with a 0.7% stroke risk associated with each procedure [2]; it exposes the patient to ionizing radiation; it gives information about only a single vessel per contrast injection, and it carries a risk of contrast agent reaction. The injection pressure may modify the normal flow patterns or distort the appearance of distal vessels, leading to misrepresentation of the patient's condition. A noninvasive alternative is therefore desirable.

During the past few years, both magnetic resonance angiography (MRA) and Computed Tomography Angiography (CTA) have been reported to be useful and increasingly precise

in the diagnosis of cerebral vascular diseases; MRA, in particular, has shown a remarkable progress due to new coil designs, new pulse sequences, and additional techniques.

1.2.2 Contrast Enhanced (CE) MRA

Since its introduction in 1994 by Prince [3], first-pass contrast enhanced MR angiography with gadolinium-based contrast material has seen widespread acceptance. The use of Gd in CE MRA improves MR image quality by increasing the SNR as well as by reducing flow and motion artifacts. Instead of relying on blood flow to differentiate vessel lumen from background tissues, a paramagnetic contrast agent (e.g., Gd) is injected intravenously to shorten the T1 relaxation time of blood. Blood can then be directly imaged using a T1-weighted sequence less sensitive to flow effects. 3-dimensional (3D) CE MRA exploits fast spoiled gradient echo sequences to take advantage of their high speed, short echo time, and T1 weighting with a single center of k-space for the entire volume of data. In addition, 3D sequences have high spatial resolution with thin slices and intrinsically high signal-to-noise ratio (SNR).

As applied in intracranial vascular diseases, contrast-enhanced MRA has some theoretical advantages: first of all, contrast-enhanced MRA has a higher signal to noise ratio and a shorter acquisition time than other MRA techniques. As the major T1-shortening effect of the gadolinium, the saturation effect is rare, and this confers high sensitivity to slow flow. Arteries in the imaging volume can be demonstrated regardless of their spatial orientation. Turbulent flow-related artifacts are minimized because of the parameters of the sequence, especially the short echo time, which prevents spin dephasing. Motion artifacts are less common, because of the short acquisition time.

The disadvantage of this technique is its imaging window, which is restricted to the first pass of the contrast bolus. Contrast-enhanced MRA requires a good coordination between the

contrast injection, patient cooperation, and the starting time of the acquisition. Intracranial applications of contrast-enhanced MRA have been mainly limited because of the insufficient spatial resolution due to short time window between arterial and venous enhancement in the cerebral circulation. However, contrast-enhanced MRA has benefited from a lot of new techniques such as 3D time-resolved imaging of contrast kinetics (TRICKS) [4], partial Fourier imaging [5], and parallel imaging [6, 7, 8]. Novel reconstruction methods like HYPR [9, 10] push the spatial and temporal resolution even further. However, the inherent trade-off between the temporal resolution, spatial resolution and SNR limits their clinical applications. Furthermore, the length of the contrast bolus, after circulation through lung and heart increases the difficulty in separating fast and slow flow vascular structures.

A major drawback of contrast enhanced MRA is the injection of Gd-based contrast agents. The recent association between high dose of gadolinium-based contrast material and nephrogenic systemic fibrosis [11] has made it imperative that patients with moderate to severe renal insufficiency and vascular disease have noncontrast alternatives for angiography.

1.2.3 Non-Contrast-Enhanced (NCE) MRA

Development of modern NCE-MRA techniques has been motivated by several factors [12]. First of all, not only the contrast material is expensive, the time, personnel, and equipment for set up and administration of the contrast injection also added cost. Secondly, concerns about a possible link between gadolinium-based contrast agents and nephrogenic systemic fibrosis (NSF) have brought into question the use of these agents for MRA. It is recommended that special considerations be taken regarding the use of gadolinium based contrast agents, especially for renal-compromised patients.

While noncontrast magnetic resonance angiographic methods have been available since the earliest days of MR imaging, prolonged acquisition times and image artifacts have generally

limited their use in favor of gadolinium-enhanced MRA techniques. However, the combination of recent technical advances (in hardware, software, and sequence design) has really made several NCE-MRA techniques feasible for clinical application

Multichannel receiver coil arrays generate higher signal-to-noise ratio (SNR), which can be exchanged for higher resolution. High bandwidth data acquisition hardware combined with faster and stronger gradients facilitate shorter TEs and TRs, enabling faster scan times, higher SNR, and/or higher-resolution images. The application of parallel imaging techniques in NCE-MRA has reduced shot durations and/or the total number of shots, thereby greatly reducing scan times. The higher field strength of the increasingly prevalent 3.0 Tesla scanners not only improves SNR, but also lengthens T1, resulting in reduced stationary tissue signal in inflow-based NCE-MRA and longer blood transit times for spin labeling NCE-MRA.

The major NCE-MRA methods include: phase-contrast (PC- MRA) [13], Time-Of-Flight(TOF) [14], and arterial spin labeling (ASL) techniques [15, 16].

Time-Of-Flight (TOF)

The most commonly used nonenhanced MR angiographic technique has been TOF imaging, developed in the late 1980s. TOF angiography relies on the differences in exposure to radiofrequency excitation between in-plane or in-slab stationary protons and the blood protons flowing into the section or slab. Stationary protons in the imaging section become relatively saturated with repeated excitation pulses and produce low signal intensity. Inflowing blood protons in arteries and veins have not experienced the excitation pulses, are not saturated, and therefore generate high signal intensity.

In TOF, any inflowing blood, whether from venous or arterial sources, arrives with fresh longitudinal magnetization and appears bright. Hence, the technique is prone to venous contamination. For selective imaging of arteries, saturation bands are applied on the venous side of imaging sections to null signal from the venous flow.

The inflow effect is dependent on the vessel orientation relative to the imaging section. The optimal refreshment occurs for arteries running perpendicular to the thinnest dimension of the section volume. For vessels that lie generally in parallel with the imaging section their effective refreshment rate is very low [17].

The thick slab of 3D acquisitions poses a challenge for 3D TOF. The blood velocity needs to be very high to refresh the thick slab. To address this issue the slab can be split into multiple,thinner slabs called multiple overlapping thin-slab acquisition (MOTSA) [18]. This hybrid 2D/3D method is designed to greatly reduce the effective selection thickness and increase the inflow effect. To further reduce blood saturation, the slab can be excited using an RF excitation pulse with ramped slice selection profile like the tilted optimized nonsaturating excitation (TONE) [19] pulse. To further suppress stationary tissue signal, a nonselective off-resonance magnetization transfer (MT) RF pulse can be applied to reduce the signal of brain parenchyma. Brain parenchyma is more susceptible to MT saturation than blood due to its greater relative macromolecular content.

Today, the most common clinical application of 3D TOF angiography is the examination of intracranial vessels. 3D TOF has been routinely used in many clinical institutions as alternative of X-ray DSA. However, it may not provide sufficient image quality in some cases. E.g., stenotic lesions are sites where proton spin dephasing, and consequently flow signal intensity loss, commonly occur. This is due to complex, slow or in-phase flow, all flow characteristics commonly seen in stenotic intracranial vessels. Another limitation of TOF technique is the comparatively long imaging times, frequently leading to patient motion artifacts and degradation of image quality.

Phase Contrast (PC)-MRA

Phase-contrast (PC) MRA also utilizes the fact that blood is flowing through the vessels. In the same way that magnetic field gradients can be used to encode the spatial position

of spins, they can be used to encode the motion, or flow, of spins. Spins in the transverse plane flowing in the vector direction of a gradient field accumulate phase proportional to their speed. In this way, the flow velocity (direction and speed) is encoded in the phase of the spins. Bipolar gradients consisting of two equal but opposite amplitude gradient lobes are commonly used for flow encoding. The bipolar gradients generate net zero phase for stationary spins but a nonzero phase for flowing spins related to the amplitude and duration of the biopolar gradient.

PC-MRA has the advantage of depicting multidirectional flow, including recirculating flow patterns and in-plane flow. Quantitative measurements of flow velocity can be calculated from the phase data using the explicit relationship between velocity and bipolar gradient amplitude and duration.

Due primarily to its long scan times, PC-MRA is not commonly used for routine MRA. Its most common angiographic use is as a low-resolution scout sequence for identifying the location of the carotid arteries. Recently, 3D PC-MRA has become feasible for intracranial applications benefited from the accelerated 3D radial acquisition technique [20].

The other non-contrast MRA technique Arterial Spin Labeling will be discussed in details in the following section.

1.3 Arterial Spin Labeling (ASL)

In addition to time-of-flight and phase-contrast, another way to generate contrast is to use arterial spin labeling (ASL) techniques. ASL employs radio frequency and magnetic field gradient pulses to saturate or invert naturally existing water spins in the feeding arteries and use the magnetically labeled spins as endogenous contrast. Most ASL techniques obtain the difference of two sets of images: labeled images and control images. For labeled image, the proton spins of the arterial water are labeled prior to reaching the imaged volume. A

"control" image is acquired in which, ideally, the arterial water spins have not been altered. Subtraction of these two images removes the static tissue component, leaving only the labeled blood signal.

Since the original innovation of the basic ASL technique byWilliams et al. in 1992 [21], numerous ASL sequences have been developed. Based on how labeling is achieved, these sequences are commonly categorized as either continuous ASL (CASL), or pulsed ASL (PASL).

1.3.1 ASL schemes

Continuous ASL (CASL)

In CASL, the inflowing arterial water spins are "continuously" labeled via inversion through a process called adiabatic fast passage (AFP). Compared to PASL, the SNR of CASL is 30% to 50% higher.

One of the major drawbacks of CASL is the requirement for a long labeling pulse to bring about the adiabatic inversion. This requirement complicates CASL on both theoretical and practical standpoints. Theoretically, long off-resonance RF pulses cause signal loss due to magnetization transfer (MT) effects. The MT effects constrained the initial application of CASL to a single slice where in order to balance these effects, two labeled images were acquired, one above and one below the imaged slice. To circumvent this constraint, Alsop and Detre [22] applied an amplitude-modulated (AM) RF pulse with the same duration as the labeling pulse during the acquisition of the control image. The introduction of the AM pulses moved CASL from single slice to whole-brain imaging thus opening new venues for its applications.

Additionally, the requirement for long continuous RF waveforms and continuous gradient waveforms faces practical challenges. RF hardware on standard scanners often prevents the

performance of continuous labeling. RF amplifiers optimized for pulsed operation typically cannot support CASL because of constraints on the RF duty cycle, especially for body coil transmit. Continuous RF waveforms and continuous gradient waveforms also produce high-power disposition. Several techniques have been developed to overcome this problem. One is dual-coil (DC-CASL) which needs additional transmit coil making it difficult for routine application.

Pulsed ASL(PASL)

In contrast to CASL, labeling in PASL is achieved using more easily implemented short pulses (usually 10-15 ms) that invert spins in a specific region commonly referred to as the inversion slab. Depending on how labeling is applied with respect to the imaging volume, PASL techniques are divided into two main groups: symmetrical and asymmetrical.

The original symmetrical PASL, called flow sensitive alternating inversion recovery (FAIR), was developed in mid 1990s [23, 24, 25]. The sequence consisted of two inversion recovery acquisitions: one involved slice-selective inversion, that is, the magnetization was inverted only at a selected slice, whereas the other was a non-slice-selective inversion. A delay was introduced after each inversion pulse and before image acquisition. After the delay, the tissue magnetization of the imaged volume of the slice-selective inversion includes the signal from the inflow of the uninverted blood. Although various versions of FAIR have been developed, the original FAIR sequence is still the most commonly used.

The asymmetrical PASL sequence, called signal targeting with alternating radiofrequency (STAR), was first proposed by Edelman et al. in 1994 [26]. In this sequence, magnetization is inverted in a thick slab proximal to the imaging slice. The additional control image is similarly acquired after inverting magnetization in a slab symmetrically distal to the imaging slice and thus having the same MT effects. Proximal inversion with a control for off-resonance effects (PICORE) [27] and transfer insensitive labeling technique (TILT) [28] sequences are

based on the original EPISTAR technique.

Generally, PASL has been more widely used because it is easier to implement and conceptually more straightforward than CASL. Also, because shorter labeling pulses are needed, PASL sequences are less affected by MT than the standard CASL sequence. However, drawbacks are still present such as low SNR, high sensitivity to transit times, and slice profile artifacts that can limit brain coverage.

Pseudo Continuous ASL(PCASL)

Pseudo-continuous ASL [29, 30, 31] was developed as an intermediate technique that takes advantage of CASL's superior SNR and PASL's high labeling efficiency without the need for long labeling pulses. A schematic revolution from traditional CASL to pseudo continuous ASL was shown in Figure 1.1.

In the original implementation of flow-driven adiabatic inversion (Figure 1.1(A)), constant RF and gradient fields were applied and the flowing spins were inverted because they follow the effective field, a vector combination of the RF and gradient fields in the rotating frame, as it rotates from positive to negative.

Due to the constraints on pulsed RF amplifiers in many commercial imagers, RF pulses cannot be applied in such a continuous manner. It is natural to try to break up a continuous rectangular RF into a train of rectangular RF pulses separated by a gap (Figure 1.1(B)). However, the rectangular RF pulse train will cause a number of aliased labeling planes. A rectangular RF pulse train with rectangular width δ and spacing Δt can be represented as:

$$RF(t) = \frac{1}{\Delta t} comb(\frac{t}{\Delta t}) rect(\frac{t}{\delta}) \tag{1.1}$$

The Fourier transform of $RF(t)$ is given by:

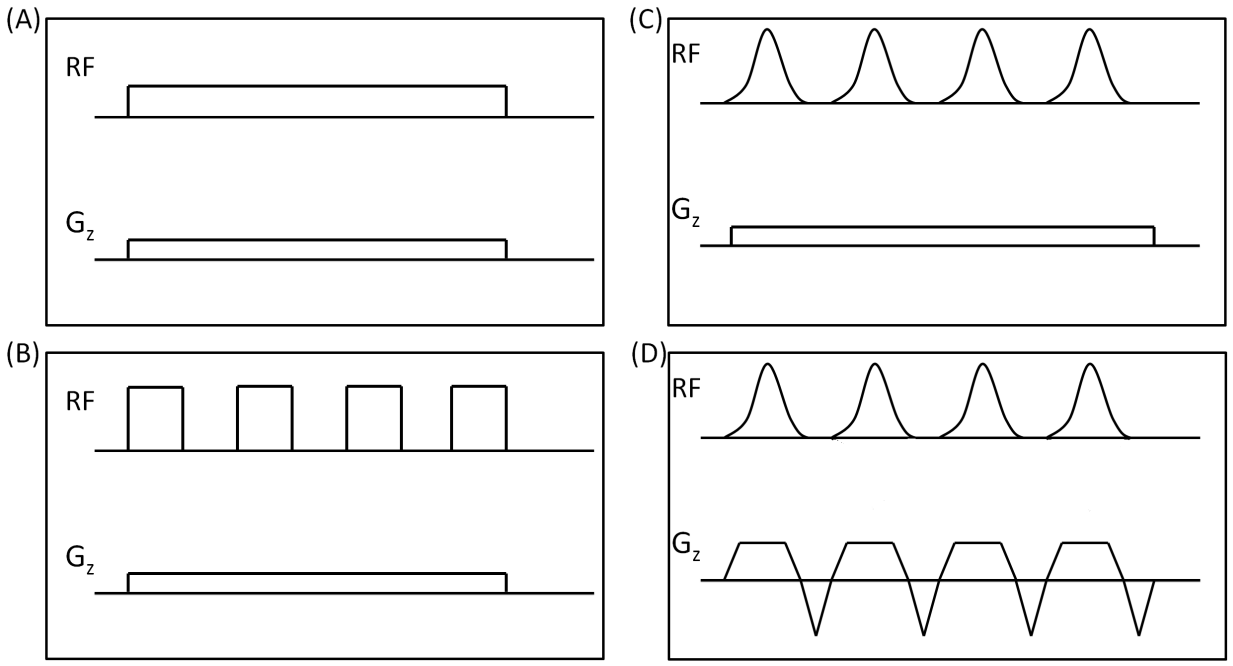

Figure 1.1: Different RF pulse and gradient patterns for continuous ASL: (a) constant RF pulse, constant gradient; (b) rectangular RF pulse train, constant gradient; (c) Hanning RF pulse train, constant gradient; (d) Hanning RF pulse train, variable gradient with strong gradient during RF pulses.

$$F(RF(t)) = comb(f\Delta t)\delta sinc(\pi\delta f) \tag{1.2}$$

One can see from Eq. 1.2, we have aliased labeling planes located at $f = n/\Delta t$ in frequency space, modulated slowly by a broad *sinc* function. With a constant applied gradient g in the z direction, this corresponds to labeling planes at $z = n/(\gamma g \Delta t)$.

To eliminate the undesired aliased planes, a Hanning pulse instead of a rectangular pulse is used (Figure 1.1(C)) so that the Fourier response will drop more rapidly.

$$RF_H(t) = \frac{1}{\Delta t} comb(\frac{t}{\Delta t}) * H(\frac{t}{\delta}) \tag{1.3}$$

where the Hanning function $H(t)$ is defined as

$$H(t) = \begin{cases} 0.5 + 0.5\cos(2\pi t) & |t| < 1/2 \\ 0 & otherwise \end{cases} \tag{1.4}$$

The Fourier transform of the new RF pulse $RF_H(t)$ is given by:

$$F(RF_H(t)) = comb(f\Delta t)\Delta sinc(\pi\delta f)\frac{1}{2(1-\delta^2 f^2)} \tag{1.5}$$

The Fourier transform of the Hanning pulse train drops quadratically faster with frequency than the rectangular pulse train. However, the response of the Hanning pulse is still too broad to remove all of the labeling planes. The first aliased labeling plane is at $f = 1/\Delta t$, where the Hanning response is still well above zero.

To make the RF pulse more spatially selective the gradient amplitude during each Hanning pulse (G_{max}) can be increased relative to the average gradient applied between the center of two RF pulses (G_{ave})(Figure 1.1(D)).

Aliased labeling planes will occur at $z = n/(\gamma G_{ave}\Delta t)$, but the first zero of the Hanning response will be at $z = 1/(\gamma G_{max}\delta)$. Hence aliased labeling planes will be suppressed as long as the condition is met:

$$\frac{G_{max}}{G_{ave}} \gg \frac{\Delta t}{\delta} \tag{1.6}$$

As seen in Figure 1.1(D), PCASL performs the inversion by playing out a long train of RF and gradient pulses which invert the magnetization flowing through a defined labeling plane. Because the RF is pulsed, it is highly compatible with RF hardware optimized for pulsed operation and does not require any additional hardware.

To acquire control image, the relative phase of the RF pulses to spins at the tagging plane

alternates between 0 and 180 degrees while the frequency and amplitude of the RF pulses remains the same as in tag session. In this means, the MT effects are equalized between control and tag acquisition and multi-slice imaging with PCASL is not a problem anymore.

Wu et al. [32] compared optimized PCASL with standard PASL and CASL at 3T and found that PCASL provides a 50% improvement in SNR compared to PASL and an 18% increase in labeling efficiency compared to CASL.

Also, the potential of PCASL to selectively label vessels varying in size and orientation may prove invaluable in studying disease diagnosis, progression, and treatment.

1.3.2 ASL perfusion

The past decade has seen the emergence of arterial spin labeling (ASL) in perfusion MRI [33] as an approach which is less invasive and less expensive than earlier approaches using radioactive tracers or paramagnetic contrast agents. In clinical applications, ASL has been demonstrated to provide reproducible and reliable quantitative CBF measurements in the presence of various cerebrovascular disorders in the brain.

One of the main advantages of ASL perfusion is that, because ASL is noninvasive, it is safe to repeat over time and can therefore be used to track changes in CBF. Important, ASL yields an absolute measurement of CBF and therefore any change in flow can be expressed in physiologically meaningful units rather than as a % change.

In ASL perfusion, the tag images are acquired after a time delay that allows for the inverted water spins to exchange with the tissue in which the blood magnetization is fully relaxed. The signal from a given voxel in the labeled image represents a sum over both blood and tissue spins (Figure 1.2, left panel). At each imaged voxel, the difference between the control and labeled images is proportional to the amount of flow supplying that voxel. The ASL signal is typically expressed as a fractional ratio between the difference image and

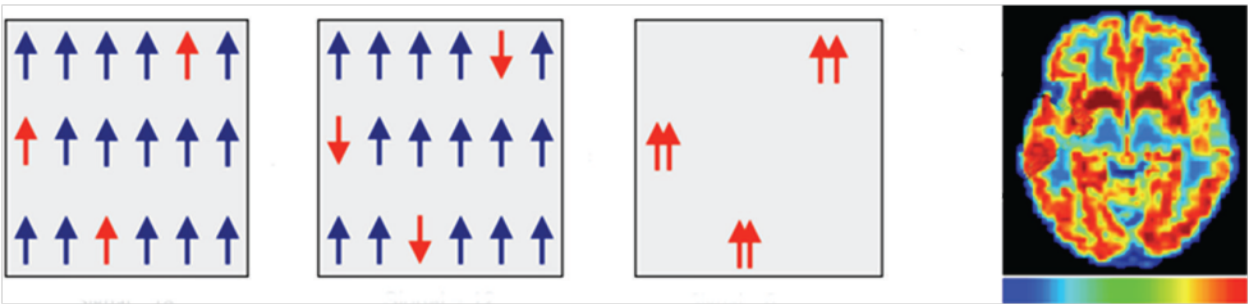

Figure 1.2: Schematic presentation of how ASL perfusion image is obtained. The first three panels represent the signal from a single imaged voxel that originates from the control (left), label (center), and control-label difference (right) panels, respectively. The difference image is converted to a single CBF image (the last right panel) via a function that includes physiological and MR parameters such as relaxation rates, transit times, and blood tissue water partition coefficient

the control image. A CBF image is computed by applying a set of measured or assumed physiological and MR parameters on the ASL signal image to obtain voxel-wise flow values in absolute physiological units of flow (Figure 1.2, right panel).

ASL perfusion is based on the theory of tracer kinetics, which was first applied for measuring CBF in humans by Kety and Schmidt in 1948 [34]. These mathematical tools were the basis of the "general kinetic model for quantitative perfusion imaging with ASL" developed by Buxton et al. [35] in which the Bloch's equation for longitudinal magnetization was modified to include delivery and clearance terms proportional to local blood flow as shown in equation:

$$\frac{dM_T(t)}{dt} = \frac{M_T^0(t)}{T_1} + f \cdot \left(\frac{\lambda M_A(t) - M_T(t)}{\lambda} \right) \tag{1.7}$$

where M_T^0 is the equilibrium magnetization of tissue, λ is the partition coefficient for water, and M_T and M_A represent the time-dependent longitudinal magnetizations of tissue and arterial blood, respectively.

Image acquisition in ASL perfusion

In ASL, generally less than 1% of the spins in a given voxel are perfused per second. And the labeled spins decay at a quick rate. These two factors contribute to the low intrinsic signal-to-noise ratio (SNR) of ASL methods. For an adequate SNR, therefore, ASL requires multiple pairs or label and control images for signal averaging, which leads to long measurement times (typically on the order of 5-10 minutes).

SNR of ASL perfusion could be improved by several ways. First, the use of higher field strengths has increased ASL signal both because of intrinsically higher SNR at high field and the lengthening of blood T1 which accompanies increased field strength. Second, the use of background suppression by the application of multiple inversion pulses can improve ASL robustness and true SNR. Furthermore, combined with parallel imaging techniques, multichannel detectors allow for increased SNR.

Due to the limitation of SNR and scan time, fast imaging techniques are often used in ASL perfusion. The most extensively used data acquisition technique echo planar imaging (EPI). Due to its extreme sensitivity to susceptibility artifacts, other acquisition techniques that are insensitive to magnetic field inhomogeneities were gaining more interest. These techniques include single-shot rapid acquisition with relaxation enhancement (RARE), gradient echo and spin echo (GRASE), half-Fourier single-shot turbo spin echo (HASTE), spoiled gradient recalled echo (SPGR) and balanced Steady State Free Precession (bSSFP).

In combination, the above methods allow for substantial improvement in SNR and acquisition speed, which can be traded off for increased spatial resolution and volume coverage. In brain imaging, With the use of multichannel detectors for ASL at 3.0 T, perfusion-weighted images can be acquired with $1.5 \times 1.5 \times 3.0 mm^3$ resolution, and perfusion images can be calculated at an SNR of 5-10 in about 11 minutes.

The recent development of PCASL, due to its high efficiency, multislice capability, and

relative ease of implementation, has contributed to a substantial increase in applications of ASL perfusion and becomes the best choice for a broad range of applications in brain research.

1.3.3 ASL angiography

Although the use of ASL for angiography began from 1980s, ASL angiography hasn't been widely used until recently. The major reason is the low SNR and long scan time. Putting aside these two limitations, there are several advantages of using ASL for angiography. First of all, ASL based angiography can easily acquire dynamic information of the flow by varying the tagging duration or post-labeling delay time. By using arterial water as an endogenous tracer, ASL is not restricted to a single pass, therefore the achievable temporal resolution is not constrained by intravenous bolus dynamics. In addition, ASL can selectively label specific vessel of interest analogous to single-vessel catheter injection as used in X-ray DSA.

The image acquisition for ASL angiography should be different from the ones for ASL perfusion. First of all, ASL angiography will be imaging the large blood vessels instead of the tissue. Therefore most of the volume of a voxel should be occupied by the labeled spins (in tag acquisition) and SNR is much higher. Secondly, aiming at vessel visualization instead of quantification of CBF, ASL angiography requires a very high spatial resolution which will compromise the SNR and dramatically increase the acquisition time for each tag or control image. Lastly, the transit time from labeling plane to large blood vessels is shorter than to perfused regions, therefore, post-labeling delay time (in PASL) and labeling duration (in CASL) could be shortened compared to perfusion imaging.

The resurgence of ASL angiography is due to the recent MRI development in hardware, fast imaging techniques, and novel labeling techniques. In intracranial vascular applications, for example, Tan [36] combined PASL and spoiled gradient echo (SPGR) for static 3D

angiography, Yan and Bi [37, 38] combined PASL and multiphase balanced steady-state free precession (bSSFP) for 4D angiography. Continuous ASL has rarely been used for angiography until the development of pseudo continuous ASL (PCASL).

PCASL-based angiography

The recent development of PCASL, due to its high efficiency, multislice capability, and relative ease of implementation, has contributed to a substantial increase in applications of CASL angiography. PCASL has been applied to angiography with Cartesian acquisition and bSSFP readout in 1.5 T scanners. Robson et al [39] implemented dynamic and vessel selective intracranial PCASL angiography with 2D thick slab (36 mm section thickness) imaging with coronal plane prescription. Each time frame requires a separate scan of 1.5-min obtaining in-plane spatial resolution of approximately $1 \times 1mm^2$. Koktzoglou et al [40] implemented static PCASL angiography with 3D bSSFP readout and applied it in extracranial carotid MRA. They were able to obtain a spatial resolution of $1 \times 1 \times 1mm^3$ and 64 mm coverage in AP direction. Although these works achieve a high spatial resolution, it's still insufficient for cerebral vasculature and the volume coverage is not large enough to cover the entire head. So it's not comparable to routine intracranial MRA technique 3D Time-of-flight (TOF).

1.4 The goal of my thesis work – Accelerating PCASL angiography

To achieve higher spatial resolution in ASL angiography, scan time is the most critical issue that determines the applicability of the technique. If using Cartesian sampling for 3D imaging, a $320 \times 320 \times 320$ image volume takes 68 min assuming a TR of 5 ms and a fully sampled k-space. Partial fourier imaging and parallel imaging could provide a combined

acceleration of 3-6 which is still insufficient for a reasonable scan time. A non-traditional sampling acquisition could provide a greater acceleration such as radial sampling.

1.4.1 Accelerated 3D Radial Acquisition

MRI was first performed with a radial trajectory [41], but it was quickly replaced by Cartesian methods due to several reasons. First, radial sampling needs $\pi/2$ times TRs than Cartesian sampling according to Nyquist theorem. Second, reconstruction of Cartesian sampled k-space only requires inverse Fourier transform which can be implemented very fast while reconstruction of radially sampled k-space needs regridding which not only needs more computation but also not robust.

The resurgence of radial trajectories came with the concept of undersampling. For most application, higher spatial resolution and/or higher temporal resolution are encouraged for more accurate and reliable diagnosis. To achieve this goal, however, is not easy due to either the long scan time (in non-contrast technique like phase contrast) or the limited sampling window (in contrast enhanced MRA). Sparse sampling of k-space has been a hot topic in the last decade and still be. While undersampling in Cartesian brings aliasing artifacts, radial sampling has very different artifacts. Undersampling in 2D radial k-space [42, 43] produces streak-like artifacts which do not obscure diagnosis in most time because the radiologist can easily distinguish them from the true signal. Peters et al [43] increased in-plane resolution by a factor of 4 relative to Cartesian techniques.

3DPR was first proposed very early in MRI [44]. Fully sampled 3DPR trajectories are not widely used because the required number of excitations is prohibitively large. Although the artifact resulting from undersampling the 3DPR trajectory is structured, this aliased energy resembles noise more than coherent streaks as in 2D PR. Therefore, vastly undersampling the number of projections in a 3DPR trajectory can be used to limit the scan time without

compromising coverage or resolution. This technique is termed "Vastly undersampled Isotropic Projection Reconstruction" (VIPR) [45]. VIPR trajectory is shown in Figure 1.3. Data is acquired in a 3D spherical coordinate system, with the readout direction defined by the angle θ from the kz –axis and by the angle ϕ from the ky –axis. The trajectory consists of a series of evenly spaced projections with all projections going through the origin of k-space. The maximum k-space radius determines the resolution in all three spatial directions. The radial sample spacing (Δk_r) determines the diameter of the full FOV. For time resolved applications, the projection acquisition order is interleaved so that spatial frequency orientations throughout the sphere are sampled on an interval equal to the desired frame rate. Sliding window is usually used for reconstruction.

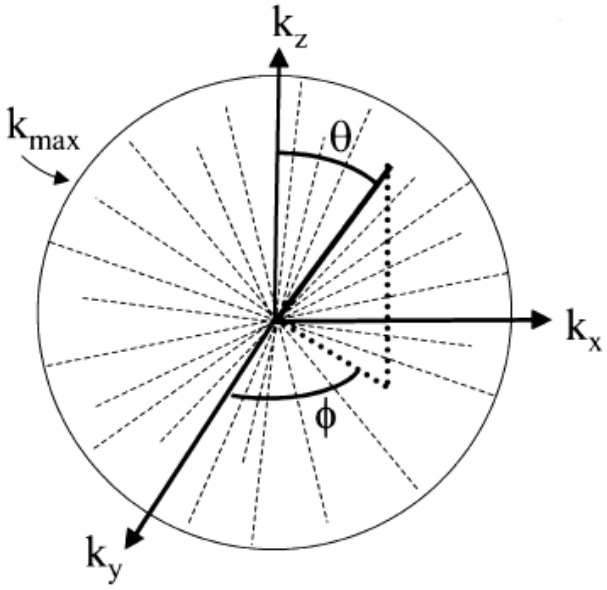

Figure 1.3: Diagram of the K-space trajectory for VIPR. The endpoints of the projections sample evenly on the surface of a sphere in k-space. Image taken from Barger [45]

1.4.2 Combining PCASL with VIPR

VIPR is especially suited for MRA acquisitions as those are usually characterized by high contrast and sparse data distribution due to inherent background suppression or subtraction or T1 shortening contrast agent. VIPR has been utilized in 3D CE-MRA and 3D phase contrast MRA and demonstrated ability of acceleration. For PCASL angiography, the subtraction of tag and control image generates a highly sparsed image volume which supports high undersampling factor.

In addition to acceleration ability, there are two more benefits of VIPR. First, VIPR provides a large spherical imaging volume that covers the entire volume of interest, rather than a carefully oriented slab over the tissue of interest. Second, the symmetry of the 3D radial acquisition sampling strategy also provides isotropic resolution, allowing for reformats at any orientation without sacrifice in spatial resolution.

As applied for PCASL angiography, 3D radial sampling has a unique advantage over Cartesian sampling: the robustness to contrast modulation. During the acquisition window, there are contrast changes coming from various sources. For static imaging, while the acquisition starts after the vasculature has been fully filled, the inverted spins experienced T1 recovery and saturation from repetitive RF pulses during readout. This signal behavior approximately follows an exponential decay curve for spins in the volume. Previous work with Cartesian angiography [36] and fast spin echo imaging have well characterized the response to the decay as a low pass filter apodization in k-space. This is not the case with 3D radials. With inconsistent data for radials, signal decay manifests as increased undersampling artifacts (noise-like). For dynamic imaging, additional contrast change is due to the bolus advancing during the readout. In Cartesian acquisition, this inconsistency of contrast expresses as ghost artifacts in images. While in radial sampling, the bolus advancing expresses as blurred bolus edge in its advancing directon. The advantageous robustness to contrast modulation of 3D

radial sampling is due to the fact that the contrast change is evenly distributed between the edge and center of k-space and the center of k-space is sampled in every TR.

1.5 References

[1] Stephen L. Ondra, Henry Troupp, Eugene D. George, and Karen Schwab. The natural history of symptomatic arteriovenous malformations of the brain: a 24-year follow-up assessment. *Journal of Neurosurgery*, 73(3):387–391, 1990. PMID: 2384776.

[2] HJ Cloft, GJ Joseph, and JE Dion. Risk of cerebral angiography in patients with subarachnoid hemorrhage, cerebral aneurysm, and arteriovenous malformation. *Stroke*, 30:317âŁ“320, 1999.

[3] MR Prince, T. M. Grist, and Debatin J.F. *3D Contrast MR Angiography*. Springer, Berlin, 2003.

[4] F. R. Korosec, R. Frayne, and T. M. Grist. Time-resolved contrast-enhanced 3d mr angiography. *Magn Reson Med*, 36:345–351, 1996.

[5] Yingbiao Xu and E. Mark Haacke. Partial fourier imaging in multi-dimensions: A means to save a full factor of two in time. *Journal of Magnetic Resonance Imaging*, 14(5):628–635, 2001.

[6] Daniel K. Sodickson and Warren J. Manning. Simultaneous acquisition of spatial harmonics (smash): Fast imaging with radiofrequency coil arrays. *Magnetic Resonance in Medicine*, 38(4):591–603, 1997.

[7] Klaas P. Pruessmann, Markus Weiger, Markus B. Scheidegger, and Peter Boesiger. Sense: Sensitivity encoding for fast mri. *Magnetic Resonance in Medicine*, 42(5):952–962, 1999.

[8] Mark A. Griswold, Peter M. Jakob, Robin M. Heidemann, Mathias Nittka, Vladimir Jellus, Jianmin Wang, Berthold Kiefer, and Axel Haase. Generalized autocalibrating partially parallel acquisitions (grappa). *Magnetic Resonance in Medicine*, 47(6):1202–1210, 2002.

[9] C.A. Mistretta, O. Wieben, J. Velikina, W. F. Block, J. Perry, Y. Wu, and K. M. Johnson. Highly constrained backprojection for time-resolved mri. *Magn Reson Med*, 55:30–40, 2006.

[10] KM Johnson, J Velikina, Y Wu, SR Kecskemeti, O Wieben, and CA Mistretta. Improved waveform fidelity using local hypr reconstruction (hypr lr). *Magn Reson Med*, 2008:456–462, 2008.

[11] P. Marckmann, L. Skov, K. Rossen, A. Dupont, M.B. Damholt, J.G. Heaf, and H.S. Thomsen. Nephrogenic systemic fibrosis: suspected causative role of gadodiamide used for contrast-enhanced magnetic resonance imaging. *J Am Soc Nephrol*, 17:2359–2362, 2006.

[12] M. Miyazaki and M. Akahane. Non-contrast enhanced mr angiography: Established techniques. *J Magn Reson Imaging*, 35(1):1–19, 2012.

[13] CL Dumoulin, SP Souza, MF Walker, and W. Wagle. Three-dimensional phase contrast angiography. *Magn Reson Med*, 9:139–49, 1989.

[14] C.L. Dumoulin, H.E. Cline, S. P. Souza, W.A. Wagle, and M.F. Walker. Three-dimensional time-of-flight magnetic resonance angiography using spin saturation. *Magn Reson Med*, 11:35–46, 1989.

[15] W.T. Dixon, L.N. Du, D.D. Faul, M. Gado, and S. Rossnick. Projection angiograms of blood labeled by adiabatic fast passage. *Magn Reson Med*, 3:454–462, 1986.

[16] D. G. Nishimura, A. Macovski, J. M. Pauly, and S. M. Conolly. Mr angiography by selective inversion recovery. *Magn Reson Med*, 4(2):193–202, 1987.

[17] SE Kim and DL Parker. *Magnetic Resonance Angiography: Principles and Applications*. Springer, 2011.

[18] D. L. Parker, C. Yuan, and D. D. Blatter. Mr angiography by multiple thin slab 3d acquisition. *Magn Reson Med*, 17:434–451, 1991.

[19] D Atkinson, M Brant-Zawadzki, G Gillan, D Purdy, and G Laub. Improved mr angiography: magnetization transfer suppression with variable flip angle excitation and increased resolution. *Radiology*, 190(3):890–894, 1994.

[20] K.M. Johnson, D.P. Lum, P.A. Turski, W. F. Block, C.A. Mistretta, and O Wieben. Improved 3d phase contrast mri with off-resonance corrected dual echo vipr. *Magn Reson Med*, 60(6):1329–1336, 2008.

[21] D.S. Williams, J.A. Detre, J.S. Leigh, and A.P. Koretsky. Magnetic resonance imaging of perfusion using spin inversion of arterial water. *Proc. Natl. Acad. Sci. USA*, 89:212–216, 1992.

[22] D C Alsop and J A Detre. Multisection cerebral blood flow mr imaging with continuous arterial spin labeling. *Radiology*, 208(2):410–416, 1998.

[23] K.K. Kwong, D.A. Chesler, R.M. Weisskoff, K.M. Donahue, T.L. Davis, L. Ostergaard, T.A. Campbell, and B.R. Rosen. Mr perfusion studies with t1-weighted echo planar imaging. *Magn Reson Med*, 34:878–887, 1995.

[24] S. G. Kim. Quantification of relative cerebral blood flow change by flow-sensitive alternating inversion recovery (fair) technique: application to functional mapping. *Magn Reson Med*, 34(3):293–301, 1995.

[25] C. Schwarzbauer, S.P. Morrissey, and A. Haase. Quantitative magnetic resonance imaging of perfusion using magnetic labeling of water proton spins within the detection slice. *Magnetic resonance in medicine*, 35(4):540–546, 1996.

[26] R. R. Edelman, B. Siewert, M. Adamis, J. Gaa, G. Laub, and P. Wielopolski. Signal targeting with alternating radiofrequency (star) sequences: application to mr angiography. *Magn Reson Med*, 31(2):233–238, 1994.

[27] Eric C. Wong, Richard B. Buxton, and Lawrence R. Frank. Implementation of quantitative perfusion imaging techniques for functional brain mapping using pulsed arterial spin labeling. *NMR in Biomedicine*, 10(4-5):237–249, 1997.

[28] X. Golay, M. Stuber, K.P. Pruessmann, D. Meier, and P. Boesiger. Transfer insensitive labeling technique (tilt): application to multislice functional perfusion imaging. *Journal of Magnetic Resonance Imaging*, 9(3):454–461, 1999.

[29] D.M. Garcia, C de Bazelaire, and D.C. Alsop. Pseudo-continuous flow driven adiabatic inversion for arterial spin labeling. *proc. Intl. Soc. Mag. Reson. Med. 13*, page 37, 2005.

[30] W Dai, D Garcia, C de Bazelaire, and DC Alsop. Continuous flow-driven inversion for arterial spin labeling using pulsed radio frequency and gradient fields. *Magn Reson Med*, 60(6):1488–1497, 2008.

[31] EC Wong. Vessel-encoded arterial spin-labeling using pseudocontinuous tagging. *Magn Reson Med*, 58(6):1086–1091, 2007.

[32] W Wu, M Fernandez-Seara, J.A. Detre, F.W. Wehrli, and J Wang. A theoretical and experimental investigation of the tagging efficiency of pseudocontinuous arterial spin labeling. *Magn Reson Med*, 58:1020–1027, 2007.

[33] J.A. Detre. Arterial spin labeled perfusion mri. *Clinical Neurology*, 2008.

[34] S. Kety and C. Schmidt. The nitrous oxide method for the quantitative determination of cerebral blood flow in man: theory, procedure and normal values. *The Journal of Clinical Investigation*, 27:476–483, 1948.

[35] R.B. Buxton, L.R. Frank, E.C. Wong, B. Siewert, S. Warach, and R.R. Edelman. A general kinetic model for quantitative perfusion imaging with arterial spin labeling. *Magnetic resonance in medicine*, 40(3):383–396, 2005.

[36] ET Tan, J III Huston, NG Campeau, and SJ Riederer. Fast inversion recovery magnetic resonance angiography of the intracranial arteries. *Magn Reson Med*, 63:1648–1658, 2010.

[37] L Yan, S Wang, Y Zhuo, RL Wolf, MF Stiefel, J An, Y Ye, Q Zhang, ER Melhem, and DJJ Wang. Unenhanced dynamic mr angiography: High spatial and temporal resolution by using true fisp - based spin tagging with alternating radiofrequency. *Radiology*, 256(1):270–279, 2010.

[38] X Bi, P Weale, P Schmitt, S Zuehlsdorff, and R Jerecic. Non-contrast-enhanced four-dimensional (4d) intracranial mr angiography: A feasibility study. *Magn Reson Med*, 63:835–841, 2010.

[39] PM Robson, W Dai, A Shankaranarayannan, NM Rofsky, and DC Alsop. Time-resolved vessel-selective digital subtraction mr angiography of the cerebral vasculature with arterial spin labeling. *Radiology*, 257(2):507–515, 2010.

[40] I Koktzoglou, N Gupta, and RR Edelman. Nonenhanced extracranial carotid mr angiography using arterial spin labeling: improved performance with pseudocontinuous tagging. *J Magn Reson Imaging*, 34(2):384–394, 2011.

[41] P Lauterbur and C-M Lai. Zeugmatography by reconstruction from projections. *IEEE Trans Nucl Sci*, NS-27:1227–1231, 1980.

[42] V Rasche, R.W. de Boer, D Holz, and R Proksa. Continuous radial data acquisition for dynamic mri. *Magn Reson Med*, 34:754–761, 1995.

[43] D. C. Peters, F. R. Korosec, T. M. Grist, W. F. Block, J. E. Holden, K. K. Vigen, and C. A. Mistretta. Undersampled projection reconstruction applied to mr angiography. *Magnetic Resonance in Medicine*, 43(1):91–101, 2000.

[44] CM Lai and PC Lauterbur. True three-dimensional image reconstruction by nuclear magnetic resonance zeugmatography. *Phys Med Biol*, 26:851–856, 1981.

[45] AV Barger, WF Block, Y Toropov, TM Grist, and CA Mistretta. Time-resolved contrast-enhanced imaging with isotropic resolution and broad coverage using an undersampled 3d projection trajectory. *Magn Reson Med*, 48:297–305, 2002.

2 Static Intracranial angiography with PCASL-VIPR

Intracranial MRA is most frequently performed with three-dimensional time-of-flight (3D TOF) in clinical routine. This technique provides relatively high spatial resolution, however is limited by the saturation of spins in slow, complex, or in-plane flow [1] and provides limited information of vessel filling patterns.

Recently developed ASL strategy pseudo continuous arterial spin labeling (PCASL) is of particular interest for intracranial applications. PCASL has been demonstrated to provide significantly higher arterial signal compared with PASL and improve diagnostic confidence [2]. PCASL also holds the potential to provide hemodynamic information and label the selected vessels similar to X-ray DSA [3, 4]. Unfortunately, current intracranial angiography is limited to 2D projection imaging or low-resolution 3D imaging due to scan time limitations. For example, recent 2D projection imaging has required 11 s per slice [3], which translates to scan times over 30 min for true 3D imaging even with parallel imaging.

In this chapter, an accelerated PCASL-based 3D MRA technique was presented as follows: first, the sequence design was described; then the validation with in-vivo study was presented in details; in the following two sections the preliminary studies about vessel selective imaging and tagging efficiency were briefly shown; at last the whole study was discussed and concluded. This part of work has been published [5]

2.1 Static PCASL-VIPR Sequence design

PCASL angiography is performed with an interleaved acquisition set to two tagging states, control and label, which are subtracted to yield an angiographic image. Each tag session consists of four modules: background saturation, PCASL, PASL, and imaging, as illustrated in Figure 2.1.

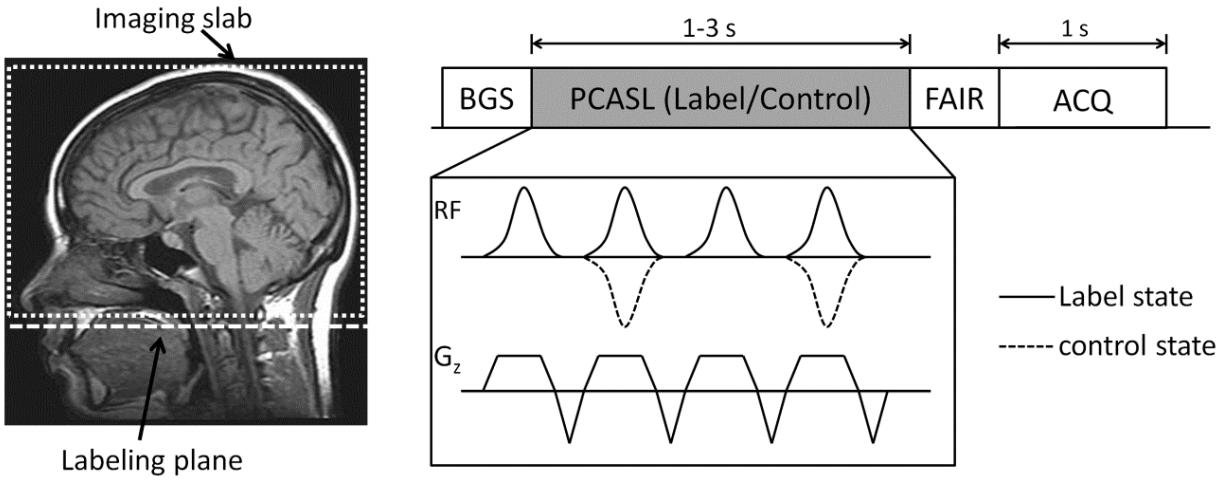

Figure 2.1: Labeling geometry (left); PCASL-VIPR sequence diagram (right) shows a tag session consisting of four modules: background suppression (BGS), PCASL, FAIR and image acquisition with time assignment. PCASL is set to label state or control state to acquire the label image and the control image respectively.

For background suppression, we used a variable rate selective excitation (VERSE) transformed hyperbolic secant pulse [6] to selectively invert the imaging slab. This helps to reduce the signal from cerebrospinal fluid and other background tissue that give rise to artifacts.

The PCASL module was implemented following a balanced gradient approach [7] using a train of pulsed radiofrequency (RF) and gradients as illustrated in Figure 2.1. In the label state, the RF phase cycling is set such that spins at the labeling plane see RF pulses with the same phase. In this condition the spins passing through this labeling plane undergo adiabatic inversion. In the control state, the RF pulse train and the gradients are the same as in the label state, while the RF phase is cycled such that spins at the labeling plane see RF pulses

having a phase of π relative to the previous pulse, leading to limited effect on the passing spins. In our implementation, a Hanning window-shaped RF pulse of 500 us duration was performed periodically with a 1200 μs spacing between RF pulses. The amplitude of the RF pulse and gradients were optimized using Bloch simulation to get a labeling efficiency greater than 95%. The parameters we used in this study are as follows: average gradient=0.78 mT/m, maximum gradient = 7 mT/m, average B1=1.63 μT.

At the end of PCASL labeling, inflowing spins superior to the labeling plane are inverted. However, fresh spins will displace labeled spins during the imaging module causing signal loss in proximal vessels. This could be avoided by setting a large gap between the labeling plane and the inferior edge of the image region. However, this will lead to substantial reduction in SNR and adds a transit time parameter that will vary from subject to subject depending on the flow velocity. To avoid signal loss with SNR penalty we incorporate a PASL scheme at the end of PCASL to ensure a continued inflow of labeled blood during image acquisition. In our study, flow-alternating-inversion-recovery [8] is implemented such that a selective inversion pulse is applied on the imaging slab in label state, while a global inversion pulse in control state.

Both bSSFP and SPGR have been utilized for non-contrast angiography and can be used as readout with PCASL. bSSFP provides substantially higher signal; however bSSFP is highly sensitive to off-resonance, leads to high SAR, and can be sensitive to flow related artifacts [9]. Off-resonance artifact are a particular issue in intracranial applications, due to susceptibility at the skull base and nasal fossa, movement of spins through the off-resonant field, and higher utilization of 3T scanners. To avoid these artifacts, the acquisition module consists of a low flip angle SPGR readout combined with a VIPR sampling strategy.

The VIPR sequence samples data along radial lines evenly spaced through a spherical volume each intersecting the origin of k-space. For PCASL angiography, VIPR has two major advantages over Cartesian acquisitions. First, undersampling artifacts appear as a

diffuse low level background noise rather than ghosting artifacts in Cartesian acquisitions [10] . This allows for undersampling acceleration when the image is sparse. The subtractive nature of PCASL creates a highly sparse imaging volume allowing the high acceleration factors needed to keep the scan time in a clinical acceptable range for 3D scans. Second, 3D radial sampling is more robust to contrast changes during the acquisition. During the readout, the signal experience T1 recovery and RF saturation due to repetitive RF pulses. This signal behavior approximately follows the exponential decay curve for spins in the volume. Previous work with Cartesian angiography [11] and fast spin echo imaging have well characterized the response to the decay as an apodization in k-space, which results in the loss of spatial resolution. For 3D radial acquisition, the signal modulation leads to an increased angular undersampling artifact in the image as demonstrated in previous applications of radial acquisition for hyperpolarized He3 magnetic resonance imaging [12] and fast spin echo [13, 14]. This is merely due to the fact that the decay is evenly distributed between the edge and center of the k-space. The additional diffuse artifacts have no effects on the image resolution, which makes VIPR advantageous for angiography where high resolution is critical.

2.2 In-vivo study and image results

5 healthy volunteers (1 women, 4 men, age range 25-35) and 5 patients with previously diagnosed AVMs (N=3) or aneurysms (N=2) were imaged after obtaining Institutional Review Board (IRB) approval and informed consent. All exams were performed on a clinical 3T MR system(Discovery 750, GE Healthcare, Waukesha, WI, USA) with a 32-channel head coil (Nova Medical, Wilmington, MA, USA). Subjects were imaged with a clinical standard 3D TOF scan and a whole brain PCASL-VIPR scan. The standard 3D TOF scan was acquired with the following parameters: TR/TE 30/2.8; field of view (FOV) 22x22 cm2; matrix 512x256; slice thickness 1mm; flip angle 20; bandwidth ±41.67 kHz; slabs 4; slab thickness

40mm; overlap thickness 10mm; pparallel imaging method SENSE (ASSET; GE Healthcare) with an acceleration factor of 2X. For partial head coverage of 11 cm, the examination time was 8:01 minutes.

For PCASL-VIPR scan, a 16cm-thick imaging slab was prescribed covering the whole brain. The labeling plane was positioned at the inferior edge of the imaging slab. PCASL-VIPR parameters include: labeling duration 3 s; image acquisition window 1 s; FOV 22×22×16 cm3 ; 3D isotropic resolution 0.68 mm; readout bandwidth ±62.50 kHz; fractional echo 0.75; flip angle 10 ˚. A total of 12,000 projections were collected in a scan time of 8:27 minutes. Compared to Nyquist this represents a 13x undersampling. PCASL-VIPR images were reconstructed utilizing an optimized gridding routine [15] zero-filled to 0.46mm isotropic resolution. Individual coil images were combined utilizing coil sensitivities estimated from the center of k-space [16]. This coil combination helps reduce undersampling artifacts as in partially parallel imaging (PILS) [17] and leads to more optimal SNR in the final image [18].

Figure 2.2 shows representative PCASL-VIPR images obtained in a healthy subject. With near-zero background, whole volume Maximum-Intensity-Projection (MIP)s could be generated at any angle. The axial, coronal, and sagittal collapsed views are presented. High spatial resolution enables visualization of small distal arteries not generally seen with CE MRA. Signal intensity decays from proximal to distal vessels due to T1 recovery and RF saturation. Whole brain coverage is achieved with a 16-cm slab thickness.

Figure 2.3 shows results of a patient with a thalamic AVM with deep venous drainage. Limited MIPs in the sagittal view of the same thickness and location were performed for the source images of both PCASL-VIPR and 3D TOF. Images were cropped to compare with DSA image which was also performed for this patient as the reference standard. The images show increased flow through the left posterior cerebral artery and the venous drainage into the vein of Galen. The structures of the AVM were equally visualized in both exams with delineation of the main feeding arteries confirmed by DSA. However, severe signal loss in the

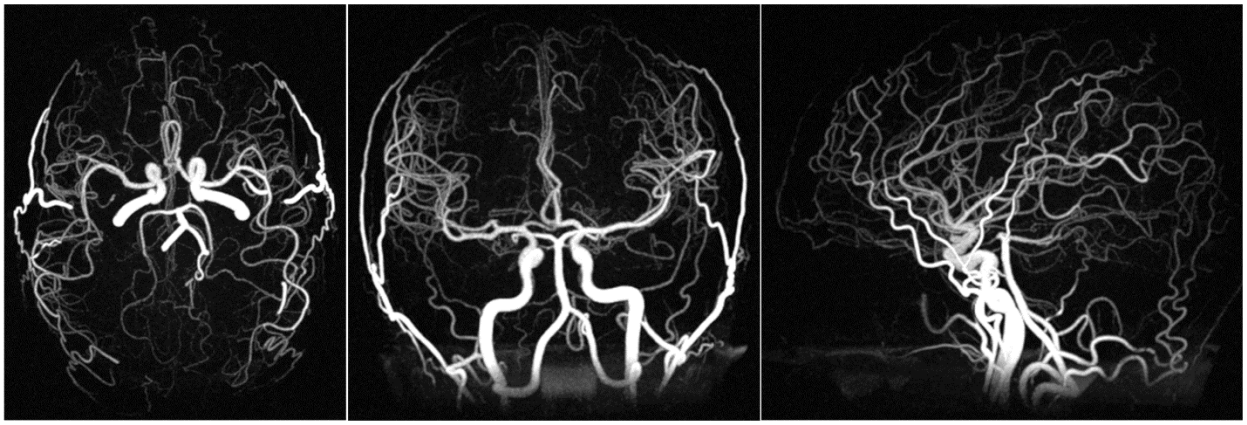

Figure 2.2: Axial, coronal and sagittal MIPs of PCASL-VIPR of a Healthy subject. Images show complete filling of the entire arterial vasculature of the brain. Signal intensity decreases from proximal to distal vessels due to increasing transit time from the labeling plane.

draining vein due to saturation can be observed in the TOF image.

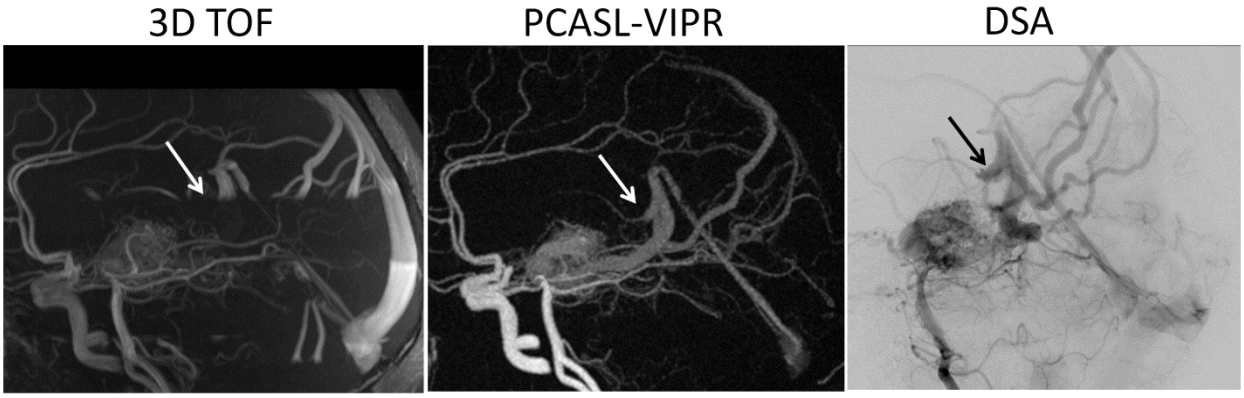

Figure 2.3: Thalamic AVM patient: sagittal limited MIPs of 3D TOF (left), PCASL-VIPR (middle) and DSA (right). The arrows point to the venous drainage of the AVM into the vein of Galen. MIP image of 3D TOF show severe signal loss in the draining vein due to saturation artifacts.

Figure 2.4 shows results of a patient with left frontal AVM. As demonstrated in the limited sagittal MIP images of both exams, there is increased flow in the left anterior cerebral artery indicating that it is the dominant supply to the AVM. However, there is still mild signal loss due to saturation in the feeding arteries in the TOF image. The superficial venous drainage can be observed in both exams.

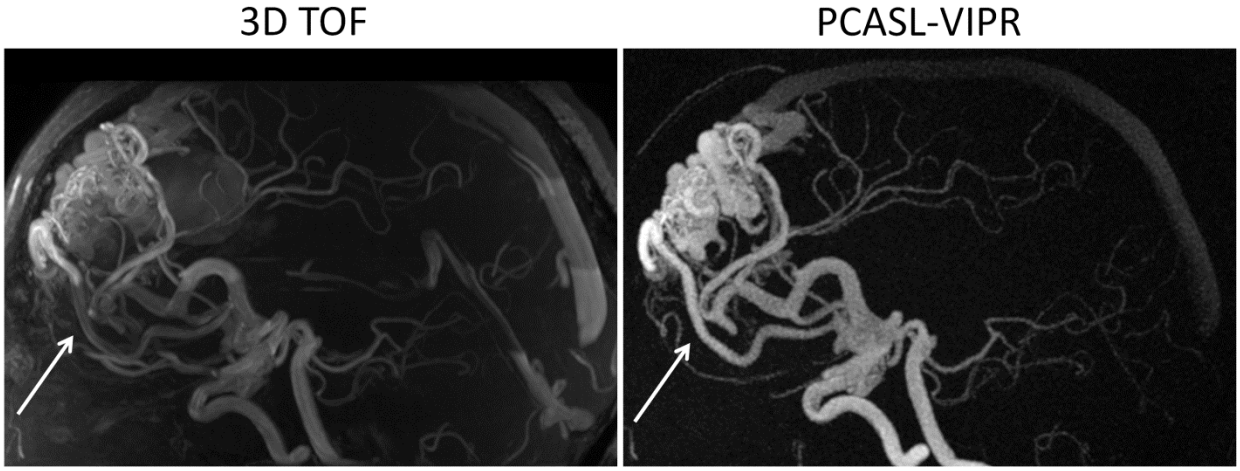

Figure 2.4: Left frontal AVM patient: sagittal limited MIPs of 3D TOF (left) and PCASL-VIPR (right). The arrows point to the major feeding arteries of the AVM. Saturation artifacts can be observed in the feeding arteries in TOF image. Additionally, non-shunted veins, such as the vein of Galen (right arrow), appear on TOF but are not present on 3D PCASL.

Figure 2.5 shows results of a patient with a large aneurysm arising from the left cavernous internal carotid artery. Limited coronal MIPs of both exams are shown at the aneurysm location. A profile was drawn along a horizontal line (indicated with a white line) through the aneurysm for the two MIP images. Signal intensity was scaled for the two profiles to be compared together. The profile of TOF shows signal drop both in the region of the aneurysm and the left carotid artery compared to the left side. This is likely due to saturation artifacts due to the slow, recirculating flow inside the aneurysm. In the profile of PCASL-VIPR, signal is more uniform in the aneurysm and the signal drop due to slow flow is less compared to TOF. The basilar artery region shows weaker signal due to the inappropriate placing of the labeling plane (more inferior than usual). With proper adjustment of the labeling plane, higher signal in the aneurysm could have been obtained as well.

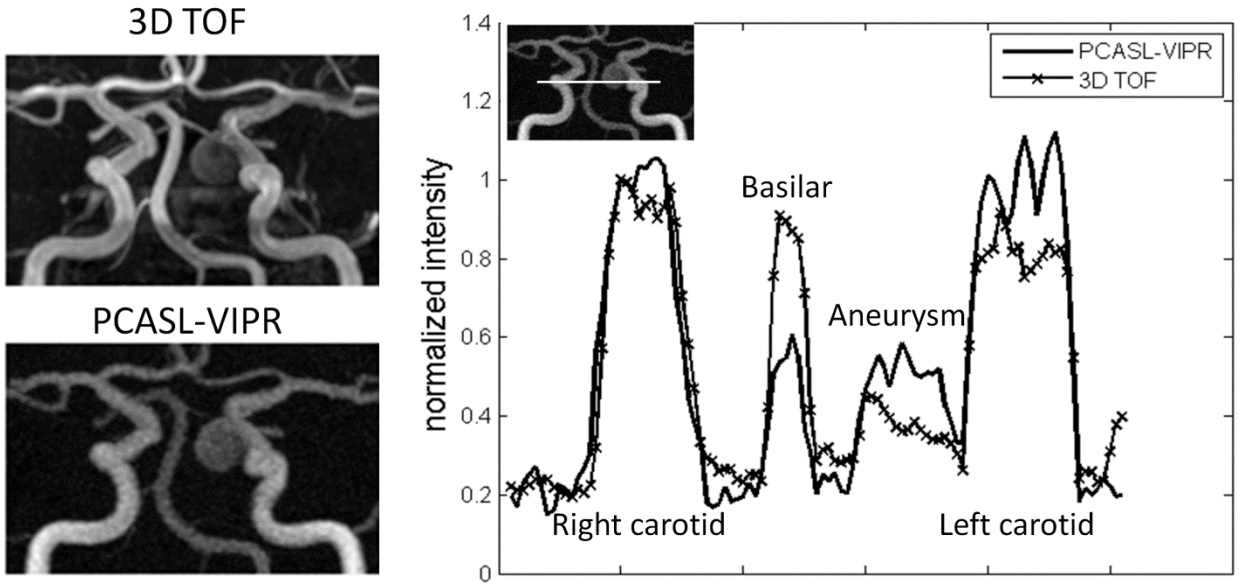

Figure 2.5: Patient with an aneurysm arising from the left cavernous internal carotid artery: cropped coronal limited MIPs of 3D TOF (upper) and PCASL-VIPR (lower). PCASL-VIPR image shows stronger and more uniform signal inside the aneurysm and less blurring artifacts around it. The right figure shows the profile along the horizontal line across the aneurysm indicated in the left upper corner small image. Different vessels are labeled in the profile. 3D TOF profile (starred line) shows signal drop in the aneurysm and left carotid due to saturation of slow and recirculating flow. PCASL-VIPR shows weaker signal in the aneurysm and basilar artery due to the placing of the labeling plane.

2.3 Qualitative and quantitative evaluation of in-vivo study

Images from 3D TOF and PCASL-VIPR were evaluated quantitatively and qualitatively. For qualitative evaluation of image quality, two experienced readers in neurovascular imaging were presented with source images from both 3D TOF and PCASL-VIPR scans on a PACS workstation. PCASL-VIPR and 3D TOF examinations were evaluated using two criteria (vessel visualization and saturation artifacts), defined on a four-point scale (Table 2.1). Eight vessel segments were evaluated for each subject, while pathology was evaluated only for the patients. Supported by a strong inter-operator correlation (Pearson correlation value is 0.8),

the scores of two readers were averaged. The nonparametric Wilcoxon signed rank method was used to test for a significant difference in image quality between PCASL-VIPR and 3D TOF for each criterion, where $P<0.05$ was taken to be statistically significant.

Criterion	**Interpretation**	**Score**
Vessel Visualization	*Non-Diagnostic or Not Visible*	1
	Poor (Structures visible, but with significant blurring or artifacts, non diagnostic)	2
	Good (Good quality diagnostic information, minimal blurring or artifacts)	3
	Excellent (Excellent quality diagnostic information, sharply defined borders)	4
Saturation artifacts	*Severe signal dropouts. Not diagnostic.*	1
	Moderate signal dropouts. Loss of diagnostic accuracy.	2
	Minimal presence of signal dropouts. Does not interfere with diagnostic interpretation.	3
	No significant saturation artifacts.	4

Table 2.1: Criteria for qualitative evaluation.

Table 2.2 summarizes the results from the qualitative evaluation. For vessel visualization, PCASL-VIPR was superior in three of the eight vessel groups and pathology (positive values) while 3D TOF was slightly better in the left five vessel groups (negative values). However, there was no statistical significance between any of these groups. For saturation artifacts, PCASL-VIPR was superior in four of the eight vessel groups and in the delineation of pathological conditions with a statistically significant advantage in visualization of the siphons (bold and underscored). 3D TOF was superior with no statistical significance in the remaining vessel comparisons. The scores were also averaged over all the evaluated vessel segments excluding pathology, and PCASL-VIPR performs slightly better in both criteria with no statistical significance.

For quantitative evaluation, regions of interest (ROIs) were placed on the source images of the five healthy subjects on the following locations: siphons (left/right), basilar tip, carotid

Vessel Segments	***Vessel Visualization (1-4)***			***Saturation Artifacts(1-4)***		
	TOF	PCASL	PCASL-TOF*	TOF	PCASL	PCASL-TOF*
Anterior cerebral artery	3.25	3.10	-0.15	3.20	3.25	0.05
Right posterior cerebral artery	3.22	3.11	-0.11	3.22	3.06	-0.16
Left posterior cerebral artery	3.10	3.05	-0.05	3.15	3.05	-0.10
Right middle cerebral artery	3.35	3.30	-0.05	3.35	3.25	-0.10
Left middle cerebral artery	3.35	3.30	-0.05	3.35	3.25	-0.10
Basilar tip	3.40	3.45	0.05	3.35	3.50	0.15
Right siphon	3.30	3.60	0.30	3.30	3.85	**0.55**
Left siphon	3.25	3.60	0.35	3.30	3.85	**0.55**
Pathology	2.80	3.50	0.70	3.00	3.60	0.60
All the above vessels excluding pathology	3.28	3.32	0.04	3.28	3.39	0.11

Table 2.2: Results of qualitative evaluation.

terminus (left/right), first bifurcation of middle cerebral artery (left/right), 5-mm-region around the anterior communicating artery, and background tissue. Contrast-to-noise ratio (CNR) were measured with equation CNR=(V-B)/σ, where V represents the maximum signal in ROIs, B represents the average signal in background ROIs, and σ is the standard deviation of the signals in background ROIs. For PCASL-VIPR images, σ includes the noise and also undersampling artifacts which have noise-like appearance. The student's t test was performed to test for a significant difference in mean CNR between PCASL-VIPR and 3D TOF for each vessel groups.

Figure 2.6 shows the average CNR (mean $\pm$ SD) of PCASL-VIPR and 3D TOF across all subjects' vessel segment ROIs. Compared to 3D TOF, PCASL-VIPR shows higher CNR in the siphons and basilar artery (starred) with statistical significance (p value <0.05) and equal values in the others. The CNR values are also more consistent across the subjects in PCASL-VIPR. In addition, PCASL-VIPR shows a trend of signal diminishing from the

siphons to the anterior cerebral arteries with increasing transit time.

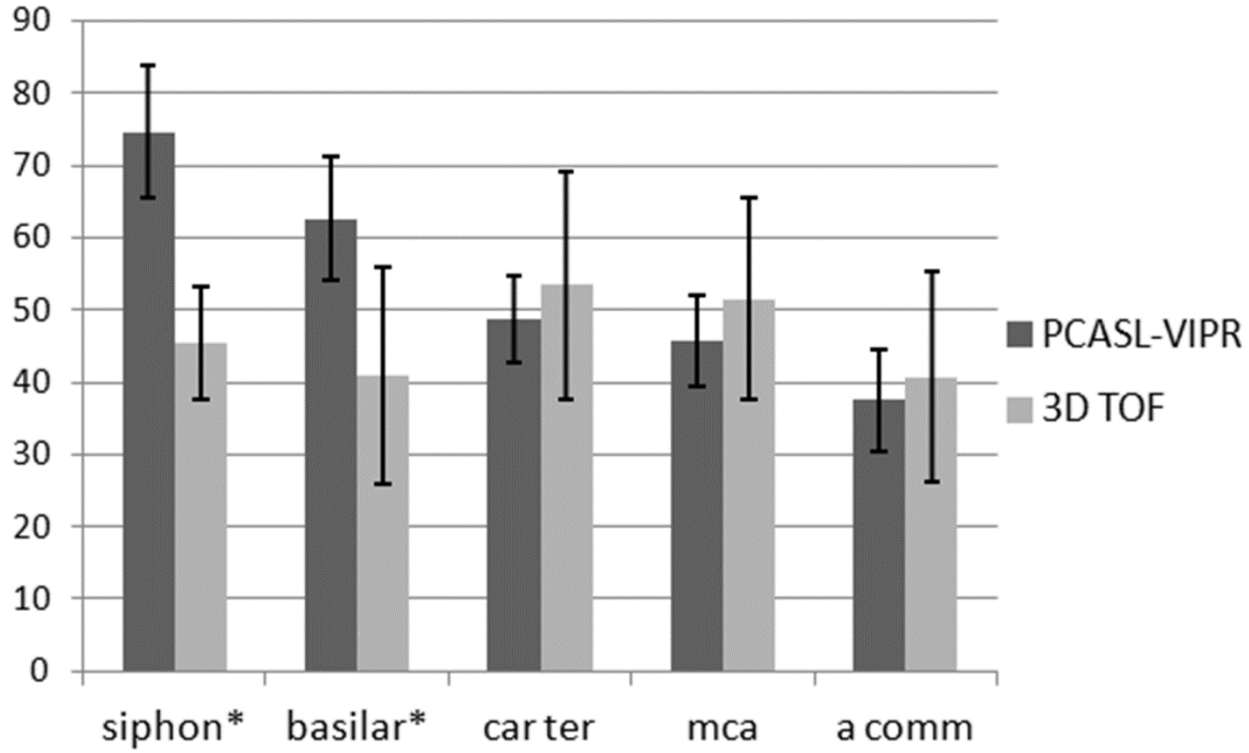

Figure 2.6: CNR (mean ± SD) graph of PCASL-VIPR and 3D TOF measured from five ROIs: left/right siphons, basilar tip, left/right carotid terminus (car ter), first bifurcation spot of the middle cerebral arteries (mca) and 5-mm-region around the anterior communicating artery (a comm). CNR of PCASL-VIPR is higher than 3D TOF in siphons and basilar tip (starred) with statistical significance tested by t test. It also shows signal decreases in moving from proximal to distal vessels. CNR of 3D TOF shows no information of flow patterns, and the standard deviation is higher (less consistent across the subjects).

2.4 Vessel selective PCASL-VIPR and preliminary results

In patients with cerebrovascular steno-occlusive disease, the presence of collateral circulation is essential to maintain cerebral perfusion, metabolism, and function. Therefore, the ability to assess the presence or absence of collateral flow is important for both prognosis and

therapeutic decision making. In diseases such as arteriovenous malformations and tumors, Information about the source of the blood supply to a particular vascular territory can also be important.

Compared to pulsed ASL, continuous ASL methods can provide simpler and more precise labeling of selected vessels. Multiple approaches to achieving such selective labeling have been proposed. A famous one was introduced by Werner et al.[19] in which the labeling plane is tilted and rotated such that only blood flow in the neighborhood of a single point could be efficiently labeled.

Since PCASL introduced gaps between RF pulses, additional gradients can be added to localize labeling without tilting the labeling plane. Wong has reported a strategy to encode all vessels of interest, using Hadamard-type encoding based on PCASL. To achieve this encoding, images are acquired with fixed gradients perpendicular to the labeling plane added. While this approach is efficient for characterizing flow through all vessels, it requires a relatively complex geometric prescription of the scan and may require measurement of labeling efficiencies of each vessel to correct for imperfect Hadamard encoding.

Another selective labeling method which labels one individual artery at a time was proposed by Dai [20]. This method only requires the relative location of the targeted vessel to iso-center at the tagging plane as extra input. In the method, rotating in-plane gradients are added in between the RF pulses to achieve localized labeling while spoiling the undesired labeling of other vessels.

Single artery PCASL method

With longitudinal gradient, PCASL tags all the spins that cross the tagging plane. According to single artery PCASL method [20], the tagging can be limited to a small disc by adding in-plane rotating gradient in the gaps between the RF pulse. Modified PCASL which tags

one artery at a time is shown in Figure 2.7.

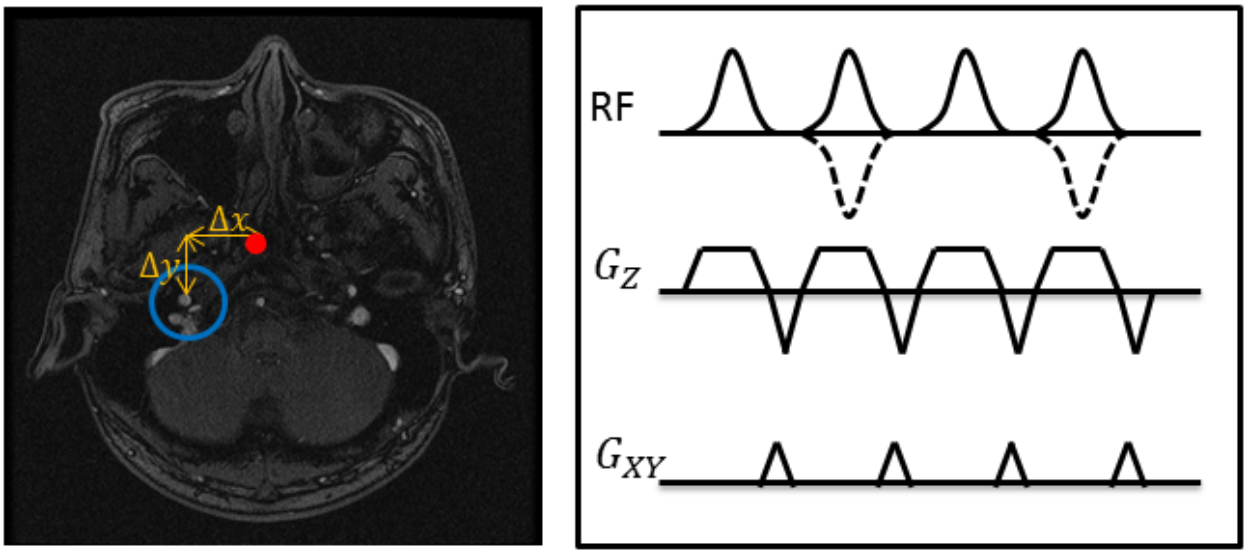

Figure 2.7: Vessel-selective PCASL diagram. Left: axial slice image for vessel location measurement, blue circle (target artery: right carotid), red dot is the iso-center, yellow measurements are the location of the target artery relative to the iso-center. Right: RF pulse train and gradient pulse train utilized in single artery PCASL.

First of all, an axial slice image at the tagging position is picked. Then, the location of the target artery relative to the iso-center is measured and work as the center of the selective labeling disk. In PCASL sequence, each RF pulse must be incremented in phase relative to the prior pulse by an amount determined by the applied gradients and the desired labeling center. The phase shift is given by:

$$\Delta\psi = \gamma G_{zave}\Delta z\Delta t + \gamma G_{xave}\Delta x\Delta t + \gamma G_{yave}\Delta y\Delta t \tag{2.1}$$

where *gamma* is the gyromagnetic ratio, Δt is the time spacing between the center of two RF pulses; G_{zave},G_{xave}, and G_{yave} are the time averaged gradients between the center of two RF pulses along z, x, and y directions, respectively. Δz is the longitudinal offset distance from the iso-center to the labeling plane. Δx is the projection distance of the segment from

the isocenter to the target vessel along the gradient x direction, and Δy is the projection distance along the gradient y direction.

Theoretically, only the center of the selected labeling disk keeps the same phase as the RF pulse, other positions have less tagging efficiency depending on the distance to the center. It means that the tagging efficiency of single-artery PCASL is always less than non-selective PCASL. Therefore, to obtain enough SNR, SSFP is chosen for image acquisition. The experiment was conducted in 1.5 T scanner for fewer artifacts from off-resonance. The experiment consisted of three single-artery PCASL scans with each tagging only one artery which are right internal carotid artery (green), left internal carotid artery (red), and basilar artery (blue). After standard reconstruction, the images from each scan were given a certain color and combined together for visualization.

MIP images of axial, coronal, and sagittal plane are shown in Figure 2.8. We can see that, blood supply from different arteries is separated very well. Signal from basilar artery is relatively lower compared to the other two arteries probably due to the smaller diameter and slower flow of the basilar artery.

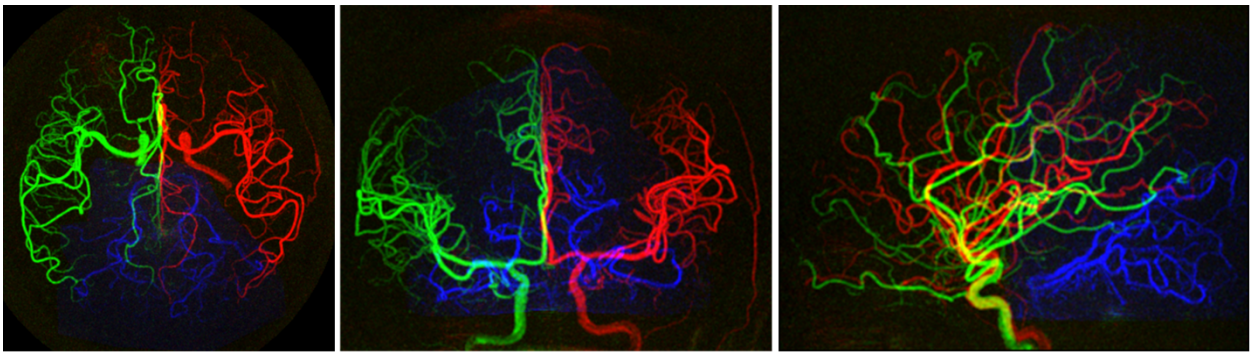

Figure 2.8: Combined color display of axial, coronal, and sagittal MIP images of a volunteer vessel-selective PCASL study. Red (tagged at left carotid artery); Green (tagged at right carotid artery); blue (tagged at basilar artery).

2.5 Labeling efficiency and tagging plane

Adiabatic inversion occurs when spins experience an RF magnetic field B1 of sweeping frequency relative to their resonance frequency. In the case of flow-driven inversions (e.g. CASL), the frequency sweep is achieved by the spins moving in the direction of a magnetic field gradient. In other words, the frequency of the B1 field is constant, but the resonant frequency of the spins changes as they move in the direction of the gradient. Pseudo-continuous inversion pulses produce the flow-driven adiabatic inversion effect in a piecewise manner by exciting the magnetization vector and allowing a small amount of position dependent phase accumulation in the transverse plane between RF pulses. Assuming that the slice-selective gradient is applied along the Z direction, the phase accumulation is caused by the imbalance in the slice-selective gradient (Gz) providing a net average gradient (Gave) between pulses. The net movement of the magnetization vector closely resembles the motion of continuous adiabatic inversions. Let us consider a single cycle in a pseudo-continuous inversion pulse, as depicted in Figure 2.1. Ideally, for a flowing spin moving at velocity V along the Z direction, which is at distance Z(t) from the iso-center, the amount of phase accumulation between the nth and (n+1)th RF pulses is:

$$\Delta\phi(n) = \int_{t=n\delta}^{(n+1)\delta} \gamma G_z(t) Z(t) dt \approx \gamma G_{zave} Z(0) \delta \tag{2.2}$$

where $G_z(t)$ represents the slice-selective gradient, δ is the time interval between two RF puluses, and G_{zave} is the average gradient over the time between RF pulses.

This term depends on the position of the tagging plane with respect to the system iso-center and needs to be compensated if the tagging plane is not located at the system iso-center. Adding a linear phase to the tagging/control RF pulses can compensate for this phase accumulation. However, the field homogeneity in the tagging plane is often perturbed by the presence of the head and/or by imperfect shimming. In particular, the air-tissue

interfaces in the mouth and throat and any dental work have a profound effect. We model the local field inhomogeneities at the tagging plane of the pCASL pulse as a constant shift plus a linear Z gradient, and refer to them as the 'off-resonance' (ΔB_0) and 'off-resonance gradient' (ΔG), respectively. In this case, the amount of error introduced into the phase accumulation ($\Delta\phi_{error}$) between two RF pulses can be calculated using:

$$\Delta\phi_{error} = \gamma\Delta B_0\delta + \frac{1}{2}\gamma V\Delta G\delta^2 \tag{2.3}$$

ΔG induces an unwanted velocity-dependent phase in the magnetization vector during the interval between RF pulses that can degrade the adiabatic inversion. Off-resonance ΔB_0 produces a position-dependent phase error in the magnetization vector that can further degrade the inversion. As a result, the inversion efficiency can be significantly modulated by the phase mismatch from gradient imperfections and the off-resonance fields. Therefore, the tagging efficiency of PCASL can vary greatly for different subjects, and also for different tagging locations in the same subject.

There has been research work about correcting the signal loss from phase matching errors. Jung [21] introduce a MP-PCASL approach which, instead of just acquiring the data at two phase offsets, as in the conventional PCASL approach, acquires at multiple phase offsets and then fit the data on a per-voxel basis to an expected inversion response curve. Jahanian [] proposed to restore the loss in tagging efficiency by correcting the phase of the RF pulses in combination with an average gradient compensation scheme.

Any loss in the tagging efficiency of PCASL causes a loss in SNR which cannot be neglected, given the inherently low SNR of ASL. In this work, we investigated the effects of tagging position to tagging efficiency and empirically determined the optimal anatomic location to achieve the best labeling efficiency.

One healthy volunteer was recruited for this study. 6 Static PCASL scans were conducted

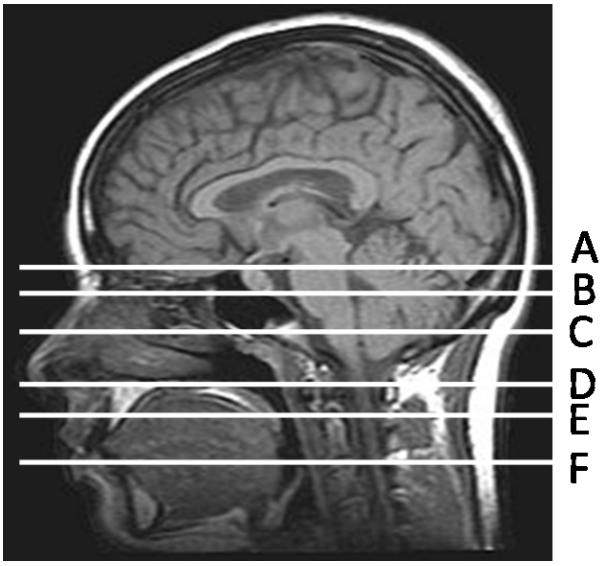

Figure 2.9: Labeling plane setups for tagging efficiency investigation.

with tagging planes setting at successively increasing distance from the top of the head as shown in Figure 2.9. 3000 projections were collected for each scan and 3D volume images were reconstructed with standard methods. Whole volume coronal MIP images were generated for each scan and presented in Figure 2.10. With a shorter transit distance from the tagging plane, signal loss from T1 recovery is supposed to be less. However, as shown in the MIPs (A), (B), (C), the distal vessels are not well visualized as in MIP (D) which has a more inferior tagging plane. This could be due to the phase matching errors such as local field inhomogeneities at the tagging plane or the vessel orientation. MIP (E) and (F) show a lower SNR of distal vessels which was could be due to the lower tagging efficiency and T1 recovery.

This study provided an optimization position D for tagging plane set up. A position other than that could suffer extra signal loss either from the low tagging efficiency, the vessel orientation or the T1 recovery. One example we encountered in patients study is a patient with an aneurysm located by the carotid (the case was also shown in Figure 2.7). In that scan, we set up the tagging plane at an unusually lower position and observed poor visualization of the most distal vessels as shown in Figure 2.11.

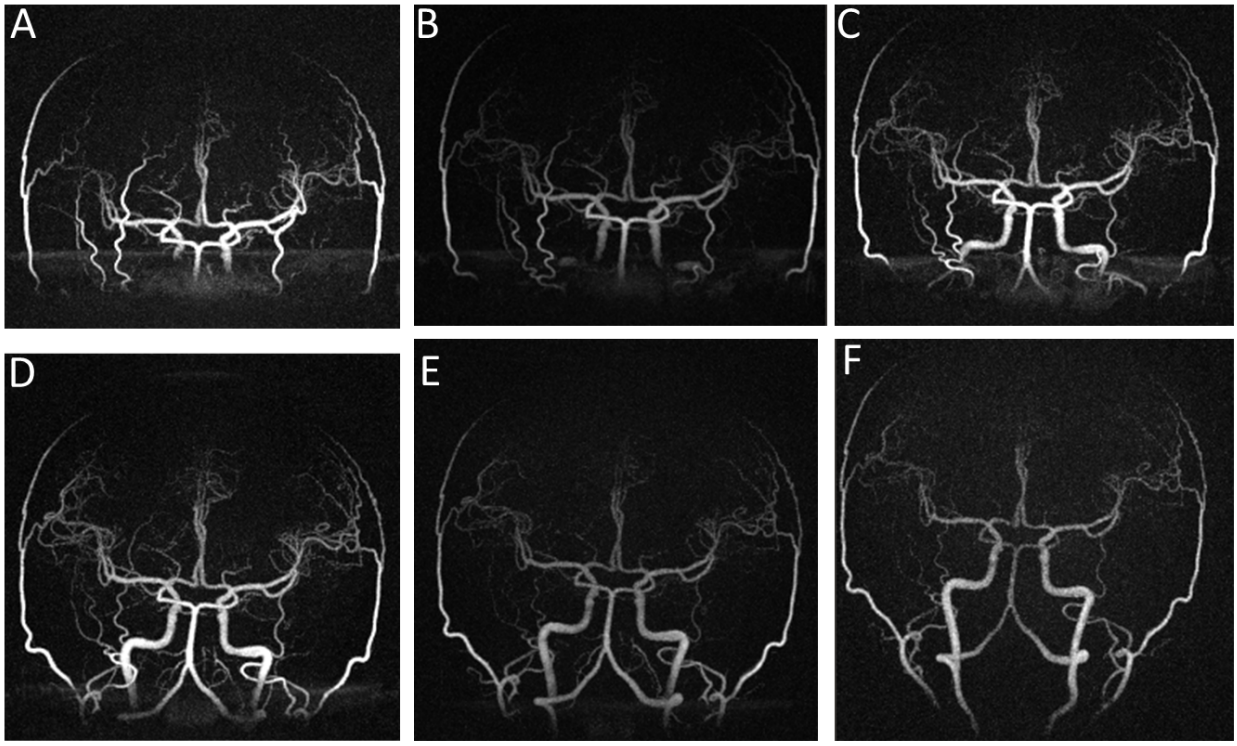

Figure 2.10: Coronal MIP images of varying tagging planes.

2.6 Discussion

We have developed a 3D non-contrast-enhanced MR angiography technique that combines ASL tagging with PCASL and an accelerated 3D radial acquisition technique, VIPR. PCASL-VIPR has been tested for intracranial angiography in both healthy and diseased subjects.

Compared with 3D TOF, PCASL-VIPR was found to hold several advantages over it as demonstrated by the images of the feasibility study. Ignoring the imperfect equalization of MT effects and the tissue perfusion signal, static tissue should be completely cancelled out by subtraction procedure. With a near zero background, vessel visualization is limited by noise in the background rather than contrast with neighboring structures. PCASL has much less sensitivity to slow flow while 3D TOF suffers from saturation artifacts due to slow or in-plane flow patterns. When combined with a 3D radial trajectory, PCASL-VIPR can easily

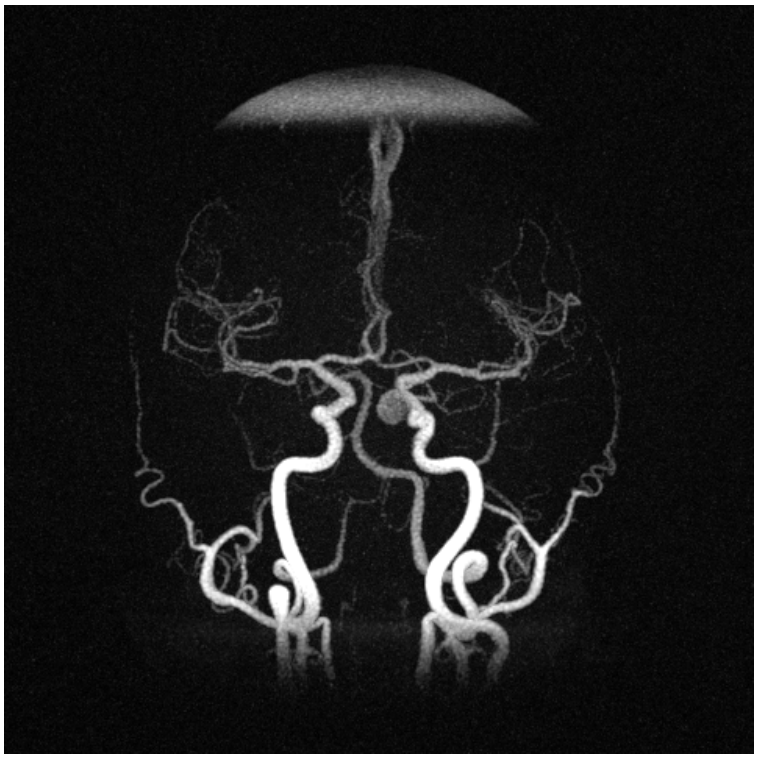

Figure 2.11: Whole volume coronal MIP image of an aneurysm patient scan. The tagging plane was set up very low in SI direction. Signal loss could be observed in distal vessels which have long transit time due to the unnecessarily low tagging plane.

cover the entire head without the extension of scan time and achieve 3D isotropic spatial resolution simultaneously. According to our evaluation results, whole head PCASL-VIPR provides approximately equal image quality as 3D TOF in healthy subjects. When applied to patients especially, AVM patients, PCASL-VIPR provides better image quality and diagnostic information over 3D TOF which suffers from the artifacts due to saturation and multi-slab coverage. The recent large group study that investigated the reliability of using 3D TOF to follow up the obliteration process of AVMs [22] showed its insufficiency when the remaining nidus diameter is < 10 mm. The reasons include spin dephasing due to complex or turbulent flow, saturation due to slow flow, and lack of temporal resolution. Our preliminary study has already shown PCASL's advantage of less sensitivity of slow flow. We also expect better performance of PCASL-VIPR in the delineation of AVMs when it's applied to dynamic

angiography. In future study, systematic analysis of the AVM components with large number of subjects will be conducted.

PCASL-VIPR holds several advantages over previously developed 3D PASL angiography techniques [11, 23, 24]. With PASL, the delay time between spin labeling and image acquisition needs to be chosen for the tradeoff between ensuring vasculature filling and providing adequate SNR. This parameter is subject dependent, and the selection requires additional scans and also induces other artifact-issues, even with the retrospective methods. For this work, we were able to utilize a long label duration (3 s) which ensured adequate vessel filling. Longer label duration could be utilized, but have diminished gains due to T1 recovery of the tag. Second, the vessel segments with different transit times experience different amount of T1 recovery in PCASL angiography varying from minimum (the proximal vessels) to maximum (the most distal vessels). In PASL angiography, all the vessel segments experience the same amount of T1 recovery which is determined by the longest transit time. Therefore, PCASL angiography provides higher SNR than PASL angiography.

Previously reported PCASL angiography [3, 4] are limited to 2D projection imaging or multiple thick-slab imaging, and cannot be easily extended to 3D imaging due to long scan times. With the accelerating benefits from the 3D radial trajectories, PCASL-VIPR is the first method to achieve high 3D isotropic spatial resolution which greatly improves the vessel visualization compared to the 2D techniques.

The use of balanced SSFP as seen in other non CE-MRA methods could provide higher SNR and reduced RF saturation effects. However, SSFP is generally more prone to off-resonance artifacts that are more prevalent when imaging at higher field strength. In this work, the choice of SPGR avoided this issue and also reduced the specific absorption rate compared to balanced SSFP.

Vessel selective ability of PCASL has been explored and validated with a volunteer study. Due to the loss of tagging efficiency, so far vessel selective PCASL-VIPR can only be

performed in 1.5 T scanner with SSFP readout for sufficient SNR. Since the tagging accuracy relies on the accuracy of target artery location, long scan time due to multiple acquisitions makes the current technique sensitive to patient motion. Optimized protocol with integrated acquisition, easy location measuring, and short scan time needs further work. The usefulness of the technique to certain vascular diseases needs further exploration.

The efficacy of PCASL-VIPR is primarily limited by long scan times, T1 recovery, RF-saturation, and labeling efficiency. Long scan times introduce sensitivity to motion artifacts and hinder time resolved imaging or vessel selective imaging. In this work, we have not utilized parallel imaging or compressed sensing [25] which could be utilized to help achieving higher acceleration factors. The signal difference of PCASL-VIPR is directly related to the labeling efficiency of PCASL. Efficiency can be lost by imperfect phase tracking at the labeling plane. Phase tracking errors arise from off-resonance field at the labeling plane due to imperfect shimming or the susceptibility from eddy currents or gradient waveform errors. Corrections can be made if the amount of off resonance and gradient errors can be mapped at the labeling plane [21, 26], but requires substantially more imaging time. Higher order shimming might also be useful and will be tested in future study.

Although signal saturation is substantially reduced compared to 3D TOF, signal loss is still observed in distal vessels in PCASL-VIPR. Because of T1 recovery, signal decreases exponentially with the transit time from labeling plane. This limits the extent to which slow inflow can be imaged. In addition, signal saturation occurs in distal vessels due to the application of multiple RF pulses within an SPGR readout cycle. Spin that are not refreshed during the readout by inflow experience more RF saturation. This effect is more severe when the readout flip angle increases and/or the acquisition window extends. The residual tissue signal at the inferior edge of the image volume as can be seen from the coronal and sagittal MIP images came from two sources: the selective inversion performed over the imaging volume and PCASL labeling at the edge of the volume. With PCASL, the tissue

spins at the labeling plane experience (α, α) RF pulses in the label phase, and (α, -α) RF pulses in the control phase. Therefore, the saturation effects caused by the two different RF pulse train are not equal. Furthermore, the selective inversion has a profile that will result in incomplete subtraction at areas just outside the imaging FOV. Subtraction of the label phase and control phase is not able to cancel out the tissue signal at the labeling plane and leaves some residual tissue signal at the inferior edges of the 3D image volume. Both of these errors would be mitigated by placing the labeling plane more inferior, at the cost of reduced flow sensitivity.

2.7 References

[1] L Axel. Blood flow effects in magnetic resonance imaging. *Magn Reson Annual*, pages 237–44, 1986.

[2] I Koktzoglou, N Gupta, and RR Edelman. Nonenhanced extracranial carotid mr angiography using arterial spin labeling: improved performance with pseudocontinuous tagging. *J Magn Reson Imaging*, 34(2):384–394, 2011.

[3] PM Robson, W Dai, A Shankaranarayannan, NM Rofsky, and DC Alsop. Time-resolved vessel-selective digital subtraction mr angiography of the cerebral vasculature with arterial spin labeling. *Radiology*, 257(2):507–515, 2010.

[4] TW Okell, MA Chappell, and MW Woolrich. Vessel-encoded dynamic magnetic resonance angiography using arterial spin labeling. *Magn Reson Med*, 64(3):698–706, 2010.

[5] Huimin Wu, Walter F. Block, Patrick A. Turski, Charles A. Mistretta, and Kevin M. Johnson. Noncontrast-enhanced three-dimensional (3d) intracranial mr angiography using pseudocontinuous arterial spin labeling and accelerated 3d radial acquisition. *Magnetic Resonance in Medicine*, pages n/a–n/a, 2012.

[6] Brian A. Hargreaves, Charles H. Cunningham, Dwight G. Nishimura, and Steven M. Conolly. Variable-rate selective excitation for rapid mri sequences. *Magnetic Resonance in Medicine*, 52(3):590–597, 2004.

[7] EC Wong. Vessel-encoded arterial spin-labeling using pseudocontinuous tagging. *Magn Reson Med*, 58(6):1086–1091, 2007.

[8] S. G. Kim. Quantification of relative cerebral blood flow change by flow-sensitive alternating inversion recovery (fair) technique: application to functional mapping. *Magn Reson Med*, 34(3):293–301, 1995.

[9] O. Bieri, M. Markl, and K. Scheffler. Analysis and compensation of eddy currents in balanced ssfp. *Magn Reson Med*, 54:129–137, 2005.

[10] D. C. Peters, F. R. Korosec, T. M. Grist, W. F. Block, J. E. Holden, K. K. Vigen, and C. A. Mistretta. Undersampled projection reconstruction applied to mr angiography. *Magnetic Resonance in Medicine*, 43(1):91–101, 2000.

[11] ET Tan, J III Huston, NG Campeau, and SJ Riederer. Fast inversion recovery magnetic resonance angiography of the intracranial arteries. *Magn Reson Med*, 63:1648–1658, 2010.

[12] B.H. Holmes, R.L. O'Halloran, E.K. Brodsky, Y. Jung, W.F. Block, and S.B. Fain. 3d hyperpolarized he-3 mri of ventilation using a multi-echo projection acquisition. *Magn Reson Med*, 59:1062–1071, 2008.

[13] M.I. Altbach, E.K. Outwater, T.P. Trouard, E.A. Krupinski, R.J. Theilmann, A.T. Stopeck, M. Kono, and A.F. Gmitro. Radial fast spin-echo method for t2-weighted imaging and t2 mapping of the liver. *J Magn Reson Imaging*, 16:179–189, 2002.

[14] R.J. Theilmann, A.F. Gmitro, M.I. Altbach, and T.P. Trouard. View-ordering in radial fast spin-echo imaging. *Magn Reson Med*, 51:768–774, 2004.

[15] P.J. Beatty, D.G. Nishimura, and J.M. Pauly. Rapid gridding reconstruction with a minimal oversampling ratio. *IEEE Trans Med Imaging*, 24(6):799–808, 2005.

[16] C. A. McKenzie, E. N. Yeh, M. A. Ohliger, M. D. Price, and D. K. Sodickson. Self-calibrating parallel imaging with automatic coil sensitivity extraction. *Magn Reson Med*, 47(3):529–38, 2002.

[17] Mark A. Griswold, Peter M. Jakob, Mathias Nittka, James W. Goldfarb, and Axel Haase. Partially parallel imaging with localized sensitivities (pils). *Magnetic Resonance in Medicine*, 44(4):602–609, 2000.

[18] P. B. Roemer, W. A. Edelstein, C. E. Hayes, S. P. Souza, and O. M. Mueller. The nmr phased array. *Magn Reson Med*, 16(2):192–225, 1990.

[19] R. Werner, D.G. Norris, K Alfke, H.M. Mehdorn, and O. Jansen. Continuous artery-selective spin labeling (cassl). *Magn Reson Med*, 53:1006–1012, 2005.

[20] W Dai, P.M. Robson, A Shankaranarayannan, and D.C. Alsop. Modified pulsed continuous arterial spin labeling for labeling of a single artery. *Magn Reson Med*, 64:975–982, 2010.

[21] Youngkyoo Jung, Eric C Wong, and TT Liu. Multiphase pseudocontinuous arterial spin labeling (mp-pcasl) for robust quantification of cerebral blood flow. *Magn Reson Med*, 64(3):799–810, 2010.

[22] D.R. Buis, J.C. Bot, F. Barkhof, D.L. Knol, F.J. Lagerwaard, B.J. Slotman, W.P. Vandertop, and R van den Berg. The predictive value of 3d time-of-flight mr angiography in assessment of brain arteriovenous malformation obliteration after radiosurgery. *AJNR Am J Neuroradiol*, 33:232–238, 2012.

[23] L Yan, S Wang, Y Zhuo, RL Wolf, MF Stiefel, J An, Y Ye, Q Zhang, ER Melhem, and DJJ Wang. Unenhanced dynamic mr angiography: High spatial and temporal resolution by using true fisp - based spin tagging with alternating radiofrequency. *Radiology*, 256(1):270–279, 2010.

[24] X Bi, P Weale, P Schmitt, S Zuehlsdorff, and R Jerecic. Non-contrast-enhanced four-dimensional (4d) intracranial mr angiography: A feasibility study. *Magn Reson Med*, 63:835–841, 2010.

[25] M Lustig, D Donoho, and JM Pauly. Sparse mri: The application of compressed sensing for rapid mr imaging. *Magn Reson Med*, 58:1182–1195, 2007.

[26] H Jahanian, DC Noll, and L Hernandez-Garcia. B(0) field inhomogeneity considerations in pseudo-continuous arterial spin labeling (pcasl): effects on tagging efficiency and correction strategy. *NMR Biomed*, in press, 2011.

3 Dynamic angiography with PCASL-VIPR

The status of flow through AVMs is believed to be one of the risk factors in predicting their propensity to hemorrhage [1, 2]. Change of flow is also of clinical significance after endovascular or radiation therapy to evaluate the effect of treatment. 3D time-of-flight (TOF), the most widely utilized, provides good depiction of the anatomic features of AVMs; however, does not allow assessment of AVM filling and draining and often poorly delineates nidus size [3].

Dynamic Contrast enhanced (DCE) MRA with Gadolinium based contrast agents provides both spatial and temporal filling dynamics, but is often insufficient for intracranial applications. High flow brain lesions often lead to rapid arterial venous shunt transit times (<0.5s). Therefore, extremely high temporal resolution is required to adequately visualize filling dynamic. With recent advances including temporal view sharing [4, 5], parallel imaging, undersampled acquisitions [5, 6, 7], and novel reconstruction strategies (e.g. compressed sensing [8], HYPR [9, 10], etc), DCE-MRA temporal resolution has improved. However, substantial spatial resolution and coverage still must be sacrificed to achieve sufficient temporal resolution. Moreover, DCE-MRI relies on an intravenously delivered bolus of Gd. This leads to considerable bolus dispersion which limits the effective temporal resolution [11] in addition to posing risk of nephrogenic systemic fibrosis in patients with impaired renal function [12].

Non-contrast-enhanced, arterial spin labeling (ASL) MRA techniques hold the potential to provide intracranial hemodynamics with high spatial and temporal resolution and limited bolus dispersion. With pulsed ASL, dynamics can be obtained by acquiring images with multiple delays after the inversion [13]. With low flip angle bSSFP, multiple phases can be acquired after the inversion to efficiently observe filling [14, 15, 16]. Recent application in 4D intracranial MR angiography [15, 17] has shown promising results with temporal resolution as high as 50 ms. Unfortunately, the signal-to-noise (SNR) in PASL is sensitive to RF transmission uniformity which limits the use of PASL with long labeling delays. Furthermore, image quality is often compromised when utilizing bSSFP readouts which with low flips angles is particularly prone to artifacts from off-resonance and flow [18, 19, 20]. This is amplified when spins move across bSSFP off-resonance bands, effectively interrupting steady state conditions.

PCASL has shown its potential in imaging the dynamic filling in intracranial vasculature [21, 22]. Unfortunately, current studies are limited to 2D dynamic projection imaging due to scan time limitations. In this work, we developed a dynamic angiography technique that based on previously proposed sequence PCASL-VIPR [23]. This technique can simultaneously achieve high temporal resolution (200 ms), high 3D isotropic spatial resolution (0.68 mm^3), and whole-head coverage within clinically acceptable scan time. Furthermore, this 3D radial technique enables accurate quantification of temporal arrival times (TOA). This mirrors developments of DSA [24], PASL MRA [25] and CE MRA [26] where arrival time can be computed from a series of images. To evaluate this technique, digital simulations were performed and feasibility studies were conducted in patients with known AVMs or dural arteriovenous fistulas (AVFs).

3.1 Sequence design

Since the invention of PCASL, there have been two schemes of using PCASL to acquire temporal information. In the first scheme [27], as shown in Figure 3.1, a series of time frames were acquired after either a short tagging duration or a long tagging duration. With short tag duration, the filling of the bolus can be observed in the first few time frames. However, in the later time frames when the inverted spins arrive at the distal vessels, the inverted spins have already experienced substantial decay from both repetitive RF pulses and T1 recovery. Therefore, the distal vessels are barely visualized due to lack of SNR. When a long tagging duration is utilized, flow information can be obtained by observing the wash-out of the bolus from vascular tree. However, in the last few frames when the residual signal in the vasculature is supposed to appear in the distal vessels, the visualization of these signals are not of sufficient quality due to the same reason of decay.

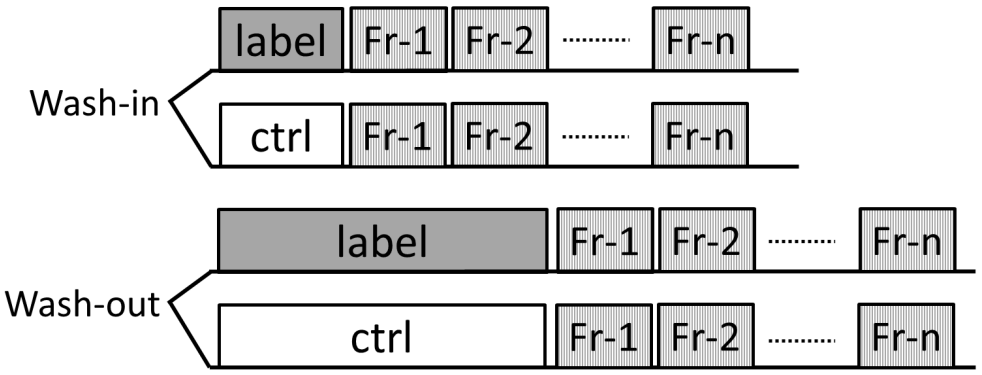

Figure 3.1: Diagram of dynamic PCASL angiography with scheme 1: wash-in dynamic is acquired with a short tag duration followed by a series of data acquisitions; wash-out dynamics is acquired with a long tag duration followed by a series of data acquisitions.

In the second scheme [21], as shown in Figure 3.2, images of dynamic flow are obtained by successive acquisition with varying tagging duration. By using arterial water as an endogenous tracer, ASL is not restricted to a single pass, and temporal resolution is not constrained by

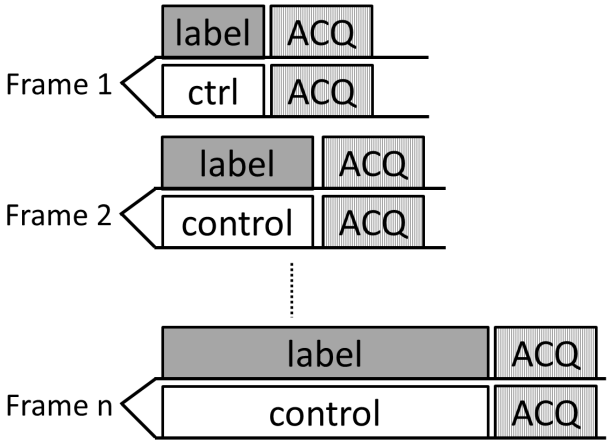

Figure 3.2: Diagram of dynamic PCASL angiography with scheme 2: each frame acquires a tag image and a control image with a certain tag duration.

intravenous bolus dynamics, but controlled by the tagging duration set by the operator.

Dynamic PCASL-VIPR is based on the previously reported static PCASL-VIPR technique [23, 21] and consists of interleaved tagging sessions as shown in Figure 3.3. Each tagging session consists of four modules: background suppression, PCASL pulse train, PASL, and image acquisition. Background suppression consists of a selective 180 $^\circ$ inversion. This is followed by PCASL module which is composed of two parts: control state and label state (Figure 3.3). The overall length of PCASL module is identical for all the tagging session while the duration of label state part is altered for different time frame acquisitions. By this means, background signal and magnetization transfer effects are consistent amongst time frames and a single control acquisition can be utilized for background subtraction.

During the control state, the RF phase is cycled between excitations such that spins at the labeling plane observe RF pulses with π phase difference relative to the previous pulse, leading to limited effect on the passing spins. For the label state, this phase difference is set to zero such that spins passing through the labeling plane undergo adiabatic inversion.

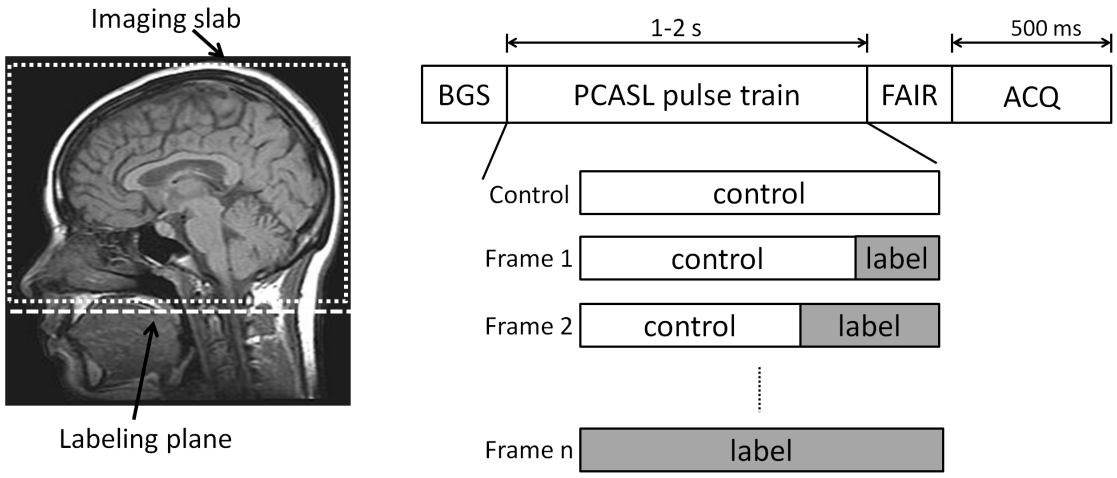

Figure 3.3: Labeling geometry (left, dashed box indicates imaging slab, dashed line indicates the labeling plane); dynamic PCASL-VIPR sequence diagram (right) shows a tagging session consisting of four modules: background suppression, PCASL, FAIR, and acquisition with time assignment. In each tagging session, PCASL pulse train is set up differently (relative length of label state) according to the required acquisition (control, Frame 1-n).

3.2 Time of Arrival (TOA) mapping

After acquisition and reconstruction, a time series of 3D images will be obtained. This large volume can be challenging to interrogate and provides no quantitative information. Time of arrival (TOA) mapping provides a method to compress the 4D filling pattern into a quantitative 3D image, which may be easier to interrogate than the full 3D volume. This can be performed by simple thresholding of the signal time course; however it ignores substantial effects from RF saturation by the imaging module, T1 relaxation, and provides coarse temporal resolution. Instead, we model the expected signal time course utilizing Bloch equations and fit the observed ones to the model. This allows substantially higher resolution in the TOA map than the acquired temporal resolution.

To model the inflowing spins, we assume a single arrival time at each spatial location. A set of expected signal time courses for the measurable range of TOA is first established as shown in Figure 3.4. For this sequence, the range is from zero to the longest tag duration plus

the sampling window length. For each PCASL pulse train, the evolution of the longitudinal and transverse magnetization of the moving spins during the passage through labeling, T1 recovery, and RF saturation is simulated with Bloch equations without diffusion. Parameters used in the scan are applied to the algorithm and the T1 of blood is assumed to be 1664 ms. This simulation gives the expected signal behavior at each TR in the sampling window, not the signal for each image. Estimating the signal for each time frame image is different depending on the acquisition scheme. For Cartesian acquisitions, center of k-space is sampled once and subsequently the signal behavior in the image is expected to follow the time point at which the center of k-space is sampled. For radial acquisitions, center k-space is sampled at every TR and subsequently the signal behavior is expected to follow the average signal over the entire acquisition window.

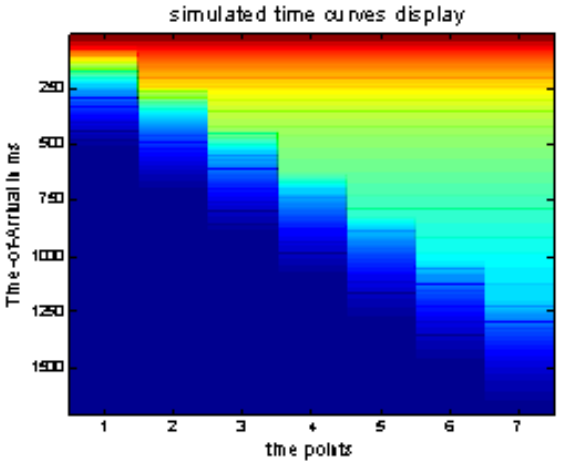

Figure 3.4: Simulated time curves of a TOA range of [0 1.75 s]

With a set of expected signal time courses for each characteristic TOA, a simple search is performed for every voxel of the 3D time frames with sum of squared differences utilized as a goodness of fit. Hue, saturation, and brightness scheme is used for colorization: the TOA map is used to determine the hue; the magnitude of the 3D image volume with the longest labeling duration is to determine the saturation and brightness.

3.3 Digital simulation and results

To investigate the effects of scan protocol on the fidelity of the TOA mapping method and overall image quality, experiments were conducted in two 2D digital phantoms. The first phantom was a highly simplified straight vessel with reconstructed resolution of 256 x 256 and without background tissue and plug flow as seen in Figure 3.5. The true TOA value of the pixels inside the vessel linearly increased from left end to right end of the vessel from 1 to 200 TRs. The second phantom was designed using a non-overlapping fractal tree, mimicking the cerebral arterial vascular system. A single input vessel bifurcated 8 times resulting 8 different sizes of vessels. The reconstructed spatial resolution of this phantom was 512 x 512. True TOA values increased from the input vessel to the distal vessels from 1 to 235 TRs as seen in Figure 3.6.

We first performed experiments on both phantoms to interrogate the effects of acquisition scheme on the image artifacts and the fidelity of TOA mapping method. Parameters for sequence set up were as follows: number of tagging sessions in one cycle = 8 (7 labels and 1 control); time spacing = 200 ms; length of sampling window = 500 ms (98 TRs). To simulate acquisitions of each PCASL pulse train set up, truth images at each TR in the sampling window were generated with given input TOA image following these procedures: For each tagging session, a set of expected signal curves for the measurable range of TOA is established by simulating the evolution of the longitudinal and transverse magnetization of the moving spins with Bloch equations (same as described in TOA mapping method); Then, for each pixel in the digital phantom, its signal at each TR during the sampling window is selected from the expected signal curves. Subsequently, K-space data is simulated utilizing inverse discrete Fourier transform.

For Cartesian acquisition, one readout (a horizontal line in 2D K-space) with 256/512 (512 in fractal tree phantom) sample points was generated from a truth image at each TR. A

total of 256/512 readouts (to satisfy Nyquist sampling criterion) were collected in a sequential order with 98 in each tagging session. For Radial acquisition, one readout (a full projection intersecting the center of k-Space) of 256/512 (512 in fractal tree phantom) sample points was generated from a truth image at each TR. A total of 400/800 (to satisfy Nyquist sampling criterion) projections were collected in a bit-reverse sampling order with 98 in each tagging session. Seven time frame images were then reconstructed from the simulated k-space data of both acquisition schemes followed by TOA mapping. Time frame images of both acquisition schemes were presented to compare the artifacts originated from the inconsistent contrast during sampling. For TOA mapping fidelity, on the single vessel phantom, the acquired TOA profiles along the horizontal center line of the vessel were compared with truth. On the fractal tree phantom, difference TOA maps were presented on the same display window to compare the two acquisition schemes. On both phantoms, root-mean-square error (RMSE) of the TOA map was calculated.

Simulation results on comparison between radial and Cartesian acquisition schemes are shown in Figure 3.5 and 3.6 (Figure 3.5: vessel phantom, Figure 3.6: fractal tree phantom). For both phantoms, 4 time frame images (frame 1, 3, 5, 7) reconstructed from both acquisition schemes are presented to compare image quality. In Figure 3.5(A), images of Cartesian acquisition sharply depict the leading edge of the vessel but also show substantial artifacts. In the radial acquisition, the leading edge of the bolus is blurred; however, artifacts from inconsistency across the sampling window are diffuse. In Figure 3.6, because of increased complexity of the digital phantom (multiple vessels heading different directions), images of Cartesian acquisitions show substantial ghost-pattern artifacts. In the radial acquisition, only blurring at the leading edge of the bolus is observed.

The comparison between two acquisition schemes on TOA mapping is presented in the bottom row on both figures. In Figure 3.5(B), TOA profile of Cartesian acquisition shows a stepping pattern and the deviation from the truth is as large as the spacing between time

frames. In Figure 3.5(C), the TOA profile of radial acquisition shows greater agreement with the truth, with limited dependence on arrival time. In Figure 3.6(B-C), TOA difference images from both acquisitions are displayed with the same scale window and the one of Cartesian acquisition shows much greater error especially at vessel edges.

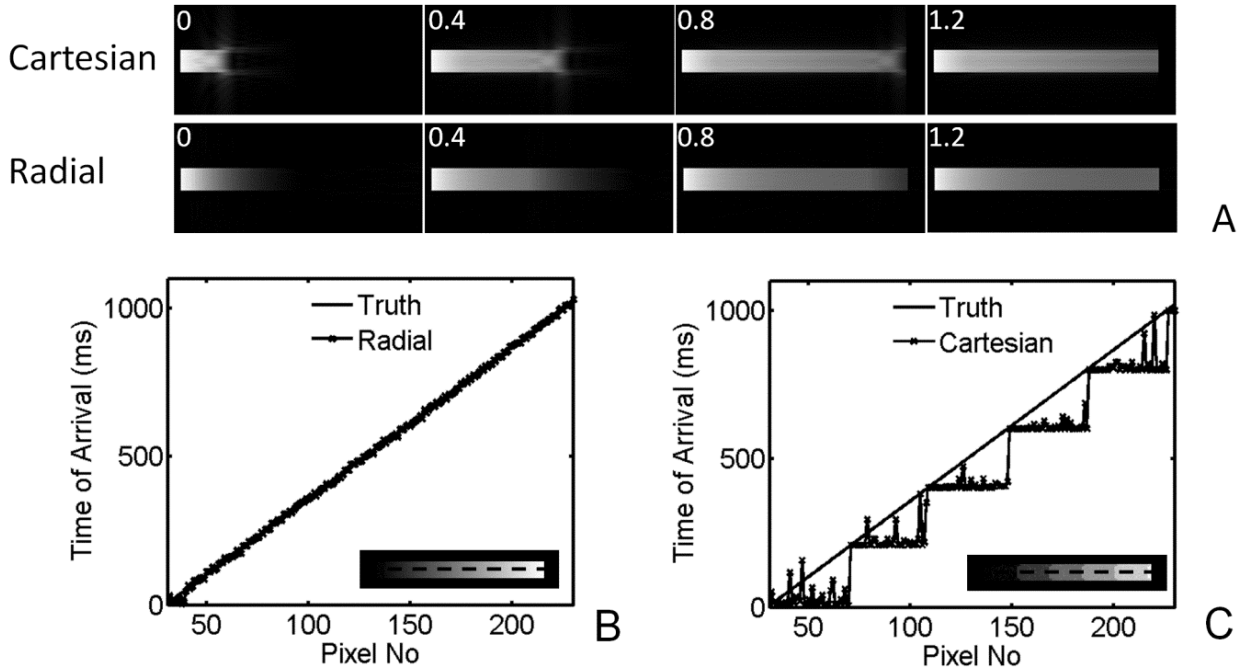

Figure 3.5: (A) Reconstructed time frame images at time points: 0, 0.4, 0.8, and 1.2 of single vessel phantom from Cartesian acquisition and radial acquisition. Notice the different artifact pattern and blurring effects. (B-C) Comparison of the TOA profiles along the horizontal center line of the vessel (black dashed line in the TOA image on bottom right of each picture). B: Radial acquisition vs. truth; C: Cartesian acquisition vs. truth.

In a subsequent experiment, we investigated the effects of two sequence parameters to the accuracy of TOA mapping: length of sampling window and time spacing. The experiment was conducted on the vessel phantom and only the radial acquisition scheme was utilized. Three values of the sampling window length were compared 200 ms, 500 ms, and 800 ms with a consistent time spacing of 200 ms. Then, three values of time spacing were compared 200 ms, 300 ms, and 600 ms with a consistent sampling window length of 600 ms. For each

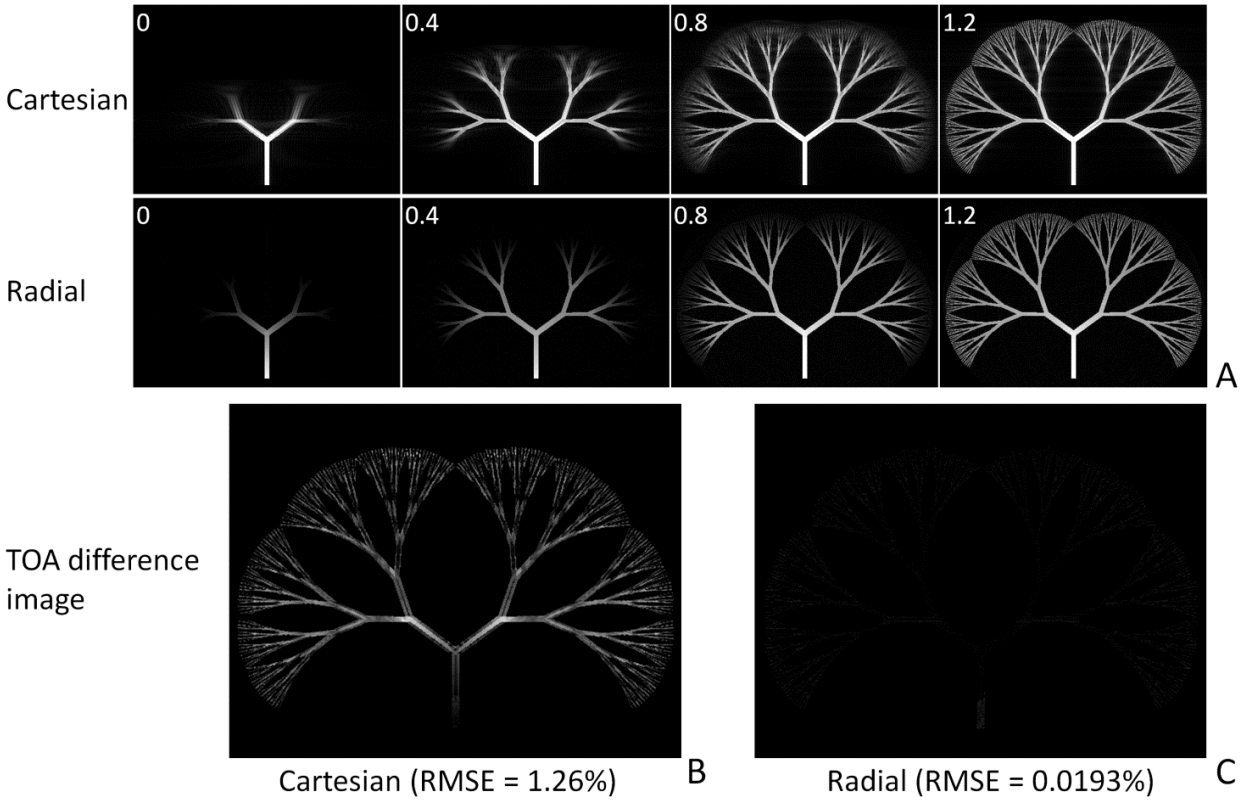

Figure 3.6: (A) Reconstructed time frame images at time points: 0, 0.4, 0.8, and 1.2 of fractal tree phantom from Cartesian acquisition and radial acquisition. Notice the different artifact pattern and blurring effects. (B). Comparison of TOA difference image generated from Cartesian acquisition (B) and Radial acquisition (C) (same display window). RMSE of TOA map is 65 times larger with Cartesian acquisition.

parameter set up, the generation of truth images and radial acquisition simulation were first performed with the same method described in the first experiment. Then a certain amount of independently complex noise were added on the originally simulated k-space data and 7 time frame images were reconstructed from this data set followed by TOA mapping. The above step (with noise adding, reconstruction and TOA mapping) was repeated for a series of SNR levels. RMSE value of TOA map at each SNR level was then calculated and an RMSE-SNR curve corresponding to this parameter set up was created.

TOA mapping dependence on sequence parameters is shown in Figure 3.7. The horizontal

axis presents the SNR level in logarithmic scale. The vertical axis shows the RMSE value of the TOA map. For all parameter set ups, the curve monotonically decreases as SNR increases. In Figure 3.7(A), substantial differences are seen with varying sample window lengths. Shorter sampling windows provide higher precision at the cost of proportionally longer scan times. In Figure 3.7(B), limited differences in precision are observed with varying time spacing between frames.

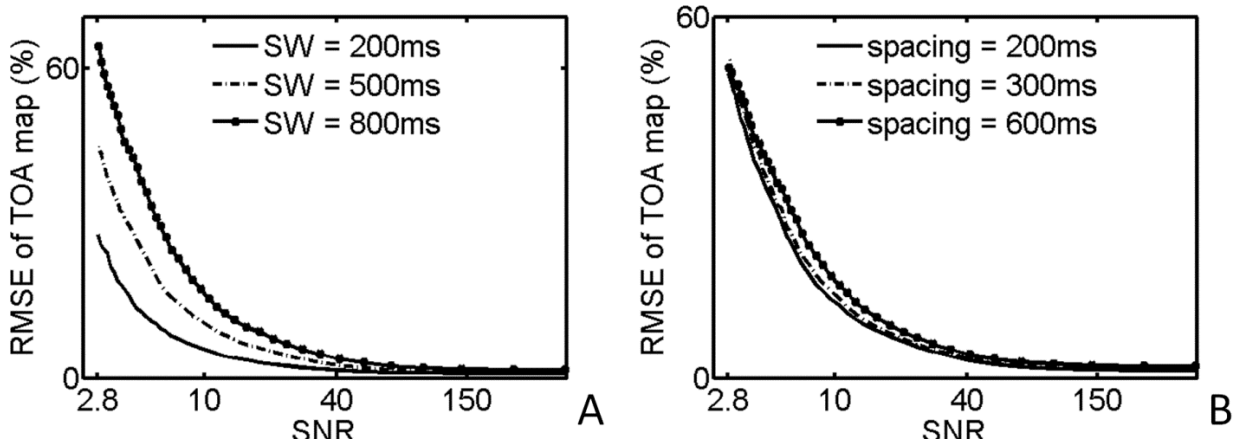

Figure 3.7: (A) RMSE-SNR curve with sampling window (SW) lengths: 200, 500, and 800 ms. (B) RMSE-SNR curve with time spacings: 200, 300, and 600 ms.

3.4 In-vivo study and results

To provide preliminary in-vivo evaluation of dynamic PCASL technique, 5 patients with known cerebral vascular disease were recruited: 3 of them have previously diagnosed AVMs with Spetzler-Martin grading scales of 5, 2, and 4 respectively; 2 have DAVFs with Cognard classification of Type I and Type II A+B. All the patients were imaged after obtaining Institutional Review Board (IRB) approval and informed consent. All exams were performed on a clinical 3T MR system (Discovery 750, GE Healthcare, Waukesha, WI, USA) with a 32-channel head coil (32 Ch Head, MR Instruments, Hopkins, MN, USA). Patients were

imaged with dynamic PCASL-VIPR sequence and a clinically standard 3D TOF. The 3D TOF scan was acquired with the following parameters: TR/TE (ms) 30/2.8; field of view 22 x 22 cm^2; matrix 512 x 256; slice thickness 1 mm; flip angle 20 $^\circ$; bandwidth 41.67 kHz; number of slabs 4; slab thickness 40 mm; overlap thickness 10 mm; parallel imaging method SENSE (ASSET; GE Healthcare) with an acceleration factor of 2x. For partial head coverage of 11 cm, the examination time was 8:01 min.

For dynamic PCASL-VIPR scan, the labeling plane was approximately placed at C1 segment of the internal carotid arteries such that the major feeding arteries of the brain vasculature including internal carotid arteries, external carotid arteries and vertebral arteries were labeled. A 16cm-thick imaging slab was prescribed right above the labeling plane with a FOV of 22×22×16 cm^3 covering the whole brain. The sampling window was set to 500 ms and 3,000 TRs/frame were collected. PCASL tagging duration and time spacing were adjusted to specific cases. For 4 of the 5 patients, 7 time frames with a time spacing of 200 ms were acquired with a scan time of 7:30 min. For the 5th patient, PCASL tagging duration was extended to 2 sec in order to visualize the venous drainage. 5 time frames with a time spacing of 500 ms were acquired with a scan time of 8:30 min. 3D images for every time frame of every subject were reconstructed with the aforementioned method, zero-filled to 0.46 mm isotropic resolution. TOA mapping was performed afterwards as well as the generation of colorized TOA images.

DSA images acquired within 8 weeks before our study are available for all the five subjects and no treatment was performed in between. All DSA exams were obtained at an Artis Zee biplane angiographic suite (Siemens, Erlangen, Germany). A minimum of two views (frontal and lateral) were obtained for each vascular pedicle at a frame rate of 2-4 images per second. In some instances oblique and 3D rotational volume images were also generated. The detector system provides 1024x1024 resolution. The field of view varied depending on the magnification and collimation of the x-ray beam. Images were obtained following injection of

3-6 mL of iohexol (Omnipaque 300, Nycomed Imaging AS, Oslo, Norway) at a rate between 5-6 mL/sec.

Figure 3.8 illustrates a time series of representative maximum intensity projection (MIP) images of dynamic PCASL-VIPR in the axial, coronal, and sagittal orientations acquired from a patient with large left frontal-parietal AVM. Bottom row shows the corresponding lateral projections from the DSA exam. As seen on the magnified axial MIPs (top row), small vessels are well visualized with a spatial resolution of 0.68 mm. On the sagittal MIPs (middle row), the branches of the left callosal marginal artery (arrows) can be clearly identified as the supply of the AVM. As seen on the coronal MIPs (second row), dynamic PCASL exam provides the temporal resolution necessary to delineate the relative filling rates of the AVM feeding arteries compared to the normal vessel. Colorized TOA image (bottom right) shows the flow dynamics from red (earliest filling) to purple (latest filling).

Figure 3.9 shows the results of a patient with a right parietal AVM. Coronal (top) and sagittal (middle) MIPs at three time points 0.4, 0.8 and 1.2 s are displayed. Bottom row shows the corresponding lateral projections from the DSA exam. The PCASL images provide excellent delineation of the right angular artery (arrows) and parietal branches (arrowheads) that supply a well-defined AVM nidus. The filling patterns of the arterial feeders and normal arteries show excellent agreement with the DSA exam. Colorized TOA image (middle right) also provides clear delineation of the feeding arteries and nidus and shows the filling pattern.

Figure3.10 shows the results of a patient with a large Brainstem AVM. Top row displays sagittal MIPs at time points 0.6 and 0.8 s. As seen on the images, the AVM is supplied by the basilar artery via small perforating vessels and superior cerebellar arteries (arrows). As compared to the sagittal MIP of 3D TOF (bottom right), the latter one shows higher spatial resolution however with more saturation artifacts. Colorized TOA image (bottom left) helps the visualization of filling pattern.

Figure 3.11 shows the results of a patient with a left posterior fossa DAVF. Axial (top

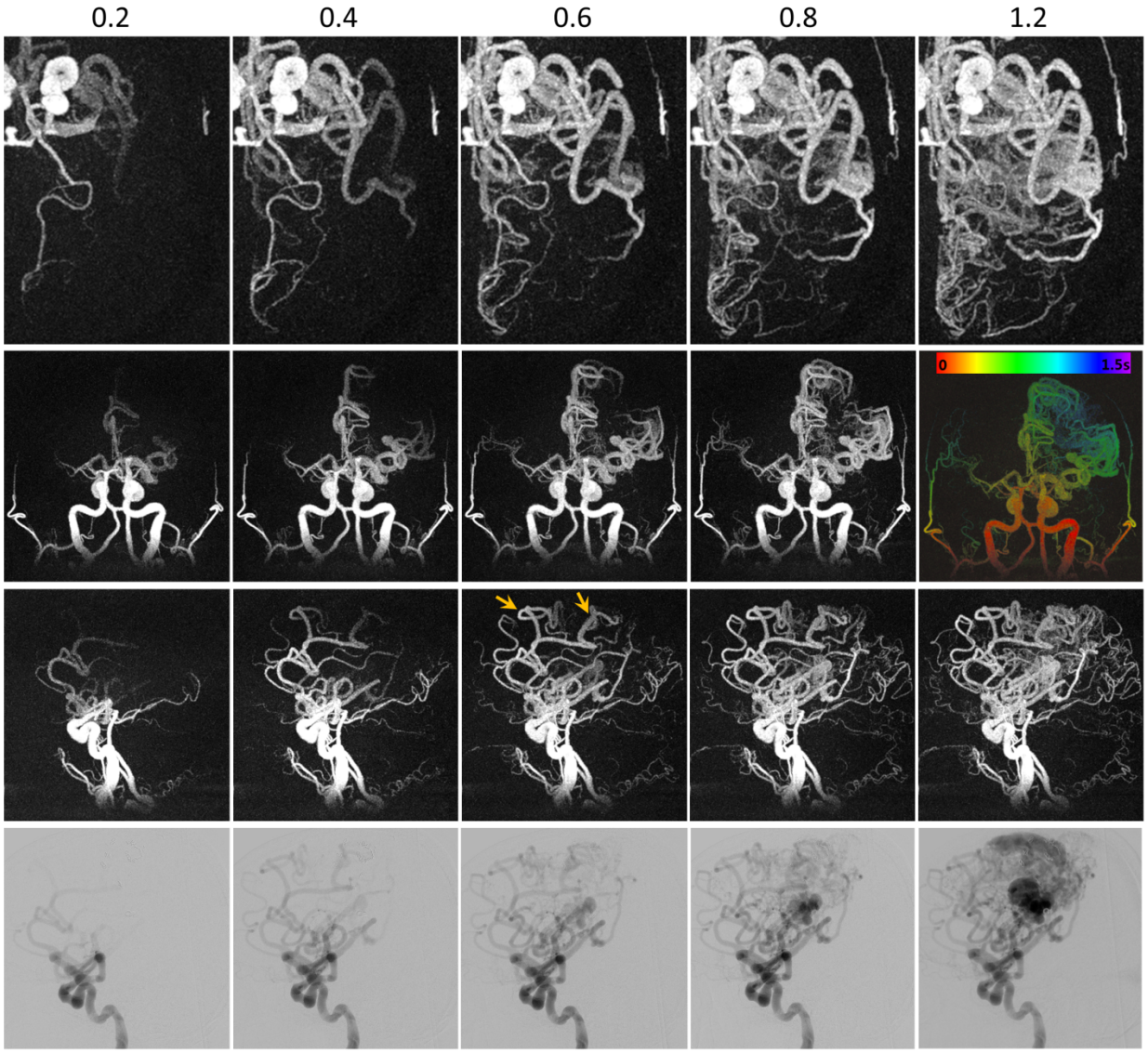

Figure 3.8: Large left frontal-parietal AVM. Rows 1-3 display the dynamic PCASL exam in the axial (magnified), sagittal and coronal planes with a temporal spacing of 200 ms. TOA map is displayed in color on bottom right with time-color bar. Arrows in the sagittal MIP at 0.6 s point to the branches of the left callosal marginal artery (arrows) that supply the AVM. The relative filling rates of the AVM feeding arteries compared to the normal vessels can be easily delineated from colorized TOA image.

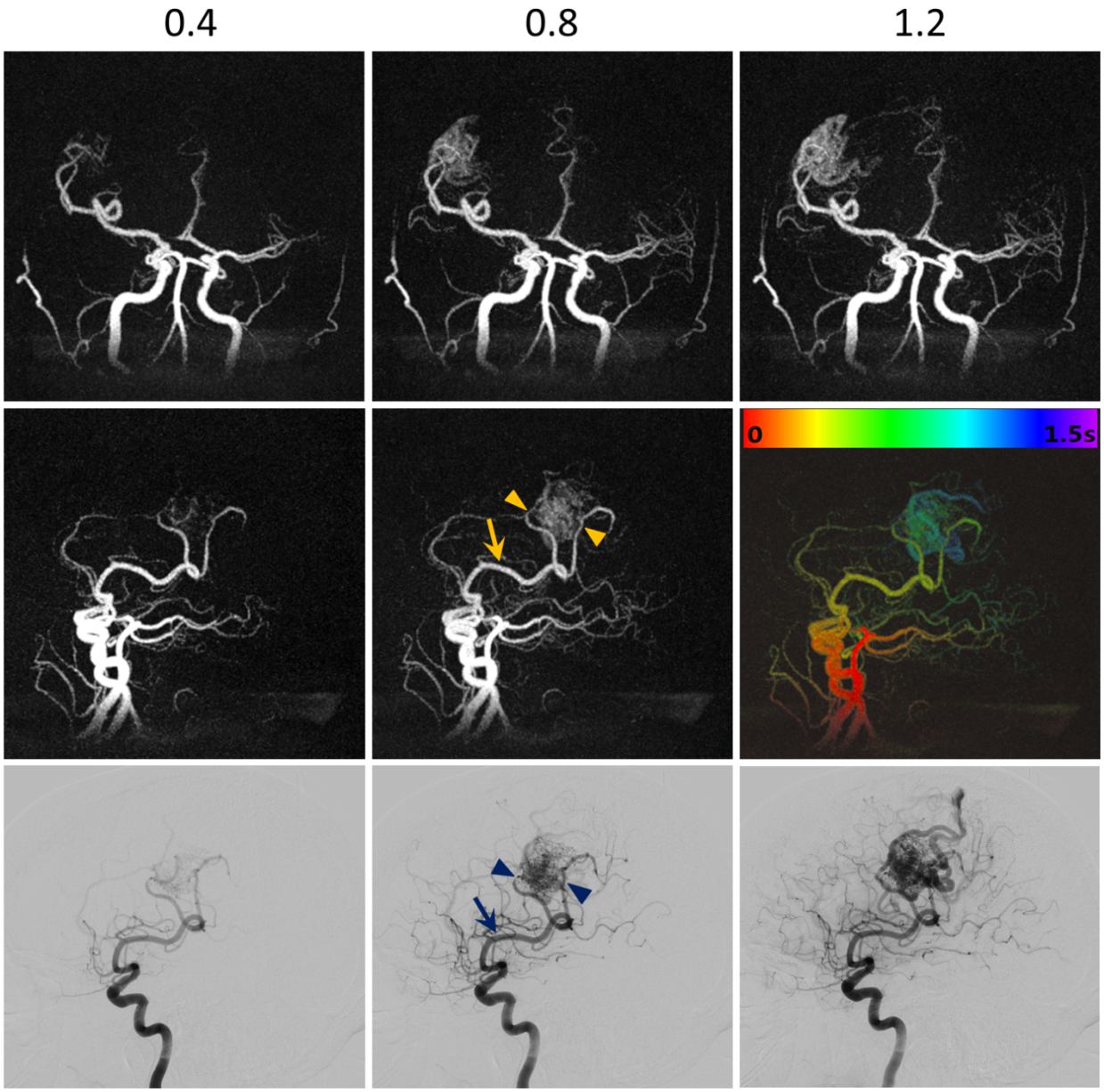

Figure 3.9: Right parietal AVM supplied by branches of the right middle cerebral artery. Rows 1-2 display the dynamic PCASL exam in the coronal and sagittal planes at three time points 0.4, 0.8, and 1.2 s. Colorized TOA map is shown on right in the middle row. Bottom row shows the corresponding lateral projections from the DSA exam. The dynamic PCASL images provide excellent delineation of the right angular artery (arrows) and parietal branches (arrowheads) that supply a well defined AVM nidus. The filling rates of the arterial feeders and normal arteries show good agreement with the DSA exam.

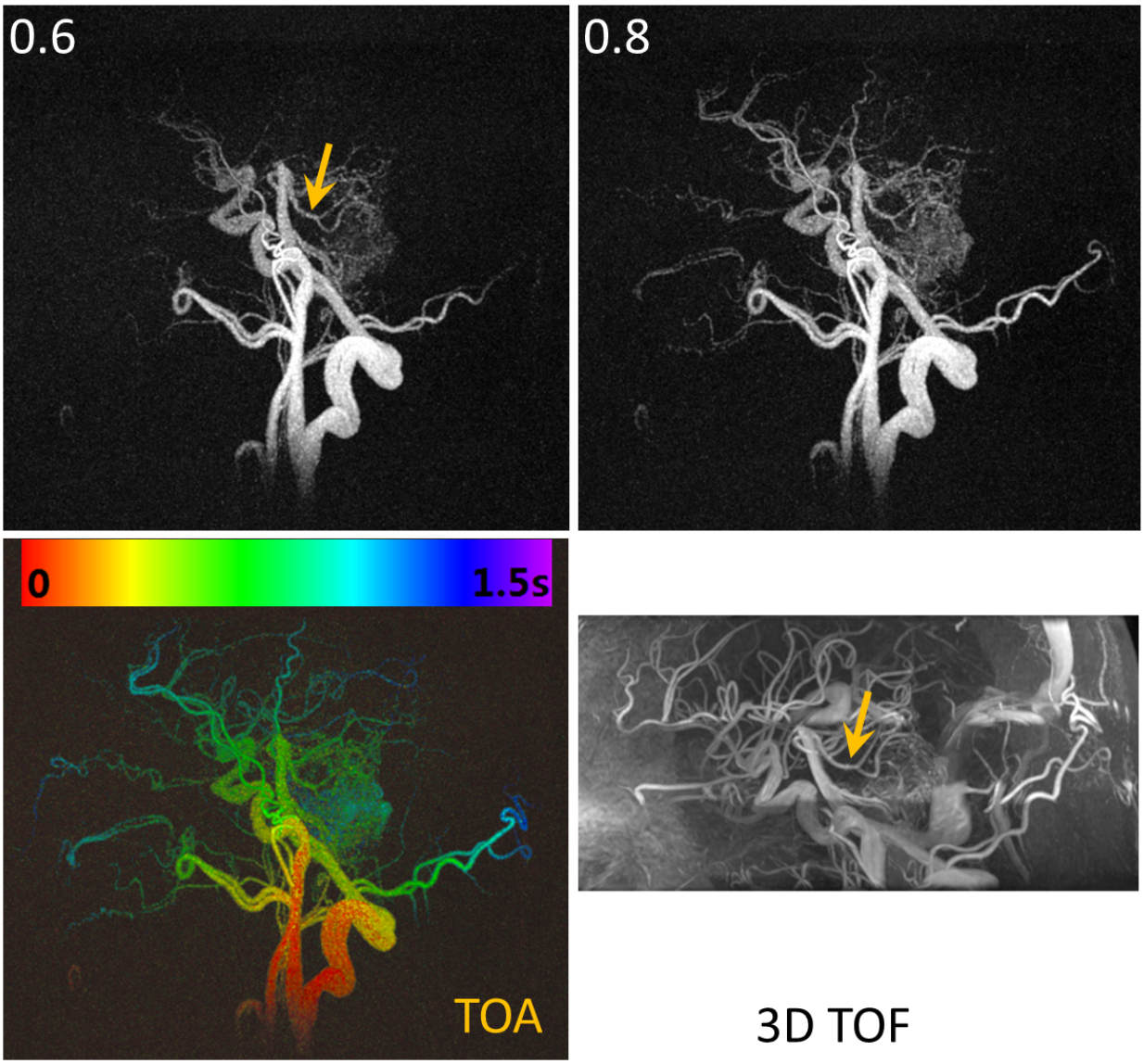

Figure 3.10: Brainstem AVM supplied by the basilar artery via small perforating vessels and superior cerebellar arteries. Row 1 display sagittal MIPs of dynamic PCASL exam at time points 0.6 and 0.8 s. The left image in bottom row is colorized display of TOA map. Sagittal MIP of 3D TOF (bottom right) shows better spatial resolution, but substantial saturation artifacts. The depiction of the superior cerebellar arteries (arrows) in PCASL images agrees with 3D TOF image.

row) and sagittal (middle row) MIPs at three time points 1, 1.5, and 2 s are displayed. Bottom row shows the corresponding lateral projections from the DSA exam. The dynamic PCASL acquisition was obtained with a long tagging duration of 2 s for better visualization of the venous drainage. As the supply of the DAVF, the left posterior meningeal artery (arrows) is excellently delineated on the sagittal MIPs. The longer tagging duration improved visualization of the transverse sinus (open arrows) but was not long enough to demonstrate the cortical venous drainage that was identified on the DSA exam.

3.5 Evaluation

Source images for each dynamic PCASL-VIPR time frame and all source and MIP images of 3D TOF were transferred to a radiology workstation (Horizon Rad Station, version 11.8, McKesson, San Francisco, CA) for evaluation by two experienced neuro-radiologists (P. A. T and D. R.). Both independently evaluated image quality of 3D TOF and dynamic PCASL-VIPR including visualization of proximal vessels, visualization of distal vessels, and saturation artifacts. The first two aspects were graded on a 4 point scale (1 = poor or non-visualized, 2 = visualized but not of diagnostic quality, 3 = visualization adequate for clinical diagnosis, and 4 = excellent image quality). The nonparametric Wilcoxon signed rank method was utilized to test for a significant difference in vessel visualization between PCASL and 3D TOF for both vessel groups. Spearsman correlation test was performed to assess the inter-rater correlation. Saturation artifacts were graded with Y/N (Y = artifacts obscured diagnosis, N = artifacts not obscured diagnosis). Kappa correlation test was performed to assess the inter-rater correlation. The evaluation results of image quality are shown in Table 3.1. The average scores of dynamic PCASL-VIPR and 3D TOF on the visualization of proximal vessels are 3.6 and 3.9 respectively indicating an adequate image quality. The difference in this score between two modalities is not statistically significant (P = 0.15). The

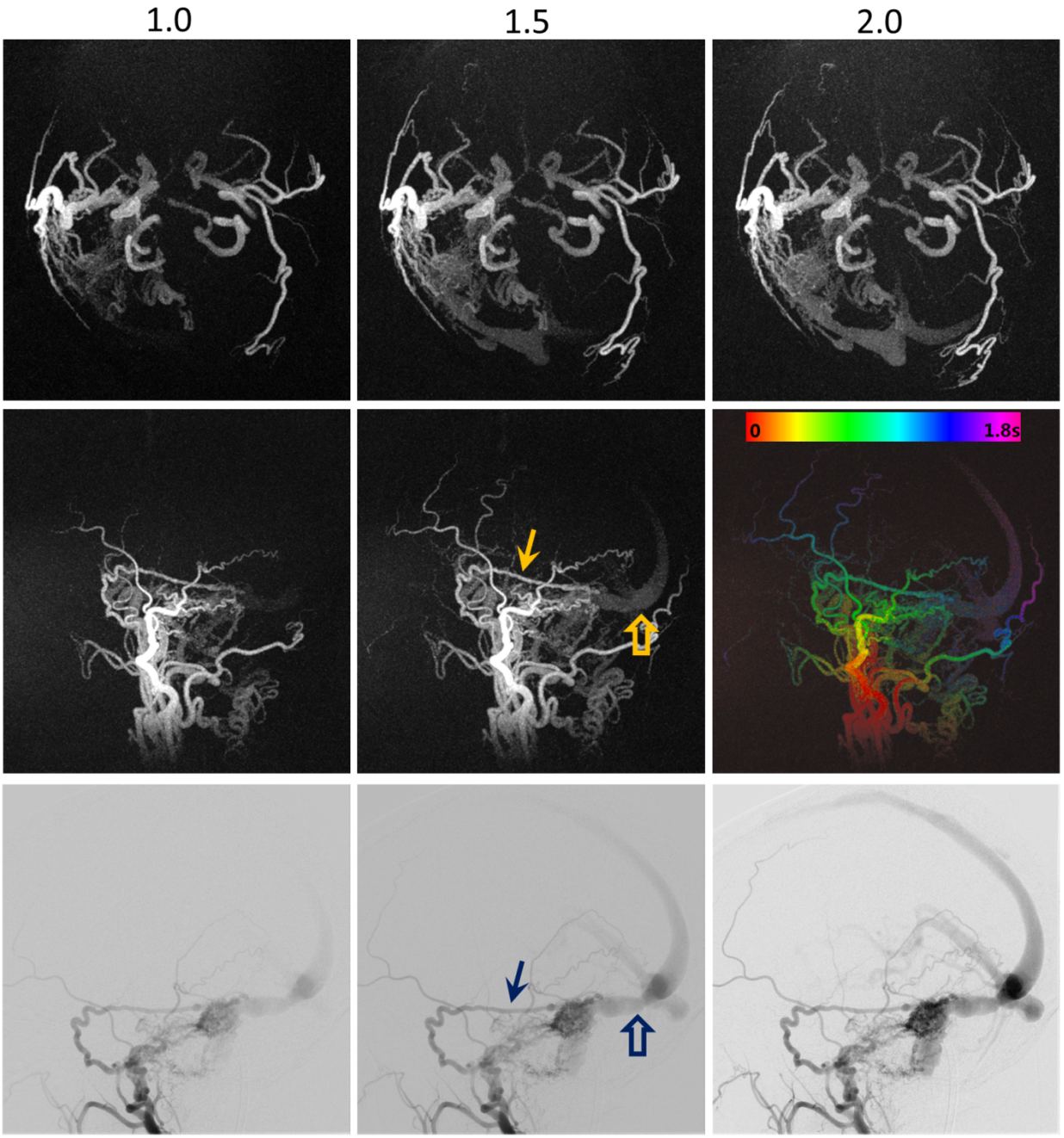

Figure 3.11: Left posterior fossa DAVF supplied by multiple right external corotid artery branches and the right tentorial artery. Rows 1-2 display the dynamic PCASL exam in the axial and sagittal planes at three time points 1 s, 1.5 s, 2.0 s. Row 3 shows the corresponding lateral projections from the DSA exam (right external carotid artery injection). Note the excellent delineation of the left posterior meningeal artery supply to the DAVF (arrows). The longer tagging duration improved visualization of the transverse sinus (open arrows) but was not long enough demonstrate the cortical venous drainage that was identified on the DSA exam.

average scores on the visualization of distal vessels are 2.6 for PCASL exam indicating a slightly inadequate image quality while 3.4 for 3D TOF. The difference in this score is not statistically significant (P = 0.095). The level of inter-rater agreement on these scores is good (Spearmen's rank correlation coefficient $\rho = 0.66$). For saturation artifacts, one rater graded 4 of 5 TOF data and the other one 2 of 5 TOF data as obscuring diagnosis. Both raters graded all dynamic PCASL-VIPR scans showing no artifact effects. The level of inter-rater agreement on this score is moderate (kappa coefficient ê=0.55).

	I/Q Proximal Vessels		I/Q Distal Vessels		Saturation artifacts	
	D-PCASL	3D TOF	D-PCASL	3D TOF	D-PCASL	3D TOF
Patient 1	3/4	4/4	3/3	3/3	N/N	Y/Y
Patient 2	3/4	4/4	2/3	3/4	N/N	Y/Y
Patient 3	3/4	4/4	2/3	4/4	N/N	Y/Y
Patient 4	3/4	4/3	2/2	3/2	N/N	Y/Y
Patient 5	4/4	4/4	3/3	4/4	N/N	Y/Y
Average	3.6	3.9	2.6	3.4		
Inter-rater	0.66(Spearsman)				0.55(kappa)	

Table 3.1: Results of image quality evaluation: two sequences are compared on three criteria (image quality of proximal vessels, image quality of distal vessels, and saturation artifacts).

For pathology evaluation, images from 3D TOF and dynamic PCASL-VIPR were assessed for arterial pedicle, nidus size (only for AVM patients), and classification grade (only for DAVF patients due to the inadequate visualization of venous drainage in AVM patients). Two raters reviewed the data together and did readings in consensus.

The results of evaluation of pathology depiction are shown in Table 3.2 and Table 3.3. To summarize, 7 of 8 arterial pedicles were identified by dynamic PCASL-VIPR and 3D TOF and confirmed by DSA. One additional arterial pedicle was identified by DSA in the fourth patient but missed by both dynamic PCASL-VIPR and 3D TOF. In the two of three AVM patients, nidus size measured by dynamic PCASL and 3D TOF showed good agreement with the DSA measurement (difference < 5 mm). In the other AVM patient, the measurement of

	Arterial pedicle			Nidus size		
	D-PCASL	3D TOF	DSA	D-PCASL	3D TOF	DSA
Patient 1	A1, M1	A1, M1	A1, M1	41-42	45	35
Patient 2	M1	M1	M1	20-25	21	21
Patient 3	Basilar	Basilar	Basilar	30	29	28

Table 3.2: Evaluation of pathology depiction on three AVM patients.

	Arterial pedicle			Classification		
	D-PCASL	3D TOF	DSA	D-PCASL	3D TOF	DSA
Patient 4	Ex Car	Ex Car	Ex Car	Type I	Type I	Type I
			Tentorial			
Patient 4	Ex Car	Ex Car	Ex Car	Type II	Type II A+B	Type II A+B
	Tentorial	Tentorial	Tentorial			

Table 3.3: Evaluation of pathology depiction on two DAVF patients.

dynamic PCASL was 6 mm larger than the DSA measurement while the measurement of 3D TOF was 10 mm larger. The deviation is probably due to the inconsistent measuring location given that the nidus is diffuse. Spezler-Martin classification was not performed with dynamic PCASL data because the tagging duration was not long enough to visualize the venous drainage signal. Spetzler-Martin classification could not be performed for 3D TOF data either due to inadequate visualization of venous drainage suffering from saturation. Benefiting from the high flow of DAVF, Cognard classification of the two DAVF patients was able to be performed on both PCASL and TOF data. One DAVF patient was classified as Type I by both dynamic PCASL and 3D TOF data, and confirmed by DSA. The other DAVF patient was classified as Type II based on dynamic PCASL data while both 3D TOF and DSA gave a classification of Type II A+B. In this case, the reason dynamic PCASL wasn't able to give a more detailed classification is that the tagging duration (2 s) was not long enough to demonstrate the cortical venous drainage.

3.6 Discussion

In this work, we developed an accelerated 4D PCASL-based MR angiography technique which is an extension of our previously proposed 3D PCASL-VIPR technique. With optimized PCASL tagging and accelerated acquisition provided by VIPR, this technique is able to achieve a temporal resolution of 200 ms/frame, isotropic spatial resolution of 0.68 mm3 and whole head coverage with a single scan of 7 minutes. This technique shows promise to provide detailed characterization of angio-architecture and hemodynamics of fast flow brain lesions.

This technique relies on radial sampling to provide not only acceleration but also robustness to artifacts. In digital phantoms, the radial acquisition proved higher image quality compared to Cartesian acquisition. Since the bolus in PCASL exhibits minimal dispersion, dramatic contrast differences due to bolus advancing can be observed between subsequent TR's. A smaller contrast change occurs due to the T1 recovery and RF saturation which approximately follows the exponential decay curve for spins in the volume. In Cartesian sampling, this resulting k-space inconsistency causes severe ghosting artifacts at the leading edge of the bolus and a loss of spatial resolution throughout the image [28] due to magnetization relaxation. In contrast, radial sampling is substantially less sensitive to data inconsistencies [29, 30, 31]. Because the center k-space is sampled every TR throughout the sampling window and the contrast change is evenly distributed between high frequency and low frequency samples, the largest contrast inconsistencies due to bolus advancing only leads to blurring of the leading edge other than structural artifacts. Contrast modulation also causes an increased angular undersampling artifact which appears as additional noise in the image. Radial acquisitions additionally demonstrated improved TOA mapping accuracy over Cartesian also due to the fact that center k-space is collected in every TR. This allowed effective deconvolution of bolus edge blurring.

Recently pulsed ASL scheme with multi-phase SSFP acquisition for 4D dynamic angiog-

raphy has been implemented and validated in brain AVM patients [17]. This technique had demonstrated a fine delineation of the arterial feeders, nidus size and location of the AVM, however a poor detection of draining veins due to short coverage of time window (∼1s). Extending time window will aggravate signal loss due to magnetization relaxation especially RF saturation in later time frames. Several previous works has shown the ability of PCASL to obtain dynamics in angiography. One scheme is to acquire time frames with separate scans which has limited efficiency. Another scheme is to use multi-phase SSFP acquisition after the tagging for scan time efficiency but showed the same problem with PASL based dynamic angiography. Our technique with PCASL shares the same principle as the former scheme that dynamics is obtained by extending tagging duration not the delay time. With a fixed short length of sampling window, the signal loss from RF saturation is limited and equalized amongst all the time frames. Therefore, dynamic PCASL-VIPR provides time frame images with not only higher but also more consistent SNR. Although the drainage of AVM was not visualized in our study due to the not long enough tagging duration compared to the AV shunt transit time, it could be solved easily by extending the tagging duration if higher acceleration factor is provided. Compared to PASL based dynamic angiography, our technique also hold potential to provide vessel selective information.

So far, no study of PCASL based dynamic angiography has been validated in clinical application. In this work, dynamic PCASL-VIPR technique has been validated with a preliminary study including 3 AVM patients and 2 DAVF patients. Image quality evaluation showed comparable results with 3D TOF in vessel visualization and better results in saturation artifacts. The evaluation of pathology delineation demonstrated good depiction of the arterial pedicles, the nidus (in AVM cases) and the draining veins (in DAVF cases). Hemodynamics could be observed from the time series of images or/and the TOA map both of which showed good agreement with DSA exams.

Compared to DSA, our technique still has several limitations. While the 200 ms temporal

resolution is sufficient to delineate the arterial phases of high flow brain lesions, a spatial resolution of 0.68 mm3 still has difficulty in depiction of the ultra thin vessels which are not uncommon in the brain. To obtain higher spatial resolution, SNR will degrade as the voxel size reduces. Since part of the noise come from undersampling artifacts, SNR could be improved by increasing the number of projections or using better reconstruction methods such as constrained reconstruction (HYPR etc.) and compressed sensing. Another way to improve SNR is to use coils with higher sensitivity for reception.

One drawback of ASL based angiography compared to DSA and CE MRA is the signal loss due to T1 recovery during the transit. T1 value of blood in 3T field is about 1.7 s, therefore the inverted spins arriving the location of interest with long transit time from the labeled artery are almost fully recovered even the tagging duration is set long enough for the transit. The resulted little signal difference from the control image makes some feature vessels poorly visualized e.g. the draining veins with slow AV shunting. Therefore, dynamic PCASL angiography has preference in applications with high flow.

Another limitation common to all the ASL methods is the long scan time. A dynamic PCASL scan with typical parameters usually takes 7 – 8 minutes, which makes the method prove to patient motion. If higher SNR is required or longer tagging duration is used for slow flow, the scan time might be even longer making it more difficult for patients to endure. The scan time can be shortened with the usage of novel reconstruction methods to provide higher acceleration factor.

This study is limited by small number of subjects and short tagging duration. In the future, a validation study with larger number of patients and standardized parameters is necessary and the comparison with DSA should include AVM gradings such as Spetzler-Martin classification. The study of TOA mapping also needs further work. Data from a certain number of healthy subjects could be used to assess the normal range of TOAs in certain ROIs. TOAs of patients will be compared to the normal range and discover useful

quantitative measurement for diagnosis. Our TOA mapping method based on ASL can be further validated with comparison to the TOA maps acquired with DSA exam.

Our study of dynamic PCASL angiography has demonstrated its usefulness in brain AVM application. Since this technique is completely non-invasive and contrast free, it will save patients from potential procedural risks, exposure to radiations, and complications from contrast agents. It could be used in preoperative planning, stereotactic-guidance, and post-operative follow up. Other potentials are under development and validation, including vessel selective imaging and acceleration with compressed sensing.

3.7 Hadamard Encoding

To acquire hemodynamics of cerebral vasculature, dynamic PCASL method vary the inflow time of the tagged blood as shown in Figure 3.3. The filling of the arterial tree is presented in a cumulative way. Abnormal flow pattern could be more easily identified if the difference between neighboring time frames is available. The intuitive solution is to subtract the neighboring time frame images to get a difference image. An alternative way is to use a sliding short bolus and image the flow by varying pre-bolus and post-bolus time in different acquisitions. However, both methods dramatically degrade the SNR and the visualization of distal vessels is insufficient for diagnostic purpose.

Hadamard encoding was first used for spatial encoding in vascular territory imaging [32]. Then the concept was extended to temporal encoding for acquiring transit times in perfusion [33, 34]. The basic idea is to prepare multiple blood boli for one image readout instead of only one as in sliding-bolus approach). Each readout has a different combination of the boli according to Hadamard matrix.

Hadamard matrix is a square matrix whose entries are either +1 or -1. A Hadamard

matrix H of order 8 looks as follows:

$$H = \begin{bmatrix} +1 & +1 & +1 & +1 & +1 & +1 & +1 & +1 \\ +1 & -1 & +1 & -1 & +1 & -1 & +1 & -1 \\ +1 & +1 & -1 & -1 & +1 & +1 & -1 & -1 \\ +1 & -1 & -1 & +1 & +1 & -1 & -1 & +1 \\ +1 & +1 & +1 & +1 & -1 & -1 & -1 & -1 \\ +1 & -1 & +1 & -1 & -1 & +1 & -1 & +1 \\ +1 & +1 & -1 & -1 & -1 & -1 & +1 & +1 \\ +1 & -1 & -1 & +1 & -1 & +1 & +1 & -1 \end{bmatrix} \tag{3.1}$$

A characteristic of Hadamard matrix is that $HH^T = I$. So we can use this property to generate arbitrary single bolus readout with a combination of all the readouts that are acquired with temporal Hadamard encoding. To implement this, first the entire PCASL duration is divided into 8 short boli with same length as shown in Figure 3.12. We assign '+1' to bolus that is set on 'control' state (gray segment in the diagram) and '-1' to bolus that is set on 'tag' state (white segment in the diagram). Then, the boli states for each acquisition are designed according to the entries (except the first entry) in a certain row in Hadamard matrix H.

Let Θ be a modified 8x7 Hadamard matrix with the first column of matrix H eliminated.

Then, we have

$$
\begin{aligned}
& \Theta^T \cdot \Theta \\
= & \begin{bmatrix} +1 & -1 & +1 & -1 & +1 & -1 & +1 & -1 \\ +1 & +1 & -1 & -1 & +1 & +1 & -1 & -1 \\ +1 & -1 & -1 & +1 & +1 & -1 & -1 & +1 \\ +1 & +1 & +1 & +1 & -1 & -1 & -1 & -1 \\ +1 & -1 & +1 & -1 & -1 & +1 & -1 & +1 \\ +1 & +1 & -1 & -1 & -1 & -1 & +1 & +1 \\ +1 & -1 & -1 & +1 & -1 & +1 & +1 & -1 \end{bmatrix} \cdot \begin{bmatrix} Phase1 & +1 & +1 & +1 & +1 & +1 & +1 & +1 \\ Phase2 & -1 & +1 & -1 & +1 & -1 & +1 & -1 \\ Phase3 & +1 & -1 & -1 & +1 & +1 & -1 & -1 \\ Phase4 & -1 & -1 & +1 & +1 & -1 & -1 & +1 \\ Phase5 & +1 & +1 & +1 & -1 & -1 & -1 & -1 \\ Phase6 & -1 & +1 & -1 & -1 & +1 & -1 & +1 \\ Phase7 & +1 & -1 & -1 & -1 & -1 & +1 & +1 \\ Phase8 & -1 & -1 & +1 & -1 & +1 & +1 & -1 \end{bmatrix} \\
= & \begin{bmatrix} Phase1 - Phase2 + Phase3 - Phase4 + Phase5 - Phase6 + Phase7 - Phase8 \\ Phase1 + Phase2 - Phase3 - Phase4 + Phase5 + Phase6 - Phase7 - Phase8 \\ Phase1 - Phase2 - Phase3 + Phase4 + Phase5 - Phase6 - Phase7 + Phase8 \\ Phase1 + Phase2 + Phase3 + Phase4 - Phase5 - Phase6 - Phase7 - Phase8 \\ Phase1 - Phase2 + Phase3 - Phase4 - Phase5 + Phase6 - Phase7 + Phase8 \\ Phase1 + Phase2 - Phase3 - Phase4 - Phase5 - Phase6 + Phase7 + Phase8 \\ Phase1 - Phase2 - Phase3 + Phase4 - Phase5 + Phase6 + Phase7 - Phase8 \end{bmatrix} \\
= & 7I
\end{aligned} \tag{3.2}
$$

Using Hadamard encoding, each time frame image is generated by averaging 4 subtracted data, therefore SNR is doubled without extending the scan time.

To demonstrate this technique, we recruited one healthy volunteer for preliminary study. The subject received two scans: one was the standard dynamic PCASL, the other was the Hadamard encoding PCASL. All exams were performed on a clinical 3T MR system (Discovery 750, GE Healthcare, Waukesha, WI, USA) with a 32-channel head coil (32 Ch

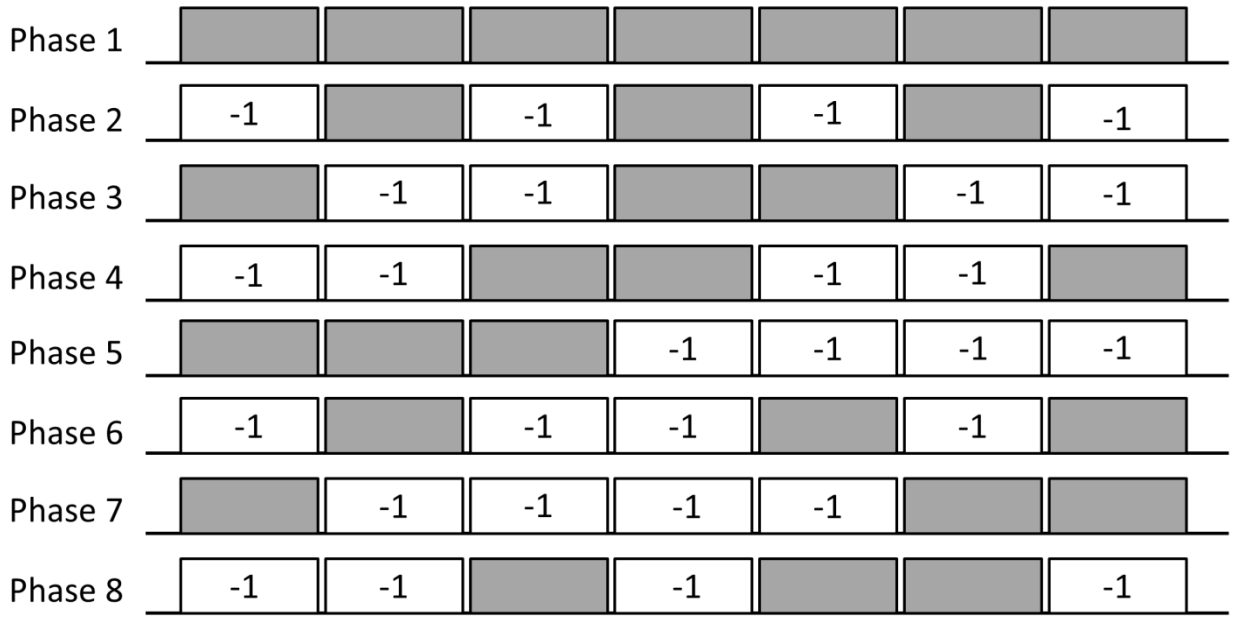

Figure 3.12: PCASL pulse train design with Hadamard encoding: each phase is a unique composition of control state boli and tag state (marked with -1) boli.

Head, MR Instruments, Hopkins, MN, USA). For both scans, the entire PCASL duration was 1.4 s; the sampling window was 500 ms and 3,000 TRs/phase with a total of 8 phases were collected. For standard dynamic PCASL scan, the duration of effective tagging was 0 (control), 200, 400, 600, 800, 1000, 1200, and 1400 ms. For each time frame, the data acquired from the previous phase was subtracted from the current phase data, then was reconstructed using standard algorithm. For Hadamard encoded dynamic PCASL scan, the entire PCASL duration (1.4 s) was divided into 7 segments and the duration of each bolus was 200 ms. For each time frame, the data from all phases were combined according to Hadamard matrix and then reconstructed with standard algorithm.

Representative coronal MIP images from two scans were shown in Figure 3.13. The upper row shows four time frames from Hadamard encoding method. The blood filling pattern can be clearly visualized. The lower row shows three time frames from standard dynamic PCASL (the left time frames were not shown because no vessel signal could be delineated from the

noise). Distal vessels were not sufficiently visualized due to the low SNR.

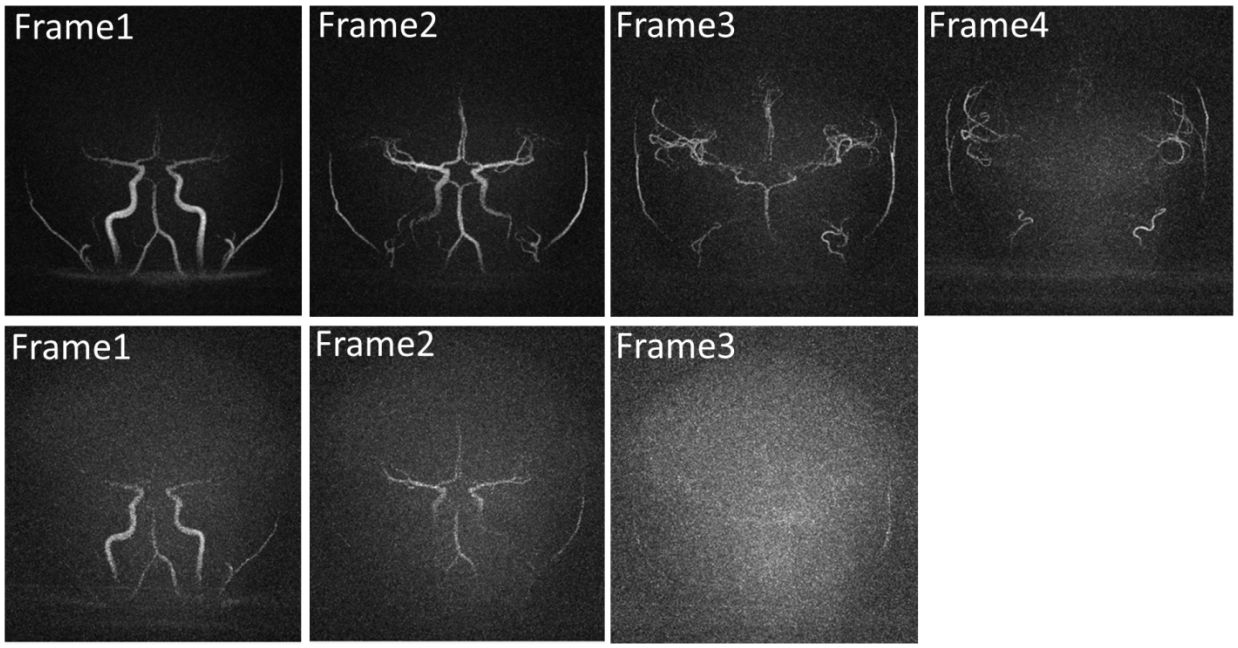

Figure 3.13: Coronal MIPs of a volunteer study: Hadamard encoding (upper row) vs. standard PCASL (lower row).

In future work, we needs more subjects for further validation especially in patients. Another interest is to acquire cumulatively filling time frame images using Hadamard encoding or other temporal encoding methods. The expectation is to see SNR improvements compared to standard dynamic PCASL imaging.

3.8 References

[1] A. Kader, W.L. Young, and J. Pile-Spellman. The influence of hemodynamic and anatomic factors on hemorrhage from cerebral arteriovenous malformations. *Neurosurgery*, 34:801–808, 1994.

[2] R.F. Spetzler, R.W. Hargraves, P.W. McCormick, J.M. Zarbramski, R.A. Flom, and R.A. Zimmerman. Relationship of perfusion pressure and size to the risk of hemorrhage from arteriovenous malformations. *J Neurosurg*, 76:918–923, 1992.

[3] D.R. Buis, J.C. Bot, F. Barkhof, D.L. Knol, F.J. Lagerwaard, B.J. Slotman, W.P. Vandertop, and R van den Berg. The predictive value of 3d time-of-flight mr angiography in assessment of brain arteriovenous malformation obliteration after radiosurgery. *AJNR Am J Neuroradiol*, 33:232–238, 2012.

[4] F. R. Korosec, R. Frayne, and T. M. Grist. Time-resolved contrast-enhanced 3d mr angiography. *Magn Reson Med*, 36:345–351, 1996.

[5] CR Haider, HH Hu, NG Campeau, J III Huston, and SJ Riederer. 3d high temporal and spatial resolution contrast-enhanced mr angiography of the whole brain. *Magn Reson Med*, 60:749–760, 2008.

[6] T.A. Cashen, H. Jeong, M.K. Shah, H.M. Bhatt, W. Shin, J.C. Carr, M.T. Walker, H.H. Batjer, and T.J. Carroll. 4d radial contrast-enhanced mr angiography with sliding subtraction. *Magn Reson Med*, 58:962–972, 2007.

[7] D. C. Peters, F. R. Korosec, T. M. Grist, W. F. Block, J. E. Holden, K. K. Vigen, and C. A. Mistretta. Undersampled projection reconstruction applied to mr angiography. *Magnetic Resonance in Medicine*, 43(1):91–101, 2000.

[8] M Lustig, D Donoho, and JM Pauly. Sparse mri: The application of compressed sensing for rapid mr imaging. *Magn Reson Med*, 58:1182–1195, 2007.

[9] C.A. Mistretta, O. Wieben, J. Velikina, W. F. Block, J. Perry, Y. Wu, and K. M. Johnson. Highly constrained backprojection for time-resolved mri. *Magn Reson Med*, 55:30–40, 2006.

[10] KM Johnson, J Velikina, Y Wu, SR Kecskemeti, O Wieben, and CA Mistretta. Improved waveform fidelity using local hypr reconstruction (hypr lr). *Magn Reson Med*, 2008:456–462, 2008.

[11] J.H. Maki, M.R. Prince, and T.C. Chenevert. Optimizing three-dimensional gadolinium-enhanced magnetic resonance angiography. *Investigative Radiology*, 33(9):528–537, 1998.

[12] P. Marckmann, L. Skov, K. Rossen, A. Dupont, M.B. Damholt, J.G. Heaf, and H.S. Thomsen. Nephrogenic systemic fibrosis: suspected causative role of gadodiamide used

for contrast-enhanced magnetic resonance imaging. *J Am Soc Nephrol*, 17:2359–2362, 2006.

[13] R. R. Edelman, B. Siewert, M. Adamis, J. Gaa, G. Laub, and P. Wielopolski. Signal targeting with alternating radiofrequency (star) sequences: application to mr angiography. *Magn Reson Med*, 31(2):233–238, 1994.

[14] L Yan, S Wang, Y Zhuo, RL Wolf, MF Stiefel, J An, Y Ye, Q Zhang, ER Melhem, and DJJ Wang. Unenhanced dynamic mr angiography: High spatial and temporal resolution by using true fisp - based spin tagging with alternating radiofrequency. *Radiology*, 256(1):270–279, 2010.

[15] X Bi, P Weale, P Schmitt, S Zuehlsdorff, and R Jerecic. Non-contrast-enhanced four-dimensional (4d) intracranial mr angiography: A feasibility study. *Magn Reson Med*, 63:835–841, 2010.

[16] Q. Chen, V. M. Mai, P. Storey, and R. R. Edelman. Dynamic asl flow imaging with cardiac triggered true fisp acquisition, 2001.

[17] S Yu, L Yan, Y Yao, S Wang, M Yang, B Wang, Y Zhuo, L Ai, X Miao, J Zhao, and DJJ Wang. Noncontrast dynamic mra in intracranial arteriovenous malformation (avm): comparison with time of flight (tof) and digital subtraction angiography (dsa). *Magnetic Resonance Imaging*, 2012.

[18] O. Bieri and K. Scheffler. Flow compensation in balanced ssfp sequences. *Magnetic Resonance in Medicine*, 54(4):901–907, 2005.

[19] M. Markl, M.T. Alley, C.J. Elkins, and N.J. Pelc. Flow effects in balanced steady state free precession imaging. *Magn Reson Med*, 50:892–903, 2003.

[20] P. Storey, W. Li, Q. Chen, and R. R. Edelman. Flow artifacts in steady-state free precession cine imaging. *Magn Reson Med*, 51:115–122, 2004.

[21] PM Robson, W Dai, A Shankaranarayannan, NM Rofsky, and DC Alsop. Time-resolved vessel-selective digital subtraction mr angiography of the cerebral vasculature with arterial spin labeling. *Radiology*, 257(2):507–515, 2010.

[22] T.W. Okell, P Schmitt, X Bi, M.A. Chappell, R.H. Tijssen, K.L. Miller, and P Jezzard. 4d vessel-encoded arterial spin labeling angiography. *Proc. Intl. Soc. Mag. Reson. Med. 19*, page 4034, 2011.

[23] Huimin Wu, Walter F. Block, Patrick A. Turski, Charles A. Mistretta, and Kevin M. Johnson. Noncontrast-enhanced three-dimensional (3d) intracranial mr angiography using pseudocontinuous arterial spin labeling and accelerated 3d radial acquisition. *Magnetic Resonance in Medicine*, pages n/a–n/a, 2012.

[24] KS Cover, FJ Lagerwaard, R van den Berg, DR Buis, and BJ Slotman. Color intensity projection of digitally subtracted angiography for the visualization of brain arteriovenous malformations. *Neurosurgery*, 60:511–515, 2007.

[25] MJP Van Osch, J Hendrikse, X Golay, CJG Bakker, and J Van der Grond. Non-invasive visualization of collateral blood flow patterns of the circle of willis by dynamic mr angiography. *Medical Image Analysis*, 10:59–70, 2006.

[26] SJ Riederer, CR Haider, and EA Borisch. Time-of-arrival mapping at three-dimensional time-resolved contrast-enhanced mr angiography. *Radiology*, 253(2):532–542, 2009.

[27] TW Okell, MA Chappell, and MW Woolrich. Vessel-encoded dynamic magnetic resonance angiography using arterial spin labeling. *Magn Reson Med*, 64(3):698–706, 2010.

[28] ET Tan, J III Huston, NG Campeau, and SJ Riederer. Fast inversion recovery magnetic resonance angiography of the intracranial arteries. *Magn Reson Med*, 63:1648–1658, 2010.

[29] M.I. Altbach, E.K. Outwater, T.P. Trouard, E.A. Krupinski, R.J. Theilmann, A.T. Stopeck, M. Kono, and A.F. Gmitro. Radial fast spin-echo method for t2-weighted imaging and t2 mapping of the liver. *J Magn Reson Imaging*, 16:179–189, 2002.

[30] R.J. Theilmann, A.F. Gmitro, M.I. Altbach, and T.P. Trouard. View-ordering in radial fast spin-echo imaging. *Magn Reson Med*, 51:768–774, 2004.

[31] B.H. Holmes, R.L. O'Halloran, E.K. Brodsky, Y. Jung, W.F. Block, and S.B. Fain. 3d hyperpolarized he-3 mri of ventilation using a multi-echo projection acquisition. *Magn Reson Med*, 59:1062–1071, 2008.

[32] E.C. Wong. Vessel encoded arterial spin labeling using pseudo-continuous tagging. *Proc. Intl. Soc. Mag. Reson. Med. 14*, page 668, 2006.

[33] J.A. Wells, M.F. Lythgoe, D.G. Gadian, R.J. Ordidge, and D.L. Thomas. In vivo hadamard encoded continuous arterial spin labeling (h-casl). *Magn Reson Med*, 63:1111–1118, 2010.

[34] M Guenther. Highly efficient accelerated acquisition of perfusion inflow series by cycled arterial spin labeling. *Proc. Intl. Soc. Mag. Reson. Med. 15*, 2007.

4 Acceleration with Compressed sensing

4.1 Introduction

The conventional practice for data acquisition is based on Nyquist sampling theory, which states that for the accurate reconstruction of a band-limited signal or image, the sampling rate must at least double the highest frequency of the signal or image. This theory does not account for additional signal structures that might be known a priori. Recently, compressive sensing (CS) has attracted major attention, which shows that a high-quality signal or image can be reconstructed from far fewer measurements than what is usually required by the Nyquist sampling theorem [1, 2, 3].

CS-based image reconstruction presents several potential benefits for MRI, e.g., reduced scan times, higher resolution imaging, dynamic imaging, etc. and may enable new applications. Therefore, CS has received much attention in the MRI community over the past few years [4].

The CS approach requires that: (a) the desired image has a sparse representation in a known transform domain, (b) the aliasing artifacts due to k-space undersampling be incoherent (noise like) in that transform domain. (c) a nonlinear reconstruction be used to enforce both sparsity of the image representation and consistency with the acquired data.

CS is particularly suitable for PCASL-VIPR angiography. Background signal is sub-

tracted leaving very sparse signal from the arterial vessels; the VIPR trajectory is a 3D incoherent sampling scheme in which the interference spreads in all three dimensions and the undersampling artifacts have noise like appearance. Intracranial angiography requires higher spatial resolution and temporal resolution that needs acceleration to keep the scan time in clinical acceptable range. PCASL-VIPR angiography could benefit a lot with the help from compressed sensing.

4.2 Compressed Sensing (CS) basics

Suppose the image of interest is a vector $\vec{m}$, let Ψ denote the linear operator that transforms from pixel representation into a sparse representation, and let E be the encoding matrix (undersampled Fourier transform) and $\vec{f}$ is the measured k-space data from the scanner. The CS principle states that one can recover $\vec{m}$ from $\vec{(}f)$ by solving the following constrained optimization problem (P1):

$$minimize\|\Psi\vec{m}\|_1, s.t.\|E\vec{m} - \vec{f}\|_2 < \epsilon \tag{4.1}$$

The objective function in Eq. 4.1 is the L_1 norm. Minimizing $\|\Psi\vec{m}\|_1$ promotes sparsity. The constraint $\|E\vec{m} - \vec{f}\|_2 < \epsilon$ enforces data consistency. ϵ controls the fidelity of the reconstruction to the measured data and is usually set below the expected noise level.

Traditionally, the problem of finding sparse solutions has been catalogued as belonging to a class of combinatorial optimization problems, whereas (P1) can be solved by linear programming and is thus dramatically more tractable in general. However, large-scale problems are simply too large for general-purpose strategies to be used in routine processing. This, together with the fact that f may contain noise in certain applications, makes solving the unconstrained problem (P2)

$$min\lambda\|\Psi\vec{m}\|_1 + \|E\vec{m} - \vec{f}\|_2^2 \tag{4.2}$$

more preferable than solving the constrained problem P1. Because P2 also allows the constraint $E\vec{m} = \vec{f}$ to be relaxed, it is used when the measurement $\vec{f}$ is contaminated by encoding errors such as noise.

The equivalence of P2 to the problem P1 has been mentioned in many papers, but how to calculate λ from ϵ and vice versa to obtain an equivalent pair is still an open problem.

The L_1-regularized least square problem (LSP) can be transformed to a convex quadratic problem, with linear inequality constraints. The equivalent quadratic program (QP) can be solved by standard convex optimization methods such as interior-point methods [5]. Standard interior-point methods are implemented in general purpose solvers which can only handle small and medium size problems. Specialized interior-point methods such as [6] uses the preconditioned conjugate gradients algorithm to compute the search direction can solve large scale L_1-regularized LSP. Other methods proposed for solving L_1-regularized LSPs include homotopy and variants which are very fast if the solution is extremely sparse, otherwise can be slow which is often the case for large scale problems. Other computational methods include coordinate-wise descent methods [7], a fixed-point continuation methods [8], Bregman iterative regularization based methods [9] , bound optimization methods [10], iterated shrinkage methods [11] , gradient methods [12], and gradient projection algorithms [13]

4.3 Iterative thresholding

One of the most popular methods for solving CS problem is in the class of iterative thresholding algorithms, see, e.g., [14] [11] [15] [16]. The algorithm is composed of two stages: optimization

of the least square term and decreasing of L1 norm. The former stage is accomplished by solving the optimization problem without L1 penalty, while the later stage is finished by thresholding.

The iterative thresholding method for the minimization problem with the cost function in Eq. 1 may be described as a gradient descent type method with thresholding in each iteration. Image is updated with the following equation:

$$\vec{f}^{(n)} = \Psi^{-1} T \Psi(\vec{m}^{n-1} + E^T(\vec{f} - E\vec{m}^{n-1})) \tag{4.3}$$

Here, $\vec{f}^{(n)}$ denotes the solution at the nth iteration, Ψ and Ψ^{-1} denote forward and inverse sparsifying transform operators, respectively. $E^H$is the backprojection operator from k-space to image space, T_t is the thresholding operator with threshold of t. The iteration generates a sequence that converges in norm to a minimizer of $\phi(\vec{f})$.

Iterative thresholding framework offers reduced memory footprint for large problems and stable, although with slow convergence. When applied to MR imaging applications [17], the computations typically involve only Fourier and sparsifying transform, both of which can be implemented efficiently and the only additional computation cost is a thresholding operation on the transformed coefficients. In particular, computationally demanding cost function/gradient evaluations and line searches are not required.

There are two kinds of thresholding as shown in figure 4.1. The hard-threshold function keeps the input if it is larger than the threshold t; otherwise, it is set to zero.

$$\psi_t(x) = x \cdot 1|x| > t \tag{4.4}$$

The soft-threshold function (or called shrinkage function) takes the argument and shrinks it

toward zero by the threshold t.

$$\eta_t(x) = sgn(x) \cdot max(|x| - t, 0) \tag{4.5}$$

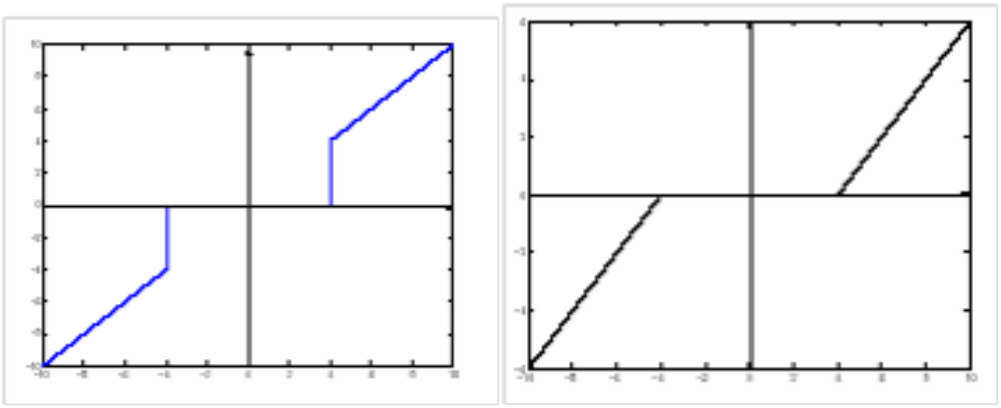

(a) (b)

Figure 4.1: Diagram of Soft thresholding (left) vs. hard-thresholding (right)

The classic interpretations of iterative thresholding for solving constraint L1 norm optimization were reported previously. For theoretic analysis, Herrity et al employed hard iterative thresholding to demonstrate that one could recover the k-term representation of the original signal up to any prescribed error tolerance under certain conditions. Their simulation results showed that soft iterative thresholding performed better than hard thresholding. Bredies and Lorenz proved that soft iterative thresholding converged with a linear rate once the underlying operator satisfied the finite basis infectivity property or the minimizer possessed a strict sparsity pattern.

The soft-thresholding rule is advantageous over hard-thresholding for several reasons. First, soft-thresholding has been shown to achieve near-optimal minimax rate over a large range of Besov spaces. Second, for the generalized Gaussian prior assumed in this work, the optimal soft-thresholding estimator yields a smaller risk than the optimal hard-thresholding

estimator. Lastly, in practice, the soft-thresholding method yields more visually pleasant images over hard-thresholding because the latter is discontinuous and yields abrupt artifacts in the recovered images, especially when the noise energy is significant. In what follows, soft-thresholding will be the primary focus.

As for complex thresholding, the soft thresholding operator becomes:

$$T_t(x) = (\|x\| - t)_+ exp(iarg(x)) \tag{4.6}$$

With $(\cdots)_+$ denoting the positive part of the quantity inside brackets.

4.4 Threshold selection

The threshold balances the L2-norm data consistency term and the L1-norm sparsity term. The image quality of the solution to the minimization problem is a complex function of the relative weights on the data consistency and sparsity terms. For the best diagnostic image quality with the available data, the CS algorithms need empirical tuning of the free parameters – a scenario that is not best suited to clinical applications. For successful introduction of CS reconstruction algorithms in a clinical setting, it is necessary to have fast robust algorithms that are fully data-driven and can automatically account for noise, and patient-to-patient or anatomical variability in images. Although there have been increasing interests in free parameter tuning for CS problems, an efficient and automatic tuning method is still lacking. If we define the sparsifying transform specifically to wavelet, there have been quite a few threshold selection schemes that we could borrow from wavelet shrinkage method of denoising problems.

Wavelet shrinkage method of denoising problems

Wavelet shrinkage [18, 19, 20, 21, 22] is a signal estimation technique that exploits the capabilities of wavelet transform for signal denoising. The theoretical formalization of filtering additive iid (independent and identically distributed) Gaussian noise (of zero-mean and standard deviation) via thresholding wavelet coefficients was pioneered by Donoho and Johnstone [18]. A wavelet coefficient is compared to a given threshold and is set to zero if its magnitude is less than the threshold; otherwise, it is kept or modified. The threshold acts as an oracle which distinguishes between the insignificant coefficients likely due to noise, and the significant coefficients consisting of important signal structures. Thresholding rules are especially effective for signals with sparse or near-sparse representations where only a small subset of the coefficients represents all or most of the signal energy.

Let the signal be $f_i, i = 1, \ldots, N$. It has been corrupted by additive noise and one observes

$$g_i = f_i + \epsilon_i, i = 1, \ldots, N \tag{4.7}$$

where ϵ_i are iid as normal $N(0, \sigma^2)$ and independent of f_i. The goal is to remove the noise, or "denoise" g_i, and to obtain an estimate $\bar{f_i}$ of f_i which minimizes the mean squared error (MSE)

$$MSE(\bar{f}) = \frac{1}{N}\sum_{i=1}^{N}(\bar{f_i} - f_i)^2 \tag{4.8}$$

Let $\vec{g} = g_{ii}$, $\vec{f} = g_{ii}$, $\vec{\epsilon} = \epsilon_{ii}$. Let $\vec{Y} = \vec{W}\vec{g}$ denote the matrix of wavelet coefficients of $\vec{g}$, where **W** is the two-dimensional dyadic orthogonal wavelet transform operator The goal is to estimate the signal $\vec{f}$ from the noisy observations $\vec{g}$ such that the Mean Square Error (MSE) is minimum. To achieve this $\vec{g}$ is transformed into wavelet domain, which decomposes $\vec{g}$ into many frequency bands. The small coefficients in the subbands are dominated by noise, while coefficients with large absolute value carry more signal information than noise.

Replacing noisy coefficients (small coefficients below certain value) by zero and an inverse wavelet transform may lead to reconstruction that has lesser noise.

The efficacy of denoising depends heavily on the choice of the thresholds. Researchers have developed various techniques for choosing thresholds. The most well-known methods include VisuShrink [18], SureShrink [19], and BayesShrink [23].

VisuShrink

VisuShrink which was proposed by Donoho (1995), is also called the Universal Threshold, or the Fixed Form threshold It calculates the value based on the number of data points and the noise estimate using formulae:

$$T = \sigma\sqrt{2\log(n)} \tag{4.9}$$

Where σ is the noise estimate, and n is the number of data points.

There are two variants of the universal threshold called single level noise (sln) estimate and multi level noise (mln) estimate. The former one estimate the noise based on the wavelet coefficients of the detail subband at the first decomposition level, and the threshold calculated from that is used for all levels; the latter one estimate the noise from the detail coefficients at each level of decomposition, and adjust the threshold value for each level.

VisuShrink offers the advantages of smoothness and adaptation and performs well under a number of applications. However, VisuShrink is found to yield an overly smoothed estimate and does not adapt well to discontinuities in the signal. It is known to exhibit visual artifacts.

SURE

SURE threshold is calculated based on Stein's Unbiased Risk Estimator [24]. This method specifies a threshold value t_j for each resolution level j in the wavelet transform which is referred to as level dependent thresholding.

Let $\vec{\mu} = (\mu_i : i = 1, \ldots, d)$ be a d-dimensional vector, and let $x_i \sim N(\mu_i, 1)$ be multivariate normal observations with that mean vector. Let $\hat{\mu} = \hat{x}(x)$ be a particular fixed estimator of μ. Charles Stein (1981) introduced a method for estimating the loss $\|\hat{\mu} - \mu\|^2$ in an unbiased fashion. Stein showed that for a nearly arbitrary, nonlinear, biased estimator, one can nevertheless estimate its loss unbiasedly.

Write $\hat{\mu}(x) = x + g(x)$. Stein showed that when g(x) is weakly differentiable, then

$$E_\mu \|\hat{\mu}(x) - \mu\|^2 = d + E_\mu \|g(x)\|^2 + 2 \bigtriangledown \cdot g(x) \tag{4.10}$$

Now consider the soft threshold estimator $\eta_t(x)$, and apply Stein's result. The quantity

$$SURE(t; x) = d - 2 \cdot \#i : |x_i| \leq t + \sum_{i=1}^{d} (|x_i| \wedge t)^2 \tag{4.11}$$

is an unbiased estimate of risk $E_\mu \|\hat{\mu}(x) - \mu\|^2$

Consider using this estimator of risk to select a threshold: $t^s = argmin_{t \geq 0} SURE(t; x)$. For large dimension d, the Law of Large Numbers will ensure that SURE is close to the true risk, and t^s will be almost the optimal threshold for the case at hand.

The optimization problem is computationally straightforward. First, x_i is reordered in order of increasing $|x_i|$. Then on intervals of t which lie between two value of $|x_i|$, SURE(t) is strictly increasing. Therefore the minimum value t^s is one of the data values $|x_i|$. The collection of all values SURE($|x_i|$) is computed. Then the one of $|x_i|$ giving the minimum SURE is t^s.

SureShrink

The SURE principle just described has a serious drawback in situations of extreme sparsity of the wavelet coefficients. In such cases, the noise contributed to the SURE profile by the many

coordinates at which the signal is zero swamps the information contributed to the SURE profile by the few coordinates where the signal is nonzero. Consequently, SureShrink employs a Hybrid scheme. SureShrink proposed by Donoho and Johnstone and is a combination of the universal threshold and the SURE threshold.

In detail, the Hybrid method works as follows: Let $\eta_d = \log_2(d)^{3/2}$ and define $s_d^2 = d^{-1}\sum_i(x_i^2 - 1)$,

$$t = \begin{cases} t_d^F & s_d^2 \leq \eta_d \\ min(t^s, t_d^F) & s_d^2 \leq \eta_d \end{cases} \tag{4.12}$$

BayesShrink

BayesShrink was proposed by Chang, Yu and Vetterli . The formulation is grounded on the empirical observation that the wavelet coefficients in a subband of a natural image can be summarized adequately by a generalized Gaussian distribution (GGD). This observation is well-accepted in the image processing community It follows from this observation that the average MSE (in a subband) can be approximated by the corresponding Bayesian squared error risk with the GGD as the prior applied to each in an iid fashion. The goal is to find the soft-threshold that minimizes this Bayesian risk. The proposed Bayesian risk minimization is subband-dependent.

The Bayes threshold t_B is defined:

$$t_B = \sigma^2/\sigma_s \tag{4.13}$$

where σ is the noise estimate and σ_s is the signal variance without noise. From the definition of additive noise we have

$$w_i = s_i + n_i \tag{4.14}$$

Since the noise and the signal are independent of each other, it can be stated that

$$\sigma_w^2 = \sigma_s^2 + \sigma^2 \tag{4.15}$$

σ_w can be computed as:

$$\sigma_w^2 = \frac{1}{n}\sum_i^n (w_i - mean(w))^2 \tag{4.16}$$

The variance of the signal is computed as:

$$\sigma_s = \sqrt{max(\sigma_w^2 - \sigma^2, 0)} \tag{4.17}$$

We note that the use of adaptive thresholding for sparsity constraint is a deviation from the strict theory, but could be advantageous from an overall image quality standpoint compared with using a fixed threshold. Furthermore, it avoids the necessity of tuning the fixed global threshold empirically depending on the imaging application.

4.5 preliminary study

Two subjects were recruited for a preliminary study. Both subject were scanner on a clinical 3T MR system (Discovery 750, GE Healthcare, Waukesha, WI, USA) with a 32-channel head coil (32 Ch Head, MR Instruments, Hopkins, MN, USA). Standard reconstruction method (labeled as PILS in later experiments) that has been used in our previous PCASL-VIPR studies were performed and worked as a basis for comparison. In PILS, individual coil images were first reconstructed using an optimized gridding routine and then were combined using coil sensitivities estimated from the center of k-space.

The first subject was imaged with a dynamic PCASL-VIPR sequence with the following parameter: FOV = 22×22×16 cm^3, the sampling window = 500 ms 3,000 TRs/frame were

collected for each of the 7 time frames. Data of the last time frame with a tagging duration of 1.2 s was extracted for experiment.

In the first experiment, manual threshold selection was tested. A series of thresholds (defined as a ratio multiplied by the maximum value of wavelet coefficients) were applied to the IST algorithm to investigate the effects of threshold magnitude. The entire 3000 projections were first used in the reconstruction with PILS, then 1500 projections (acceleration factor of 2X) were used with PILS and IST algorithm.

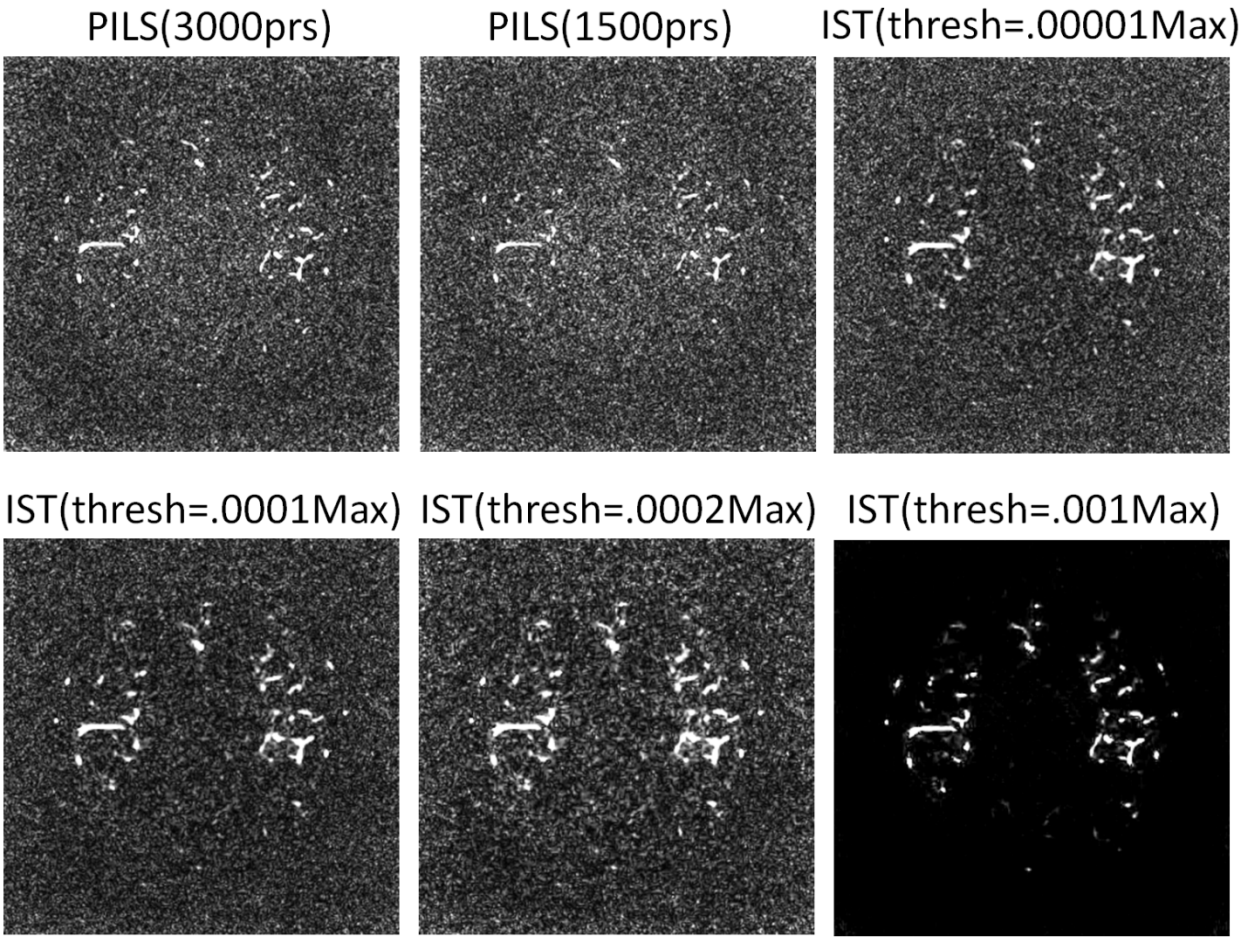

Figure 4.2: Axial slice No. 150 of reconstruction of PILS (3000 projections), PILS (1500 projections), IST (1500 projections) with varying threshold.

Slice No. 150 of the 320 axial slices of reconstruction was compared among the methods

and threshold selections as shown in Figure 4.2. We can see that with IST method, the visualization of vessels was highly improved compared with PILS. When the threshold increased, the signal from vessel details was brighter. However, it comes with the blurring of the vessels and changing of noise pattern which might interfere with the diagnosis. The source images were presented to a senior radiologist and the one with a threshold of 0.0001Max was deemed as having the best quality for diagnostic purpose.

Then, we need to investigate the data-driven threshold selection methods. Three methods were compared: VisuShrink, SureShrink, BayesShrink. Unlike the empirically selected threshold which was applied to every coefficient of the wavelet transformation without difference, in the data-driven threshold selection methods, the threshold for each coefficient might vary depending on the subband or decomposition scale this coefficient locates.

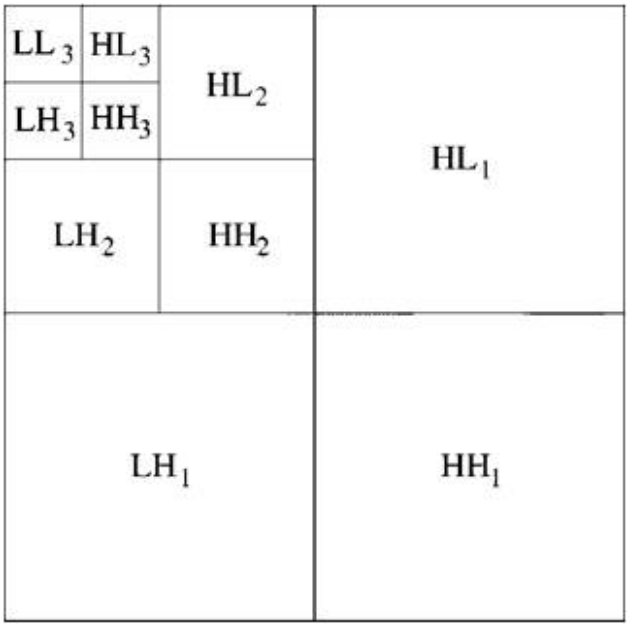

Figure 4.3: The diagram of wavelet decomposition

To take 2D image for example, it is convenient to label the subbands of the transform as in Figure 4.3. The subbands HH_j , HL_j ,LH_j , $j = 1, 2, \ldots , J$, are called the details, where j is the scale, with J being the largest scale in the decomposition, and a subband at scale j

has size $N/2^k \times N/2^k$. The subband LL_J is the low resolution residual.

Noise varians was estimated from subband HHH_1 (in 3D case) of the wavelet transformation as follows:

$$\sigma = \frac{MAD}{0.6745}, \tag{4.18}$$

where $MAD = median_i(|w_i - median_j(w_j)|)$ $(w_i, w_j \in HHH_1)$.

For VisuShrink and SureShrink, the threshold is calculated for all the details bands combined in every scale, while in BayesShrink, the threshold is calculated for each subband in every scale.

Slice No. 150 of the 320 axial slices of reconstruction was compared among different threshold selection methods as shown in Figure 4.4 All the three data-driven threshold selection methods greatly improved the visualization of the vessels. SureShrink and BayesShrink showed similar performance and noise pattern. VisuShrink calculated a relatively big threshold due to the big number of coefficients. The noise in the image of VisuShrink has been dramatically diminished. Limited MIPs with a thickness of 6.875 mm were compared in Figure 4.5. In this figure, BayesShrink can be better distinguished from SureShrink. The background noise in the head region was more diminished in the former. We can observe a noise pattern change in the liminted MIP of VisuShrink as well as a noticeable blurring of vessels. In fact, the thresholds calculated from VisuShrink are the biggest, the ones of SureShrink the smallest, and the one of BayesShrink in the middle among the three data-driven threshold selection methods.

In another experiment, a healthy volunteer was scanned with high resolution static PCASL-VIPR sequence. Scan parameters are as follows: Tagging duration = 3 s, sampling window length = 1 s, FOV = 220x220x160 mm^3, isotropic resolution = 0.43 mm, flip angle = 9. A total of 8906 projections were acquired in a scan time of 8 min. Dataset was reconstructed with IST frame with three automatic threshold selection methods: VisuShrink,

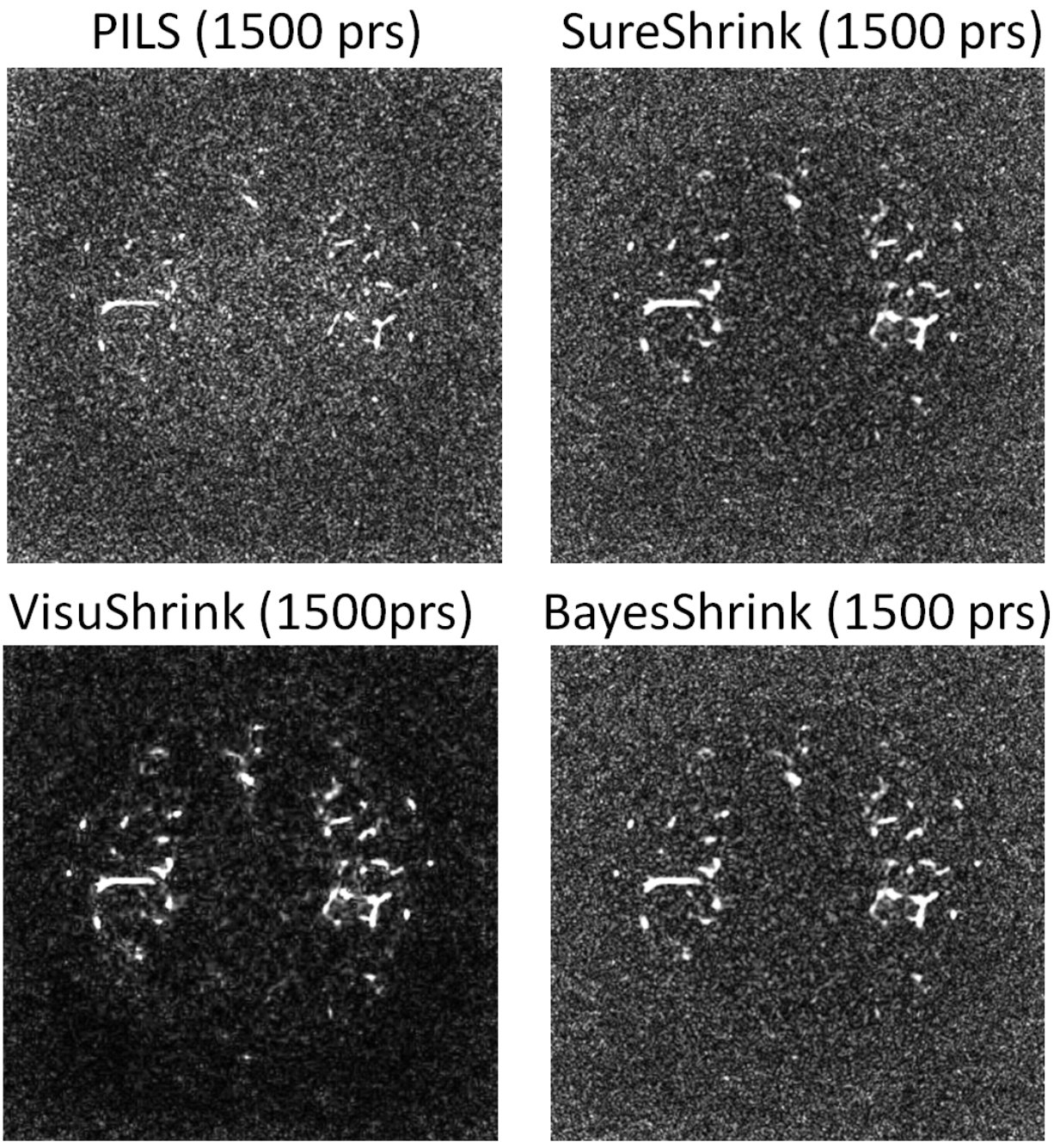

Figure 4.4: Axial slice image of the first subject. Comparison are among standard reconstruction (PILS) and IST with three threshold selection methods: VisuShrink, SureShrink, BayesShrink.

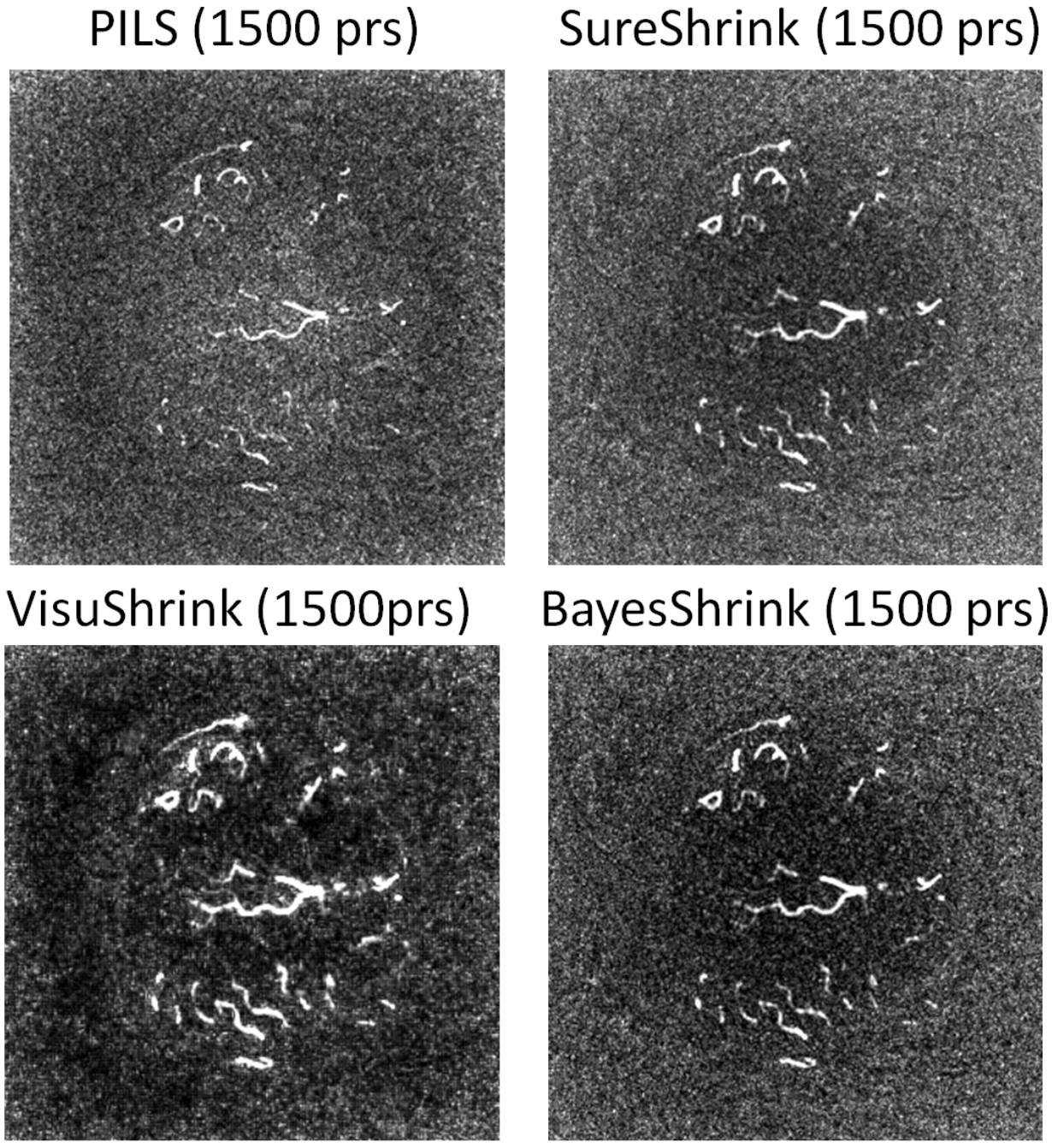

Figure 4.5: Limited axial MIPs with thickness of 6.875 mm of the first subject. Comparison are among standard reconstruction (PILS) and IST with three threshold selection methods: VisuShrink, SureShrink, BayesShrink.

SureShrink, and BayesShrink. Parameters for IST reconstruction are: number of scales of wavelet decomposition = 4; number of iterations = 50; reconstruction matrix size = 512x512x512. Limited MIPs with a thickness of 8 mm from Compressed Sensing and PILS were compared in Figure 4.6.

From the images, we can see that SNR has greatly improved with compressed sensing reconstruction compared with standard non-iterative method. SureShrink and BayesShrink performed equally well. However, the images reconstructed with universal threshold are lower in resolution and show wavelet artifacts that may interfere with diagnosis.

4.6 Discussion

Assessment of the intracranial vasculature requires flow insensitive techniques with high spatial resolution. This is challenging to achieve with contrast enhanced MRA and 3D time of flight (TOF), due to rapid bolus passage and flow saturation artifacts respectively. In previous chapter, 3D angiography techniques PCASL-VIPR have demonstrated whole head coverage with 0.7 mm isotropic resolution and reduced sensitivity to flow. This resolution is still inferior to TOF and may be insufficient for visualization of small intracranial aneurysms. Achieving higher resolution is challenging due to currently high acceleration levels. PCASL angiography is, in principle, highly amenable to compressed sensing (CS) which may provide additional acceleration. However, considerable challenges exist including selection of CS tuning parameters and computational complexities arising from Non-Cartesian sampling.

In this work, we combine compressed sensing, parallel imaging and 3D Non-Cartesian sampling. This iterative reconstruction method provides additional acceleration for the current ASL angiography. When applied to high resolution 3D ASL angiography (higher undersampling factor due to increased TR and required projections calculated from Nyquist), CS was able to improve image quality and apparent SNR. Furthermore, we demonstrate

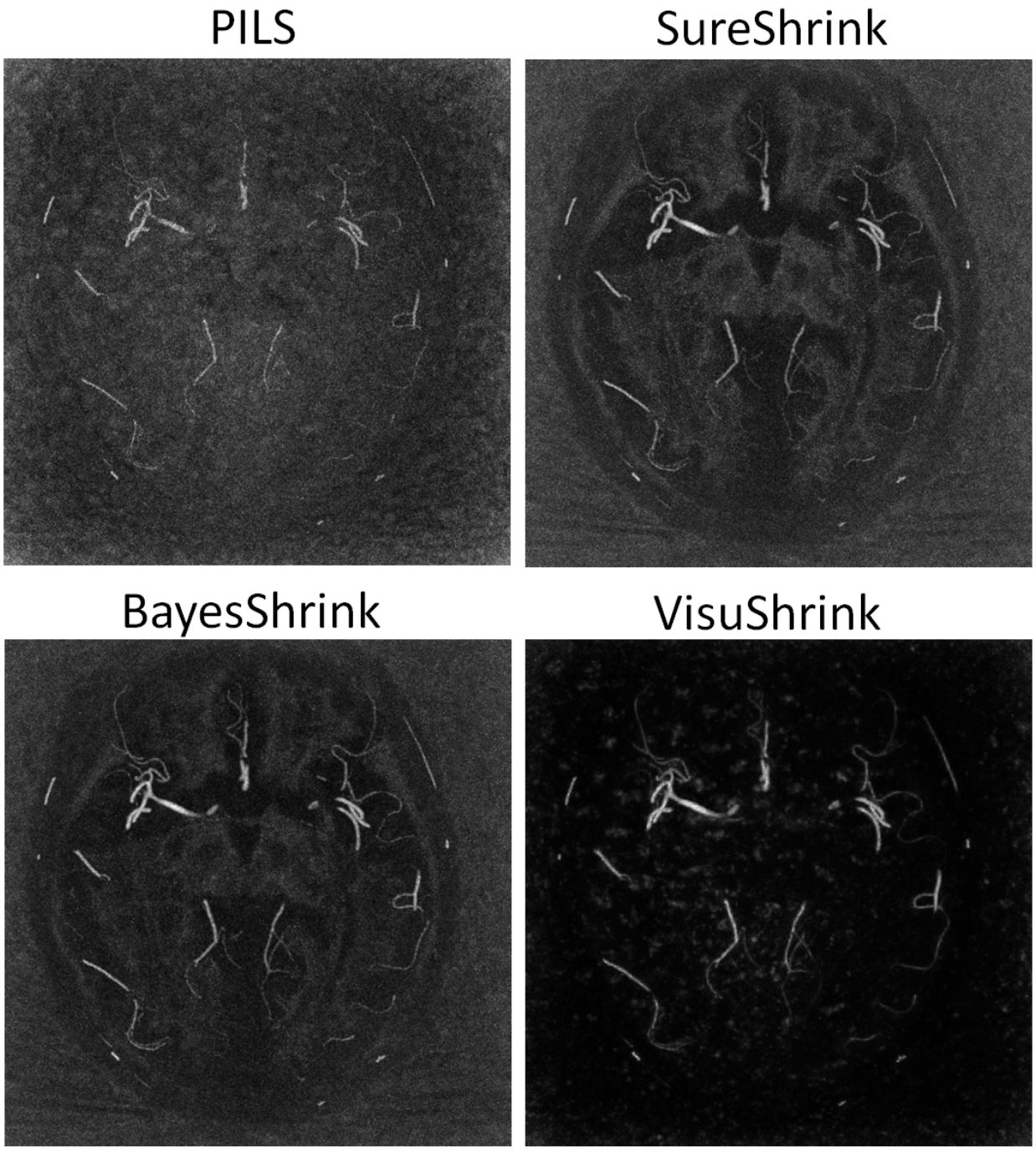

Figure 4.6: Limited axial MIPs with thickness of 8 mm reconstructed by standard non-iterative method (PILS), CS with SURE threshold (SURE), CS with Bayes threshold (BayesShrink), and CS with universal threshold (VisuShrink).

the use of data driven tuning which avoids time consuming tuning of CS algorithm. Three data-driven threshold selection methods were compared. SureShrink and BayesShrink tends to calculate a relatively conservative threshold while VisuShrink calculate a much bigger threshold due to the large matrix size of 3D image.

For CS reconstruction, wavelet may not be the optimum choice of sparsifying transform. In the future work, we might test other options like the image itself or different image.

4.7 References

[1] DL Donoho. Compressed sensing. *IEEE Trans. on Information. Theory*, 52:1289–1306, 2006.

[2] E Candes, J Romberg, and T Tao. Robust uncertainty principles: Exact signal reconstruction from highly incomplete frequency information. *IEEE Trans. Inform. Theory*, 52:489–509, 2006.

[3] E Candes and T Tao. Near optimal signal recovery from random projections: Universal encoding strategies? *IEEE Trans. Inform. Theory*, 52:5406–5425, 2006.

[4] M Lustig, D Donoho, and JM Pauly. Sparse mri: The application of compressed sensing for rapid mr imaging. *Magn Reson Med*, 58:1182–1195, 2007.

[5] Y Ye. *Interior Point Algorithms: Theory and Analysis*. John Wiley & Sons, Inc., 1997.

[6] SJ Kim, K. Koh, M. Lustig, S. Boyd, and D. Gorinevsky. An interior-point method for large-scale l1-regularized least squares. *IEEE Journal of Selected Topics in Signal Processing*, 1:606–617, 2007.

[7] J Friedman, T. Hastie, H Hofling, and R. Tibshirani. Pathwise coordinate optimization. *The annuals of applied statistics*, 1:302–332, 2007.

[8] ET Hale, W. Yin, and Y. Zhang. A fixed-point continuation method for l1-regularized minimization with applications to compressed sensing. Technical report, Department of Computational and Applied Mathematics, Rice University, 2007.

[9] W. Yin, S. Osher, D. Goldfarb, and J. Darbon. Bregman iterative algorithms for l1-minimization with applications to compressed sensing. *SIAM Journal on Imaging Sciences*, 1:143–168, 2008.

[10] M.A.T. Figueiredo and R.D. Nowak. A bound optimization approach to wavelet-based image deconvolution. In *Image Processing, 2005. ICIP 2005. IEEE International Conference on*, volume 2, pages II–782. IEEE, 2005.

[11] I. Daubechies, M. Defrise, and C. De Mol. An iterative thresholding algorithm for linear inverse problems with a sparsity constraint. *Communications on pure and applied mathematics*, 57(11):1413–1457, 2004.

[12] Y. Nesterov. Gradient methods for minimizing composite functions. *preprint*, 2007.

[13] M.A.T. Figueiredo, R.D. Nowak, and S.J. Wright. Gradient projection for sparse reconstruction: Application to compressed sensing and other inverse problems. *Selected Topics in Signal Processing, IEEE Journal of*, 1(4):586–597, 2007.

[14] T. Blumensath and M.E. Davies. Iterative hard thresholding for compressed sensing. *Applied and Computational Harmonic Analysis*, 27(3):265–274, 2009.

[15] K.K. Herrity, A.C. Gilbert, and J.A. Tropp. Sparse approximation via iterative thresholding. In *Acoustics, Speech and Signal Processing, 2006. ICASSP 2006 Proceedings. 2006 IEEE International Conference on*, volume 3, pages III–III. IEEE, 2006.

[16] M. Fornasier and H. Rauhut. Iterative thresholding algorithms. *Applied and Computational Harmonic Analysis*, 25(2):187–208, 2008.

[17] K. Khare, C.J. Hardy, K.F. King, P.A. Turski, and L. Marinelli. Accelerated mr imaging using compressive sensing with no free parameters. *Magn Reson Med*, 2012.

[18] D.L. Donoho and J.M. Johnstone. Ideal spatial adaptation by wavelet shrinkage. *Biometrika*, 81(3):425–455, 1994.

[19] D.L. Donoho and I.M. Johnstone. Adapting to unknown smoothness via wavelet shrinkage. *Journal of the american statistical association*, 90(432):1200–1224, 1995.

[20] D.L. Donoho, I.M. Johnstone, G. Kerkyacharian, and D. Picard. Wavelet shrinkage: asymptopia? *Journal of the Royal Statistical Society. Series B (Methodological)*, pages 301–369, 1995.

[21] D.L. Donoho and I.M. Johnstone. Minimax estimation via wavelet shrinkage. *The Annals of Statistics*, 26(3):879–921, 1998.

[22] H.A. Chipman, E.D. Kolaczyk, and R.E. McCulloch. Adaptive bayesian wavelet shrinkage. *Journal of the American Statistical Association*, 92(440):1413–1421, 1997.

[23] S.G. Chang, B. Yu, and M. Vetterli. Adaptive wavelet thresholding for image denoising and compression. *Image Processing, IEEE Transactions on*, 9(9):1532–1546, 2000.

[24] CM Stein. Estimation of the mean of a multivariate normal distribution. *The annals of Statistics*, 9:1135–1151, 1981.

5 Conclusion and outlook

5.1 Conclusion

A non-contrast-enhanced angiography technique was developed by combining pseudo continuous arterial spin labeling (PCASL) and accelerated 3D radial trajectory (VIPR). Benefited from the sparsity provides by PCASL and noise-like artifacts of VIPR, this new technique can acquire 3D intracranial angiograms with submillimeter isotropic resolution and whole head coverage with a 8-min scan. Image quality and ability of pathology delineation of PCASL-VIPR has been compared to 3D TOF which is most frequently performed in clinical intracranial MRA. The results of this preliminary study were very promising which demonstrated PCASL-VIPR of equally good image quality, much fewer saturation artifacts, and excellent pathology visualization. Compared to 3D TOF which can only perform static imaging, ASL based angiography technique can acquire hemodynamics which is important in delineating abnormal flow pattern in intracranial diseases. Dynamic PCASL-VIPR sequence was developed by acquiring multiple tag images and modulating the effective tagging duration in each acquisition. The sequence was optimized to best equalize the MT effects among acquisitions and be time efficient so the scan time remains in a clinical acceptable range. This dynamic method was able to acquire temporal resolution of 200 ms without sacrificing spatial resolution. High temporal resolution of dynamic PCASL was demonstrated in AVM patients that are most challenging due to high flow. This preliminary study showed good image

quality of the temporal images when compared to 3D TOF and excellent temporal fidelity when correlated with DSA images. Quantitative temporal information can be extracted from the time series images by the method Time-of-Arrival (TOA) mapping which has been validated in both digital simulations and in-vivo study. PCASL angiography is, in principle, highly amenable to accelerated reconstruction method like compressed sensing (CS). In our work, CS combined with parallel imaging was implemented using iterative soft thresholding framework which offers reduced memory footprint for large problems and stable. Wavelet was chosen as sparsifying transform therefore auto tuning methods that are well known in wavelet denoising problems can be utilized. This fully 3D compressed sensing with data-driven tuning demonstrated its usefulness in improving SNR in high resolution 3D intracranial ASL angiography. Other potential of PCASL has also been explored. Vessel-selective PCASL was implemented using a single-artery tagging scheme by inserting in-plane gradients. Combined with SSFP instead of SPGR for higher SNR and used in 1.5 T scanner instead of 3-T for lower off-resonance artifacts, vessel-selective PCASL-VIPR was able to tag left carotid, right carotid, and basilar arteries separately at a cost of increased scan times. Hadamard matrix was utilized for temporal encoding in tagging pulse train design of dynamic PCASL. Temporal images were acquired by combining all acquisitions instead of two. SNR was increased compared to standard sequence as demonstrated by volunteer study.

5.2 Future work

Adjusting protocols according to the patients:

There are some free parameters that are subject-dependent in dynamic PCASL-VIPR protocol. The entire length of PCASL pulse train and the time spacing between frames need to be adjusted to the patients with different flow pattern. Typically three kinds of patients need to

be considered: the ones with high flow and require high temporal resolution (e.g. pediatric patients), the ones with regular flow, and the ones with slow flow (e.g. aged patients or patients with occluded arteries).

Further validation of TOA mapping:

So far the TOA maps acquired from time series images are only for display. A study with larger size of healthy subjects is needed. TOA measurements will be evaluated across subjects so a normal range of TOA values at regions of clinical interest can be generated as basis. To further validate TOA mapping method, DSA images should be studied to acquire TOA maps which will be compared with the ones acquired using PCASL as reference.

Larger scale clinical study:

Larger scale clinical study will be planned to evaluate both static PCASL-VIPR and dynamic PCASL-VIPR. The evaluation should include image quality (compared with 3D TOF), temporal fidelity (compared with DSA), and pathology diagnosis. The validation should be performed separately on diseases: stenosis, aneurysms, and AVMs.

Vessel-selective PCASL-VIPR:

Vessel-selective PCASL-VIPR needs further development. Currently, the vessels are tagged separately in separate scans which are not time efficient and sensitive to patient motion. The sequence could be optimized by combining acquisitions in single scan. Measuring of vessel location is done manually now and needs a separate scan. An automatic method is important for clinical application.

Combining perfusion and angiography:

The labeling used in ASL perfusion and ASL angiography has no difference. The only difference of in sequence is the image acquisition. If the two techniques can be combined in one scan, not only the scan time will be reduced but also it provides convenience for later coregistration. The general idea for implementation is to utilized two different acquisitions after the PCASL spin preparation module. Right after PCASL tagging, readout for angiography will be performed immediately with a certain duration less than 1 s. This time will be also used as a post-labeling delay for the following perfusion to reduce its sensitivity to transit time heterogeneity. After the readout of angiography, a gradient crusher will be utilized to suppress the signal from the fast moving spins in the large vessels. Then, image acquisition for perfusion will be performed. Fast acquisition schemes should be chosen separately for the two readouts and so does the prescription such as NEX, image matrix, bandwidth, and etc. Background suppression is important for ASL perfusion, therefore, several inversion pulses will be inserted into the sequence in the time points that are simulated beforehand to best suppress the background tissue. One issue that needs attention is the additional signal loss in perfusion due to the reptitive RF saturation during the readout of angiography. The pacticability of this combination needs deeper consideration and further study in the future.